DESY-96-076

Measurement of the F_2 structure function in deep inelastic e^+p scattering using 1994 data from the ZEUS detector at HERA

ZEUS Collaboration

hep-ex/9607002 2 Jul 1996

Abstract

We present measurements of the structure function F_2 in e^+p scattering at HERA in the range $3.5\ \mathrm{GeV}^2 < Q^2 < 5000\ \mathrm{GeV}^2$. A new reconstruction method has allowed a significant improvement in the resolution of the kinematic variables and an extension of the kinematic region covered by the experiment. At $Q^2 < 35\ \mathrm{GeV}^2$ the range in x now spans $6.3 \cdot 10^{-5} < x < 0.08$ providing overlap with measurements from fixed target experiments. At values of Q^2 above $1000\ \mathrm{GeV}^2$ the x range extends to 0.5. Systematic errors below 5% have been achieved for most of the kinematic region. The structure function rises as x decreases; the rise becomes more pronounced as Q^2 increases. The behaviour of the structure function data is well described by next-to-leading order perturbative QCD as implemented in the DGLAP evolution equations.

The ZEUS Collaboration

M. Derrick, D. Krakauer, S. Magill, D. Mikunas, B. Musgrave, J.R. Okrasinski, J. Repond, R. Stanek, R.L. Talaga, H. Zhang
Argonne National Laboratory, Argonne, IL, USA [p]

M.C.K. Mattingly
Andrews University, Berrien Springs, MI, USA

F. Anselmo, P. Antonioli, G. Bari, M. Basile, L. Bellagamba, D. Boscherini, A. Bruni, G. Bruni, P. Bruni,
G. Cara Romeo, G. Castellini[1], L. Cifarelli[2], F. Cindolo, A. Contin, M. Corradi, I. Gialas, P. Giusti, G. Iacobucci, G. Laurenti, G. Levi, A. Margotti, T. Massam, R. Nania, F. Palmonari, A. Pesci, A. Polini, G. Sartorelli, Y. Zamora Garcia[3], A. Zichichi
University and INFN Bologna, Bologna, Italy [f]

C. Amelung, A. Bornheim, J. Crittenden, R. Deffner, T. Doeker[4], M. Eckert, L. Feld, A. Frey[5], M. Geerts, M. Grothe, H. Hartmann, K. Heinloth, L. Heinz, E. Hilger, H.-P. Jakob, U.F. Katz, S. Mengel[6], E. Paul, M. Pfeiffer, Ch. Rembser, D. Schramm[7], J. Stamm, R. Wedemeyer
Physikalisches Institut der Universität Bonn, Bonn, Germany [c]

S. Campbell-Robson, A. Cassidy, W.N. Cottingham, N. Dyce, B. Foster, S. George, M.E. Hayes, G.P. Heath, H.F. Heath, D. Piccioni, D.G. Roff, R.J. Tapper, R. Yoshida
H.H. Wills Physics Laboratory, University of Bristol, Bristol, U.K. [o]

M. Arneodo[8], R. Ayad, M. Capua, A. Garfagnini, L. Iannotti, M. Schioppa, G. Susinno
Calabria University, Physics Dept.and INFN, Cosenza, Italy [f]

A. Caldwell[9], N. Cartiglia, Z. Jing, W. Liu, J.A. Parsons, S. Ritz[10], F. Sciulli, P.B. Straub, L. Wai[11], S. Yang[12], Q. Zhu
Columbia University, Nevis Labs., Irvington on Hudson, N.Y., USA [q]

P. Borzemski, J. Chwastowski, A. Eskreys, Z. Jakubowski, M.B. Przybycień, M. Zachara, L. Zawiejski
Inst. of Nuclear Physics, Cracow, Poland [j]

L. Adamczyk, B. Bednarek, K. Jeleń, D. Kisielewska, T. Kowalski, M. Przybycień, E. Rulikowska-Zarębska, L. Suszycki, J. Zając
Faculty of Physics and Nuclear Techniques, Academy of Mining and Metallurgy, Cracow, Poland [j]

Z. Duliński, A. Kotański
Jagellonian Univ., Dept. of Physics, Cracow, Poland [k]

G. Abbiendi[13], L.A.T. Bauerdick, U. Behrens, H. Beier, J.K. Bienlein, G. Cases, O. Deppe, K. Desler, G. Drews, M. Flasiński[14], D.J. Gilkinson, C. Glasman, P. Göttlicher, J. Große-Knetter, T. Haas, W. Hain, D. Hasell, H. Heßling, Y. Iga, K.F. Johnson[15], P. Joos, M. Kasemann, R. Klanner, W. Koch, U. Kötz, H. Kowalski, J. Labs, A. Ladage, B. Löhr, M. Löwe, D. Lüke, J. Mainusch[16], O. Mańczak, J. Milewski, T. Monteiro[17], J.S.T. Ng, D. Notz, K. Ohrenberg, K. Piotrzkowski, M. Roco, M. Rohde, J. Roldán, U. Schneekloth, W. Schulz, F. Selonke, B. Surrow, E. Tassi, T. Voß, D. Westphal, G. Wolf, U. Wollmer, C. Youngman, W. Zeuner
Deutsches Elektronen-Synchrotron DESY, Hamburg, Germany

H.J. Grabosch, A. Kharchilava[18], S.M. Mari[19], A. Meyer, S. Schlenstedt, N. Wulff
DESY-IfH Zeuthen, Zeuthen, Germany

G. Barbagli, E. Gallo, P. Pelfer
University and INFN, Florence, Italy [f]

G. Maccarrone, S. De Pasquale, L. Votano
INFN, Laboratori Nazionali di Frascati, Frascati, Italy [f]

A. Bamberger, S. Eisenhardt, T. Trefzger[20], S. Wölfle
Fakultät für Physik der Universität Freiburg i.Br., Freiburg i.Br., Germany [c]

J.T. Bromley, N.H. Brook, P.J. Bussey, A.T. Doyle, D.H. Saxon, L.E. Sinclair, M.L. Utley, A.S. Wilson
Dept. of Physics and Astronomy, University of Glasgow, Glasgow, U.K. [o]

A. Dannemann[21], U. Holm, D. Horstmann, R. Sinkus, K. Wick
Hamburg University, I. Institute of Exp. Physics, Hamburg, Germany [c]

B.D. Burow[22], L. Hagge[16], E. Lohrmann, G. Poelz, W. Schott, F. Zetsche
Hamburg University, II. Institute of Exp. Physics, Hamburg, Germany [c]

T.C. Bacon, N. Brümmer, I. Butterworth, V.L. Harris, G. Howell, B.H.Y. Hung, L. Lamberti[23], K.R. Long, D.B. Miller, N. Pavel, A. Prinias[24], J.K. Sedgbeer, D. Sideris, A.F. Whitfield
Imperial College London, High Energy Nuclear Physics Group, London, U.K. [o]

U. Mallik, M.Z. Wang, S.M. Wang, J.T. Wu
University of Iowa, Physics and Astronomy Dept., Iowa City, USA [p]

P. Cloth, D. Filges
Forschungszentrum Jülich, Institut für Kernphysik, Jülich, Germany

S.H. An, G.H. Cho, B.J. Ko, S.B. Lee, S.W. Nam, H.S. Park, S.K. Park
Korea University, Seoul, Korea [h]

S. Kartik, H.-J. Kim, R.R. McNeil, W. Metcalf, V.K. Nadendla
Louisiana State University, Dept. of Physics and Astronomy, Baton Rouge, LA, USA [p]

F. Barreiro, J.P. Fernandez, R. Graciani, J.M. Hernández, L. Hervás, L. Labarga, M. Martinez, J. del Peso, J. Puga, J. Terron, J.F. de Trocóniz
Univer. Autónoma Madrid, Depto de Física Teórica, Madrid, Spain [n]

F. Corriveau, D.S. Hanna, J. Hartmann, L.W. Hung, J.N. Lim, C.G. Matthews[25], P.M. Patel, M. Riveline, D.G. Stairs, M. St-Laurent, R. Ullmann, G. Zacek[25]
McGill University, Dept. of Physics, Montréal, Québec, Canada [a], [b]

T. Tsurugai
Meiji Gakuin University, Faculty of General Education, Yokohama, Japan

V. Bashkirov, B.A. Dolgoshein, A. Stifutkin
Moscow Engineering Physics Institute, Mosocw, Russia [l]

G.L. Bashindzhagyan[26], P.F. Ermolov, L.K. Gladilin, Yu.A. Golubkov, V.D. Kobrin, I.A. Korzhavina, V.A. Kuzmin, O.Yu. Lukina, A.S. Proskuryakov, A.A. Savin, L.M. Shcheglova, A.N. Solomin, N.P. Zotov
Moscow State University, Institute of Nuclear Physics, Moscow, Russia [m]

M. Botje, F. Chlebana, J. Engelen, M. de Kamps, P. Kooijman, A. Kruse, A. van Sighem, H. Tiecke, W. Verkerke, J. Vossebeld, M. Vreeswijk, L. Wiggers, E. de Wolf, R. van Woudenberg[27]
NIKHEF and University of Amsterdam, Netherlands [i]

D. Acosta, B. Bylsma, L.S. Durkin, J. Gilmore, C. Li, T.Y. Ling, P. Nylander, I.H. Park, T.A. Romanowski[28]
Ohio State University, Physics Department, Columbus, Ohio, USA [p]

D.S. Bailey, R.J. Cashmore[29], A.M. Cooper-Sarkar, R.C.E. Devenish, N. Harnew, M. Lancaster[30], L. Lindemann, J.D. McFall, C. Nath, V.A. Noyes[24], A. Quadt, J.R. Tickner, H. Uijterwaal, R. Walczak, D.S. Waters, F.F. Wilson, T. Yip
Department of Physics, University of Oxford, Oxford, U.K. [o]

A. Bertolin, R. Brugnera, R. Carlin, F. Dal Corso, M. De Giorgi, U. Dosselli, S. Limentani, M. Morandin, M. Posocco, L. Stanco, R. Stroili, C. Voci, F. Zuin
Dipartimento di Fisica dell' Universita and INFN, Padova, Italy [f]

J. Bulmahn, R.G. Feild[31], B.Y. Oh, J.J. Whitmore
Pennsylvania State University, Dept. of Physics, University Park, PA, USA [q]

G. D'Agostini, G. Marini, A. Nigro
Dipartimento di Fisica, Univ. 'La Sapienza' and INFN, Rome, Italy [f]

J.C. Hart, N.A. McCubbin, T.P. Shah
Rutherford Appleton Laboratory, Chilton, Didcot, Oxon, U.K. [o]

E. Barberis, T. Dubbs, C. Heusch, M. Van Hook, W. Lockman, J.T. Rahn, H.F.-W. Sadrozinski, A. Seiden, D.C. Williams
University of California, Santa Cruz, CA, USA [p]

J. Biltzinger, R.J. Seifert, O. Schwarzer, A.H. Walenta, G. Zech
Fachbereich Physik der Universität-Gesamthochschule Siegen, Germany [c]

H. Abramowicz, G. Briskin, S. Dagan[32], A. Levy[26]
Raymond and Beverly Sackler Faculty of Exact Sciences, School of Physics, Tel-Aviv University, Tel-Aviv, Israel [e]

J.I. Fleck[33], M. Inuzuka, T. Ishii, M. Kuze, S. Mine, M. Nakao, I. Suzuki, K. Tokushuku, K. Umemori, S. Yamada, Y. Yamazaki
Institute for Nuclear Study, University of Tokyo, Tokyo, Japan [g]

M. Chiba, R. Hamatsu, T. Hirose, K. Homma, S. Kitamura[34], T. Matsushita, K. Yamauchi
Tokyo Metropolitan University, Dept. of Physics, Tokyo, Japan [g]

R. Cirio, M. Costa, M.I. Ferrero, S. Maselli, C. Peroni, R. Sacchi, A. Solano, A. Staiano
Universita di Torino, Dipartimento di Fisica Sperimentale and INFN, Torino, Italy [f]

M. Dardo
II Faculty of Sciences, Torino University and INFN - Alessandria, Italy [f]

D.C. Bailey, F. Benard, M. Brkic, C.-P. Fagerstroem, G.F. Hartner, K.K. Joo, G.M. Levman, J.F. Martin, R.S. Orr, S. Polenz, C.R. Sampson, D. Simmons, R.J. Teuscher
University of Toronto, Dept. of Physics, Toronto, Ont., Canada [a]

J.M. Butterworth, C.D. Catterall, T.W. Jones, P.B. Kaziewicz, J.B. Lane, R.L. Saunders, J. Shulman, M.R. Sutton
University College London, Physics and Astronomy Dept., London, U.K. [o]

B. Lu, L.W. Mo
Virginia Polytechnic Inst. and State University, Physics Dept., Blacksburg, VA, USA [q]

W. Bogusz, J. Ciborowski, J. Gajewski, G. Grzelak[35], M. Kasprzak, M. Krzyżanowski, K. Muchorowski[36], R.J. Nowak, J.M. Pawlak, T. Tymieniecka, A.K. Wróblewski, J.A. Zakrzewski, A.F. Żarnecki
Warsaw University, Institute of Experimental Physics, Warsaw, Poland [j]

M. Adamus
Institute for Nuclear Studies, Warsaw, Poland [j]

C. Coldewey, Y. Eisenberg[32], D. Hochman, U. Karshon[32], D. Revel[32], D. Zer-Zion
Weizmann Institute, Nuclear Physics Dept., Rehovot, Israel [d]

W.F. Badgett, J. Breitweg, D. Chapin, R. Cross, S. Dasu, C. Foudas, R.J. Loveless, S. Mattingly, D.D. Reeder, S. Silverstein, W.H. Smith, A. Vaiciulis, M. Wodarczyk
University of Wisconsin, Dept. of Physics, Madison, WI, USA [p]

S. Bhadra, M.L. Cardy, W.R. Frisken, M. Khakzad, W.N. Murray, W.B. Schmidke
York University, Dept. of Physics, North York, Ont., Canada [a]

[1] also at IROE Florence, Italy
[2] now at Univ. of Salerno and INFN Napoli, Italy
[3] supported by Worldlab, Lausanne, Switzerland
[4] now as MINERVA-Fellow at Tel-Aviv University
[5] now at Univ. of California, Santa Cruz
[6] now at VDI-Technologiezentrum Düsseldorf
[7] now at Commasoft, Bonn
[8] also at University of Torino and Alexander von Humboldt Fellow
[9] Alexander von Humboldt Fellow
[10] Alfred P. Sloan Foundation Fellow
[11] now at University of Washington, Seattle
[12] now at California Institute of Technology, Los Angeles
[13] supported by an EC fellowship number ERBFMBICT 950172
[14] now at Inst. of Computer Science, Jagellonian Univ., Cracow
[15] visitor from Florida State University
[16] now at DESY Computer Center
[17] supported by European Community Program PRAXIS XXI
[18] now at Univ. de Strasbourg
[19] present address: Dipartimento di Fisica, Univ. "La Sapienza", Rome
[20] now at ATLAS Collaboration, Univ. of Munich
[21] now at Star Division Entwicklungs- und Vertriebs-GmbH, Hamburg
[22] also supported by NSERC, Canada
[23] supported by an EC fellowship
[24] PPARC Post-doctoral Fellow
[25] now at Park Medical Systems Inc., Lachine, Canada
[26] partially supported by DESY
[27] now at Philips Natlab, Eindhoven, NL
[28] now at Department of Energy, Washington
[29] also at University of Hamburg, Alexander von Humboldt Research Award
[30] now at Lawrence Berkeley Laboratory, Berkeley
[31] now at Yale University, New Haven, CT
[32] supported by a MINERVA Fellowship
[33] supported by the Japan Society for the Promotion of Science (JSPS)
[34] present address: Tokyo Metropolitan College of Allied Medical Sciences, Tokyo 116, Japan
[35] supported by the Polish State Committee for Scientific Research, grant No. 2P03B09308
[36] supported by the Polish State Committee for Scientific Research, grant No. 2P03B09208

[a] supported by the Natural Sciences and Engineering Research Council of Canada (NSERC)
[b] supported by the FCAR of Québec, Canada
[c] supported by the German Federal Ministry for Education and Science, Research and Technology (BMBF), under contract numbers 057BN19P, 057FR19P, 057HH19P, 057HH29P, 057SI75I
[d] supported by the MINERVA Gesellschaft für Forschung GmbH, the Israel Academy of Science and the U.S.-Israel Binational Science Foundation
[e] supported by the German Israeli Foundation, and by the Israel Academy of Science
[f] supported by the Italian National Institute for Nuclear Physics (INFN)
[g] supported by the Japanese Ministry of Education, Science and Culture (the Monbusho) and its grants for Scientific Research
[h] supported by the Korean Ministry of Education and Korea Science and Engineering Foundation
[i] supported by the Netherlands Foundation for Research on Matter (FOM)
[j] supported by the Polish State Committee for Scientific Research, grants No. 115/E-343/SPUB/P03/109/95, 2P03B 244 08p02, p03, p04 and p05, and the Foundation for Polish-German Collaboration (proj. No. 506/92)
[k] supported by the Polish State Committee for Scientific Research (grant No. 2 P03B 083 08) and Foundation for Polish-German Collaboration
[l] partially supported by the German Federal Ministry for Education and Science, Research and Technology (BMBF)
[m] supported by the German Federal Ministry for Education and Science, Research and Technology (BMBF), and the Fund of Fundamental Research of Russian Ministry of Science and Education and by INTAS-Grant No. 93-63
[n] supported by the Spanish Ministry of Education and Science through funds provided by CICYT
[o] supported by the Particle Physics and Astronomy Research Council
[p] supported by the US Department of Energy
[q] supported by the US National Science Foundation

1 Introduction

Measurements of neutral current (NC) deep inelastic scattering (DIS) at HERA [1, 2] have revealed a rapid rise of the proton structure function F_2 as Bjorken-x decreases below 10^{-2}. Extensions of these measurements to low Q^2 have shown that this rise persists down to Q^2 values as low as 1.5 GeV^2 [3, 4].

In this report we present a new measurement of F_2 from a DIS event sample eight times larger than that used in our previous analysis [1]. The increase in statistics combined with a new method that provides a substantially more precise reconstruction of the event kinematics has allowed us to extend the range of the measurements in x by an order of magnitude and to decrease the systematic uncertainties of F_2 by roughly a factor of three.

New data on F_2 with similar statistics in a similar kinematic range have recently been presented by H1 [4].

2 Experimental conditions

The data presented here were taken with the ZEUS detector at HERA in 1994. HERA operated with 153 colliding bunches of 820 GeV protons and 27.5 GeV positrons, with a time between bunches of 96 ns. Additional unpaired positron (15) and proton (17) bunches circulated, which are used to determine beam related backgrounds. The proton bunch length was approximately 20 cm (r.m.s.) while the positron bunch length was negligible in comparison which, together with run-to-run variations of the mean interaction position, leads to a length of the interaction region of 12 cm (r.m.s.) centered around Z=+6 cm. [1] The data of this analysis correspond to a luminosity of 2.50$\pm$0.04 pb^{-1}. Approximately 5% of the proton current was contained in satellite bunches, which were shifted by 4.8 ns with respect to the primary bunch crossing time, resulting in a fraction of the ep interactions occurring at $\langle Z \rangle = +78$ cm.

A description of the ZEUS detector can be found in [5, 6]. The components used in this analysis are briefly discussed. The uranium-scintillator calorimeter (CAL) [7] covers 99.7% of the total solid angle. It consists of the barrel calorimeter (BCAL) covering the range $36.7^\circ < \theta < 129.1^\circ$ in polar angle, the forward calorimeter (FCAL) covering $2.6^\circ < \theta < 36.7^\circ$ and the rear calorimeter (RCAL) covering $129.1^\circ < \theta < 176.2^\circ$. The FCAL and RCAL are divided in two halves to allow retraction during beam injection. Each calorimeter part is segmented in electromagnetic (EMC) and hadronic (HAC) sections. Each section is further subdivided into cells of typically 5×20 cm^2 (10×20 cm^2 in the RCAL) for the EMC and 20×20 cm^2 for the HAC sections. Each cell is viewed by two photomultipliers (PMTs). Under test beam conditions the calorimeter has an energy resolution of $\sigma/E = 18\%/\sqrt{E(\mathrm{GeV})}$ for electrons and $\sigma/E = 35\%/\sqrt{E(\mathrm{GeV})}$ for hadrons. The timing resolution of a calorimeter cell is less than 1 ns for energy deposits greater than 4.5 GeV. In order to minimise the effects of noise due to the uranium radioactivity on the measurements all EMC(HAC) cells with an energy deposit of less than 60(110) MeV are discarded from the analysis. For cells with isolated energy deposits this cut was increased to 100(150) MeV.

[1] The ZEUS coordinate system is defined as right handed with the Z axis pointing in the proton beam direction, and the X axis horizontal, pointing towards the centre of HERA.

The tracking system consists of a vertex detector (VXD) [8], a central tracking chamber (CTD) [9], and a rear tracking detector (RTD) [6] enclosed in a 1.43 T solenoidal magnetic field. The interaction vertex is measured with a typical resolution along (transverse to) the beam direction of 0.4 (0.1) cm. For high momentum tracks ($p > 5$ GeV) the extrapolated position on the inner face of the calorimeters is known with a typical resolution of 0.3 cm.

The position of positrons scattered at small angles to the positron beam direction is measured using the small angle rear tracking detector (SRTD) which is attached to the front face of the RCAL. The SRTD consists of two planes of scintillator strips, 1 cm wide and 0.5 cm thick, arranged in orthogonal directions and read out via optical fibers and photo-multiplier tubes. It covers the region of 68×68 cm^2 in X and Y and is positioned at $Z = -148$ cm. A hole of 20×20 cm^2 at the center of the RCAL and SRTD accommodates the beampipe. The SRTD signals resolve single minimum ionizing particles and provide a position resolution of 0.3 cm. The time resolution is less than 2 ns for a minimum ionizing particle.

The luminosity is measured via the positron-proton bremsstrahlung process, $ep \to e\gamma p$, using a lead-scintillator calorimeter (LUMI) [10] which accepts photons at angles ≤ 0.5 mrad with respect to the positron beam direction. The LUMI photon calorimeter is also used to tag photons from initial state radiation in DIS events. It is positioned at $Z = -107$ m and has an energy resolution of $\sigma/E = 18\%/\sqrt{E(\mathrm{GeV})}$ under test beam conditions. In its operating position, however, it is shielded from synchrotron radiation by a carbon-lead filter and has an energy resolution of $\sigma/E = 26.5\%/\sqrt{E(\mathrm{GeV})}$, as determined from bremsstrahlung data. The position resolution is 0.2 cm in X and Y. In addition, an electromagnetic calorimeter positioned at $Z = -35$ m is used for tagging positrons scattered at small angles.

2.1 Triggering

Events were filtered online by a three level trigger system [6]. At the first level, the events are selected by the logical OR of the following conditions (further details can be found in [11]):

- Total EMC energy deposit in the BCAL is greater than 4.8 GeV.
- Total EMC energy deposit in the RCAL, excluding the region closest to the rear beampipe, is greater than 3.4 GeV.
- In the RCAL, the isolated positron condition (ISO-e) is fulfilled. The ISO-e condition requires that the isolated EMC energy deposit be greater than 2.5 GeV and that the corresponding HAC energy be less than 0.95 GeV or no more than a third of the EMC energy. The above condition is ANDed with the requirement that the total energy deposit in RCAL EMC is greater than 3.8 GeV.

Events where the positron is scattered in the direction of the FCAL are triggered efficiently, by the hadronic final state, with the above requirements.

Backgrounds from protons interacting outside the detector were rejected using the time measurement of the energy deposits in upstream veto counters and the SRTD. The average trigger efficiency for events that pass the off-line selection cuts (see Sect. 6) is above 99%, as determined from independent triggers and MC simulation.

In the second level trigger (SLT), background was further reduced using the measured times of energy deposits and the summed energies from the calorimeter. The events were accepted if:

$$\delta_{SLT} \equiv \sum_i E_i(1-\cos\theta_i) > (24 - 2E_\gamma) \quad \text{(GeV)} \tag{1}$$

where E_i and θ_i are the energies and polar angles (with respect to $X = Y = Z = 0$ cm) of calorimeter cells, and E_γ is the energy deposit measured in the LUMI photon calorimeter. For perfect detector resolution, δ_{SLT} is twice the positron beam energy (55 GeV) for fully contained DIS events while for photoproduction events, where the scattered positron escapes down the beampipe, δ_{SLT} peaks at much lower values. Proton beam-gas events which originate from inside the detector have energy flows which are concentrated in the forward direction and so also have small values of δ_{SLT}.

The full event information was available at the third level trigger (TLT). Tighter timing cuts as well as algorithms to remove beam-halo muons and cosmic muons were applied. The quantity δ_{TLT} was determined in the same way as δ_{SLT}. The events were required to have $\delta_{TLT} > (25 - 2E_\gamma)$ (GeV). Finally, events were accepted if a scattered positron candidate of energy greater than 4 GeV was found. In total 900853 NC DIS candidates satisfied the above trigger conditions.

3 Monte Carlo simulation

Monte Carlo (MC) event simulation is used to correct for detector acceptance and smearing effects. The detector simulation is based on the GEANT program [12] and incorporates our understanding of the detector, the trigger and test beam results. Neutral current DIS events are simulated using the HERACLES program [13] which includes photon and Z^0 exchanges and first order electroweak radiative corrections. The hadronic final state is simulated using the colour-dipole model CDMBGF [14] including all leading order QCD diagrams as implemented in ARIADNE [15] for the QCD cascade and JETSET [16] for the hadronisation. The ARIADNE model provides the best description of the observed DIS non-diffractive hadronic final state [17]. Diffractive events which have been observed in the data [18, 19] by the occurrence of a large rapidity gap in the detector are simulated within ARIADNE by assuming that the struck quark belongs to a colourless state having only a small fraction of the proton's momentum. The parameters of the model are adjusted to be consistent with recent ZEUS measurements [20]. The MRSA [21] parton density parameterisations, modified at low Q^2 as described in [22], are used. For the final acceptance corrections, the events are reweighted with the help of a NLO QCD fit to the data in an iterative procedure as described in Sect. 7. For systematic checks, a sample of events was also generated using the LEPTO Matrix Element and Parton Shower (MEPS) [23] final state simulation.

The shape of the vertex distribution used in the simulation is taken from non-diffractive photoproduction events, since for these events the vertex reconstruction efficiency is found to be both high ($\sim 90\%$) and independent of the Z position of the interaction.

The effects of the uranium radioactivity were simulated using distributions obtained from randomly triggered events.

A MC event sample corresponding to an integrated luminosity of 2.5 pb^{-1} for $Q^2 > 1.8$ GeV^2 was generated. This sample was supplemented by an additional sample equivalent to 2.5 pb^{-1} with $Q^2 > 20$ GeV^2.

The main source of background in the data comes from the few photoproduction interactions which lead to the detection of a fake scattered positron. 'Minimum bias' photoproduction events were simulated using PYTHIA [24] with cross sections according to the ALLM parameterisation [25]. Photoproduction events corresponding to an integrated luminosity of 250 nb^{-1} were generated with a photon-proton center-of-mass energy $W \gtrsim 190$ GeV. Events with smaller W values do not contribute to the photoproduction background due to the requirement on δ (see Sect. 6).

4 Energy and angle measurements

In the determination of the DIS kinematics, the CAL energy deposits are separated into those associated with the identified scattered positron, and all other energy deposits. The latter is defined as energy from the hadronic system, or hadronic energy. The kinematics of the event is then determined from:

- The energy (E'_e) and polar angle (θ_e) of the scattered positron.
- The hadronic energy in terms of

$$\delta_h \equiv \sum_h (E_h - p_{Zh}) \tag{2}$$

and

$$p_{Th} \equiv \sqrt{(\sum_h p_{Xh})^2 + (\sum_h p_{Yh})^2} \tag{3}$$

where the sums run over all CAL energy deposits not associated with the scattered positron.

The hadronic energy flow is characterised by the angle γ_H defined by:

$$\cos\gamma_H = \frac{p_{Th}^2 - \delta_h^2}{p_{Th}^2 + \delta_h^2}. \tag{4}$$

In the naive quark parton model picture of DIS the angle γ_H corresponds to the polar angle of the struck quark.

4.1 Positron identification and efficiency

The positron identification algorithm (SINISTRA94) is based on a neural network using information from the CAL [26]. The network separates deposits in the calorimeter which are due to electromagnetically showering particles from those which are of hadronic origin, by assigning a 'positron-probability'. A cut on this probability allows a clean identification of the scattered

positron.[2] The efficiency for finding the scattered positron was determined from MC simulations to increase from 80% at 10 GeV to greater than 99% for energies above 15 GeV. The efficiency was checked by using QED-Compton events and by comparing results from this algorithm with other positron finding algorithms [1] and found to be consistent with expectations.

4.2 Positron angle measurement

The scattering angle of the positron is determined either by measurement of its impact position on the CAL inner face together with the event vertex, or, for $\theta_e < 135°$, from the parameters of a reconstructed track matched with the positron impact position.

The impact position of the scattered positron at the calorimeter is reconstructed using the CAL or the SRTD. When both CAL and SRTD information are available, the SRTD reconstruction is used.

- CAL – The position of a shower in the CAL can be determined using the pulse-height sharing between left and right PMTs and between neighbouring cells. The position resolution on the face of the CAL is about 1 cm. The position measurement was checked by matching tracks and positron candidates. The resolution of the track-CAL matching is found to be 1.1 cm and systematic biases are less than 2 mm (see Fig. 1a and b).

- SRTD – The position in the SRTD is determined from the centres of gravity of the pulse-heights of the strips in the X and Y planes of the SRTD. The measured SRTD position resolution is 0.3 cm. For a subset of these positrons the position measured by the SRTD can be compared to the result from the track measurement. The resolution of the track-SRTD matching is measured to be 0.5 cm and systematic deviations are less than 0.1 cm (see Fig. 1c and d).

The coordinates of the event vertex are determined from tracks reconstructed with the CTD and VXD. The Z coordinate (Z_{vertex}) is determined on an event-by-event basis. Since the transverse sizes of the beams are smaller than the resolutions for the X and Y coordinates of the vertex, the beam X and Y positions averaged over a single beam-fill are used. For events which do not have a tracking vertex, the Z coordinate is set to the nominal position of the interaction point ($Z = +6$ cm).

The probability of finding a vertex depends on the number of particles which traverse the tracking detectors and thus mainly on the hadronic angle γ_H. Figure 1e, which shows the fraction of events having a reconstructed vertex as a function of γ_H, exhibits the expected behaviour. For $\gamma_H > 70°$ the vertex finding efficiency is greater than 95%. It decreases to around 50% for events with $\gamma_H \sim 20°$. The MC simulation reproduces the observed behaviour reasonably well. Relative differences of the order of 5-10% are observed in the region below $\gamma_H = 30°$. The drop in vertex finding efficiency in the region around $\gamma_H = 174°$ results from the combination of the characteristics of the DIS final states and the acceptance of the CTD in the rear direction. The effect is not fully reproduced by the MC simulation. All differences

[2] Contrary to the previous analysis [3], in this analysis we allow the cut on the probability to vary with the calorimeter energy associated with the positron.

between data and MC simulation are taken into account in the determination of the systematic uncertainties on the final results.

Figure 1f shows the Z resolution of the vertex reconstruction as a function of γ_H. For $\gamma_H > 40°$ the resolution is $\sigma_Z^{track} = 0.2$ cm, while for events with γ_H close to zero [3] it becomes $\sigma_Z^{track} = 2.5 \pm 0.4$ cm. For events where no vertex is reconstructed, the effective resolution is determined by the length of the interaction region, which is $\sigma_Z^{beam} = 12$ cm. It is also possible to determine the Z coordinate of the vertex from the measurements of the arrival times of energy deposits in the FCAL [1]. In this measurement the resolution is $\sigma_Z^{timing} = 17$ cm, and it is only used for studies of systematic errors.

For polar angles $45° < \theta_e < 135°$ and positron transverse momenta $p_{Te} > 5$ GeV the tracking efficiency is greater than 98%. Thus when the positron angle, as determined by the CAL, is smaller than 135° a track is required to match the positron identified in the CAL and the polar angle is taken from the track parameters. A successful match is obtained when the distance between the extrapolated impact point of the track on the face of the CAL and the position determined by the CAL is less than 5 cm. In this region the matching efficiency is above 97% and the combined efficiency for tracking and matching is greater than 95%.

The resolution of the scattering angle measurement is $\sigma_{\theta_e}^{SRTD} = 2.0$ mrad for positrons reconstructed in the SRTD, $\sigma_{\theta_e}^{CAL} \approx 6.8$ mrad for positrons determined by the CAL and $\sigma_{\theta_e}^{track} \approx 3.4$ mrad for positrons with a matched track. For events without a tracking vertex there is an additional error of $\sigma_{\theta_e}^{vertex} \approx 80\ (\sin\theta_e)$ mrad.

4.3 Positron energy determination

The scattered positron loses energy in the passive material in front of the CAL. In the region relevant for this analysis this passive material constitutes about 1.5 radiation lengths except in areas around the rear beampipe, $\theta \gtrsim 170°$, and the solenoid support structure, $130° \lesssim \theta \lesssim 145°$, where it is up to 2.5 radiation lengths. In the analysis, the measurement of the scattered positron energy by the CAL is corrected for the energy loss in the passive material.

The correction for the CAL measurement of the scattered positrons can be determined directly from the data using the following subsamples.

- At low y, the scattered positron energy is kinematically constrained to be close to the positron beam energy and to be primarily a function of the scattering angle. For these events, called Kinematic Peak (KP) events, the mean positron energy is determined from the scattering angle ($E'_e \approx \frac{2E_e}{(1-\cos\theta_e)}$) to within 0.5%. The KP events are selected by requiring $y_{JB} = \frac{\delta_h}{2E_e} < 0.04$, and provide a calibration at $E'_e \approx E_e = 27.5$ GeV for $\theta \gtrsim 135°$.

- For QED Compton events ($ep \to e\gamma p$) observed in the main detector, energies of the positron and the photon can be predicted precisely from the measurement of their scattering angles since the transverse momentum of the scattered proton is small. QED Compton events provide a calibration at $5 \lesssim E'_e \lesssim 20$ GeV and $\theta \gtrsim 160°$.

[3] The lines of constant γ_H in the (x, Q^2)-plane are given in Fig. 7b for $\gamma_H = 40°, 90°$ and 135°.

- In events from DIS ρ^o production, $ep \to ep\rho^o$ ($\rho^o \to \pi^+\pi^-$), the angle of the positron and the momenta of the π^+ and π^-, as measured with the CTD, give a precise determination of the positron energy. DIS ρ^o events provide a calibration at $20 \lesssim E'_e \lesssim 25$ GeV and $\theta \gtrsim 160°$.

- In the range $30° \lesssim \theta \lesssim 150°$, momenta of the positrons can be determined by the CTD. Although the CAL energy resolution at $E'_e > 10$ GeV is superior to the momentum resolution of the CTD, the track momenta averaged over several events give an independent check on the energy measurement of the CAL.

In the fiducial volume of the SRTD, $\theta \gtrsim 167°$, the correlation between the energy lost in the passive material in front of the calorimeter and the energy deposited in the SRTD is used to correct the calorimeter energy measurement (SRTD method). The corrections are determined using the QED Compton and the KP samples. The DIS ρ^o events are used as checks on the correction. This procedure is described in detail elsewhere [3].

In the RCAL outside the SRTD fiducial volume, $130° \lesssim \theta \lesssim 167°$, the observed energy shift of KP positrons from the value expected from kinematics, combined with test beam results of the energy loss of electrons in passive material, are used to determine the correction (KP method). This procedure is described in detail elsewhere [1]. Using the data from regions where both the KP method and the SRTD method can be applied, the uncertainty in the KP method of correction is found to be the same as that of the SRTD method.

The uncertainty in the energy determination in the RCAL after these corrections is 2% at 10 GeV linearly decreasing to 1% at 27.5 GeV.

In the region covered by BCAL and FCAL, $\theta \lesssim 130°$, comparison with the measured mean CTD momentum is used to correct the CAL energy measurement (track method). The energies corrected by the track method have an uncertainty of 2% independent of the energy of the positron. Where the KP method and the track method corrections can both be applied, consistent results are found.

The resolution of the positron energy measurement can be determined from the data using QED Compton, DIS ρ^o, and KP events, and is found to be in the range $\sigma/E = (20-27)\%/\sqrt{E\ (\mathrm{GeV})}$, depending on the trajectory of the positron through the passive material in front of the CAL.

Studies identical to those described above for the data were also performed with MC event samples. The resulting corrections were applied to the DIS MC sample. Thus, any difference in the CAL response between MC simulation and data is absorbed in the corrections. The resolution of the positron energy measurements in the MC simulation is adjusted to reproduce the results found from the data.

The separate positron energy corrections for MC simulation and data allow the determination of relative calibrations for the CAL in MC simulation and data. Before determining the hadronic energy, adjustments, based on the difference in the magnitude, position dependence and energy dependence of MC and data corrections, are made to bring the energy scale for data and MC simulation into agreement.

4.4 Hadronic energy determination

The hadronic energies, unlike the case of the positron energy, are not corrected for energy loss in the passive material. Instead, the transverse momentum of the positron, p_{Te}, calculated using the positron energy corrected as described in the last section, is compared to the p_{Th} of the hadrons in both the detector simulation and data. From this comparison, uncertainties in the determination of the hadronic energy are estimated. The mean $\frac{p_{Th}}{p_{Te}}$ as a function of γ_H agrees within 3% between MC simulation and data for the entire range of kinematics covered in this paper. The $\frac{p_{Th}}{p_{Te}}$ distributions in bins of γ_H are compared (see Sect. 6) for MC simulation and data, and are in good agreement. An uncertainty of $\pm 3\%$ is assigned to the hadronic energy measurement, based on these comparisons.

5 Kinematic reconstruction

In deep inelastic scattering, $e(k) + p(P) \rightarrow e(k') + X$, the proton structure functions are expressed in terms of the negative of the four-momentum transfer squared, Q^2, and Bjorken x. In the absence of QED radiation,

$$Q^2 = -q^2 = -(k - k')^2, \tag{5}$$

$$x = \frac{Q^2}{2P \cdot q}, \tag{6}$$

where k and P are the four-momenta of the incoming particles and k' is the four-momentum of the scattered lepton. The fractional energy transferred to the proton in its rest frame is $y = Q^2/(sx)$ where s is the square of the total center of mass energy of the lepton-proton collision ($s = 90200$ GeV^2).

The ZEUS detector measures both the scattered positron and the hadronic system. The four independent measured quantities E'_e, θ_e, δ_h and p_{Th}, as described in the previous section, over-constrain the kinematic variables x and Q^2 (or equivalently, y and Q^2).

In order to optimise the reconstruction of the kinematic variables, both the resolution and robustness against possible systematic shifts (stability) of each measured quantity must be considered.

For the present analysis, a new method (PT) is used to reconstruct the kinematic variables. The PT method achieves both superior resolution and stability in x and Q^2 in the full kinematic range covered, in comparison with reconstruction methods used in our previous structure function measurements.

5.1 Characteristics of standard reconstruction methods

As discussed in Sect. 4, the positron variables, E'_e and θ_e are measured with high precision, and the systematic uncertainties are small. The kinematic variables calculated from these quantities are given by:

$$y_e = 1 - \frac{E'_e}{2E_e}(1 - \cos\theta_e), \tag{7}$$

$$Q^2_e = 2E_e E'_e(1 + \cos\theta_e). \tag{8}$$

This method of reconstruction, the electron (EL) method, gives good results at high y, where E'_e is significantly different from the positron beam energy E_e, but at low y ($y \lesssim 0.1$) both the resolution and stability of y_e become poor.

The Jacquet-Blondel (JB) method [27] of kinematic reconstruction only uses information from the hadronic energy flow of the event:

$$y_{JB} = \frac{\delta_h}{2E_e}, \tag{9}$$

$$Q^2_{JB} = \frac{p^2_{Th}}{1 - y_{JB}}. \tag{10}$$

Q^2_e has better resolution than Q^2_{JB} over the entire kinematic range while at low y ($y \lesssim 0.04$), y_{JB} has superior resolution in comparison with y_e. However, unlike the case of the positron measurement, the energy loss of the hadronic system in the passive material in front of the CAL and the loss through the beam holes have to be determined using a simulation of the DIS final states and of the detector effects. This introduces substantial systematic uncertainties.

The Double-Angle (DA) method [28] combines the information from the scattered lepton with that from the produced hadronic system:

$$Q^2_{DA} = 4E^2_e \frac{\sin\gamma_H(1+\cos\theta_e)}{\sin\gamma_H + \sin\theta_e - \sin(\gamma_H + \theta_e)}, \tag{11}$$

$$y_{DA} = \frac{\sin\theta_e(1-\cos\gamma_H)}{\sin\gamma_H + \sin\theta_e - \sin(\gamma_H + \theta_e)}. \tag{12}$$

In this method the hadronic measurement enters the kinematic reconstruction through the variable γ_H (see eq. 4), which depends on the ratio of the measured quantities δ_h and p_{Th}. As a result, uncertainties in the hadronic energy measurement tend to cancel leading to a good stability of the reconstructed kinematic variables. At the highest y, however, y_e has better resolution than y_{DA}. At low y ($\lesssim 0.04$), and low Q^2, the noise in the CAL, which affects both p_{Th} and δ_h has a large effect on Q^2_{DA} and y_{DA}. This region was avoided in our previous analyses, which used the DA method, by imposing the cut $y_{JB} > 0.04$.

5.2 PT method

The PT method provides an improved measurement of y and Q^2 by an efficacious combination of the information from the measurements of both the hadronic system and the positron.

This is done in two steps. In the first step, the transverse momentum balance between the positron and the hadron system is used event by event to correct the hadronic energy measurement of y by using a functional form derived from the MC simulation. In the second step, the advantages of the EL, JB and DA methods are combined into a single reconstruction method for the full kinematic range.

5.2.1 The measurement of y at low y

In an ideal detector, transverse momentum conservation requires $p_{Th} = p_{Te}$ up to the negligible transverse momentum carried by QED initial state radiation. Since the positron is measured in the calorimeter, energy carried by QED final state radiation is mostly included in the measured positron energy. Since p_{Te} is a precisely measured quantity (see above), $p_{Th} - p_{Te}$ gives, for each event, the difference between the measured and the true hadronic transverse momentum. The difference can result from hadronic energy loss through the beam hole and/or in the passive material in front of CAL, as well as from the finite energy resolution of CAL. In first approximation the hadronic energy mismeasurement affects both p_{Th} and δ_h in the same way. Indeed, if the hadronic system consisted of the proton remnant carrying no transverse momentum and a well collimated current jet, then an accurate measurement of y would be obtained by:

$$y_{(1)} = y_{JB}/(\frac{p_{Th}}{p_{Te}}). \tag{13}$$

In this idealised case, a precise measurement of y is achieved by determining the hadronic energy correction directly from the data (on an event by event basis) rather than by a MC simulation.

In standard DIS events, in addition to a current jet, there is hadronic energy flow in the region between the current jet and the direction of the proton remnant [17]. As a result, the simple relationship given by eq. 13 no longer holds and is replaced by:

$$y_{(1)} = y_{JB}/\mathcal{C} \tag{14}$$

where $\mathcal{C}$ is a correction function. In the PT method, $\mathcal{C}$ is determined from MC simulation of final states convoluted with the detector simulation, as a function of the measured quantities $\frac{p_{Th}}{p_{Te}}$, p_{Th} and γ_H giving $\mathcal{C}(\frac{p_{Th}}{p_{Te}}, p_{Th}, \gamma_H)$.

The ratio $\frac{y_{JB}}{y_{gen}}$ averaged over p_{Th}, $\langle\frac{y_{JB}}{y_{gen}}\rangle$, as obtained from the MC simulation, is shown in Fig. 2 as a function of $\frac{p_{Th}}{p_{Te}}$; y_{gen} is the generated value of y. For small values of γ_H, $\langle\frac{y_{JB}}{y_{gen}}\rangle$ rises almost linearly with $\frac{p_{Th}}{p_{Te}}$. This behaviour is as expected from eq. 13 and follows from the fact that the hadronic energy deposit comes mainly from the current jet when γ_H is small. Note that the quantities p_{Th} and y_{JB} are rather insensitive to the energy loss in the forward beam hole. The observed positive offset from unity of $\langle\frac{y_{JB}}{y_{gen}}\rangle$ at $\frac{p_{Th}}{p_{Te}} = 1$ results from the CAL noise. [4]

As γ_H increases $\langle\frac{y_{JB}}{y_{gen}}\rangle$ falls below unity mainly due to energy loss in the passive material in the detector. With increasing γ_H an increasing fraction of p_{Th} is carried by particles produced in the region between the current jet and the proton remnant. The energy loss of these particles enters directly into the measurement of p_{Th} but to a lesser extent into the measurement of y_{JB} (see eqs. 2 and 9). This leads to a less linear dependence of $\langle\frac{y_{JB}}{y_{gen}}\rangle$ on $\frac{p_{Th}}{p_{Te}}$.

As p_{Th} increases the energy flow between the current jet and the remnant becomes relatively less in comparison to the energy flow in the current jet. Thus, as a function of increasing p_{Th}, the $\frac{p_{Th}}{p_{Te}}$ dependence of $\frac{y_{JB}}{y_{gen}}$ becomes more linear (not shown in figure).

[4] As an example of the effect of calorimeter noise on $\langle\frac{y_{JB}}{y_{gen}}\rangle$ at low γ_H, consider the measurement of an event with true $y = 0.01$ and true $Q^2 = 10$ GeV^2. If one calorimeter cell in the RCAL produces a noise signal of 100 MeV, the contribution to the measured y_{JB} amounts roughly to $\frac{200\text{MeV}}{55\text{GeV}} = 0.004$. Ignoring the effects of energy loss and smearing, y_{JB} is reconstructed 40% larger than the true y. The contribution of the same noise signal to the measured p_{Th}, on the other hand, is small (< 0.1 GeV) in comparison with the true $p_T = Q\sqrt{(1-y)} = 3.15$ GeV.

The correction function $\mathcal{C}(\frac{p_{Th}}{p_{Te}}, p_{Th}, \gamma_H)$ is parameterised using second order polynomials to describe the MC simulation of $\frac{y_{JB}}{y_{gen}}$ in the range $0.5 < \frac{p_{Th}}{p_{Te}} < 1.5$ which contains approximately 90% of the events. The curves in Fig. 2 show $\mathcal{C}$, averaged over p_{Th}, as a function of $\frac{p_{Th}}{p_{Te}}$ for several values of γ_H.

Application of the correction function, eq. 14, determines y based on the *measured* values of $\frac{p_{Th}}{p_{Te}}$, p_{Th} and γ_H, which reduces the dependence of the y measurement on the MC simulation. At the same time, by compensating for the deviations of the hadronic energy measurement from the true values for each event individually, the resolution of the y measurement is improved. It will be shown in Sect. 7.1, in the studies of systematic uncertainties, that the structure function results do not depend strongly on the details of the MC simulation of the DIS final states used in determining the correction function.

5.2.2 Kinematic measurement in the full y range

When the current jet points in the backwards direction ($\gamma_H \gtrsim 90°$), corresponding to the region of high y, the hadronic system becomes less collimated, and the particle loss through the rear beam hole is not negligible. These particles carry a small amount of transverse momentum but make a large contribution to the decrease in δ_h and therefore to the decrease in y_{JB}. As a result the ratio $\frac{p_{Th}}{p_{Te}}$ is less effective for determining the correction to the hadronic measurement of y. This can be seen in Fig. 2, where for $\gamma_H > 120°$, there is little dependence of $\langle \frac{y_{JB}}{y_{gen}} \rangle$ on $\frac{p_{Th}}{p_{Te}}$.

The measurement of y from the positron (see eq. 7) at high y does not suffer from these deficiencies and provides an accurate measurement. Applying the Σ-correction, first introduced in ref. [29] and used by H1 [2], $y_{(1)}$ and y_e are combined:

$$y_{(2)} = y_{(1)} \frac{1}{y_{(1)} + 1 - y_e}. \tag{15}$$

At this stage, the best estimate for the transverse momentum of the hadronic system is p_{Te} and for the hadronic sum $\sum_h (E_h - p_{Zh})$ is $2E'_e y_{(2)}$. This allows the calculation of the hadronic angle, γ_{PT}, as follows:

$$\cos\gamma_{PT} = \frac{p_{Te}^2 - 4E_e^2 y_{(2)}^2}{p_{Te}^2 + 4E_e^2 y_{(2)}^2}. \tag{16}$$

Since the Double-Angle method is the method least sensitive to energy scales, the kinematic variables are calculated using eqs. 11 and 12 substituting γ_{PT} for γ_H.

The kinematic variables determined in this way will be denoted by the subscript PT. Figure 3a shows the distributions of $\frac{y_{JB}}{y_{gen}}$, $\frac{y_{(1)}}{y_{gen}}$, $\frac{y_{(2)}}{y_{gen}}$ and $\frac{y_{PT}}{y_{gen}}$ for several ranges in γ_H. By construction, the correction from y_{JB} to $y_{(1)}$ centers the distribution around unity, while the further corrections yield improvements in resolution. Figure 3b shows the distributions of $\frac{y_{PT}}{y_{gen}}$ together with $\frac{y_{DA}}{y_{gen}}$ and $\frac{y_e}{y_{gen}}$. The corresponding distributions for the Q^2 reconstruction are shown in Fig. 3c. Both in y and Q^2 the resolution of the PT method is superior to all other methods. Also shown in Fig. 3c is the result for $Q^2_{(2)} (= \frac{p_{Te}^2}{1-y_{(2)}})$. The resolution of this alternative method to reconstruct Q^2 is inferior to the resolution of the PT method.

For large y one can check the method by comparing y_{PT} with y_e. Figure 4a and b show the distributions of $\frac{y_{PT}}{y_e}$ for the regions $140^\circ < \gamma_H < 160^\circ$ and $160^\circ < \gamma_H < 180^\circ$ where y_e is expected to give a reasonable estimate of y . Also shown in Fig. 4 are the expectations from the MC simulation. The r.m.s. widths ($\sigma = 9\%$ for $160^\circ < \gamma_H < 180^\circ$ and $\sigma = 20\%$ for $140^\circ < \gamma_H < 160^\circ$) of the distributions are in good agreement with the MC simulation and are dominated by the error on the measurement of y_e . There are small shifts of about 2% between the data and MC simulation. These shifts are included in the study of the systematic uncertainties.

6 Event selection

The following cuts were used to select NC DIS events:

- A positron candidate identified as described in Sect. 4.1.
- $E'_e > 10$ GeV, where E'_e is the corrected positron energy. This cut ensures high and well understood positron finding efficiency and suppresses background from photoproduction.
- 38 GeV $< \delta <$ 65 GeV, where $\delta = \sum_i (E_i - p_{Zi})$. Here the sum runs over *all* calorimeter cells, i.e. including those belonging to the identified positron. This cut removes events with large initial state radiation and further reduces the background from photoproduction.
- A track match for $\theta < 135^\circ$. This condition suppresses events from cosmic rays, halo-muons, photoproduction and DIS events where an electromagnetic shower has been falsely identified as the scattered positron.
- $y_e < 0.95$. This condition removes events where fake positrons are found in the FCAL.

A total of 680283 events pass the above cuts.

- Box cut. Events with a scattered positron impact point in the RCAL inside a box of 26 cm $\times$ 26 cm around the beampipe are rejected. This ensures that the impact point is at least 2.5 cm away from the edge of the RCAL and therefore guarantees full containment of the electromagnetic shower in the calorimeter.
- -50 cm $< Z_{vertex} <$ 100 cm. This cut is performed for events with a reconstructed tracking vertex and suppresses beam-gas background events and the small fraction of the events where the vertex position is incorrectly measured. Events without a tracking vertex are assigned the mean vertex Z position and are accepted.

After these additional cuts a sample of 443421 events remains.

- $\frac{p_{Th}}{p_{Te}} > 0.3 - 0.001\gamma_H$ (γ_H in degrees). For the PT method to yield a reliable measurement of x and Q^2 the loss in hadronic transverse momentum must be limited. There are events where a substantial part of the current jet remains in the forward beampipe. These events, which are produced at small γ_H , can be falsely reconstructed at large γ_H due to the CAL noise. This cut suppresses such events.

A total of 400627 events pass all the above selection cuts. For the accepted events Fig. 5a,b show, respectively, the measured energy and scattering angle of the positron. Figure 5c shows the reconstructed vertex distribution before applying the vertex cut and Fig. 5d-f show the distribution of $\frac{p_{Th}}{p_{Te}}$, where the $\frac{p_{Th}}{p_{Te}}$ cut was removed, for three ranges in γ_H . The energy, angle, vertex and transverse momentum distributions are well reproduced by the MC simulation (also indicated in the figures). To obtain these distributions the MC events have been reweighted to the structure function obtained from the QCD NLO fit described below.

Figure 6 shows the distributions in y_{PT}, x_{PT}, Q^2_{PT} and γ_{PT} together with the MC distributions normalised to the integrated luminosity of the data. Good agreement is obtained except for the region around $y \sim 10^{-2}$ where the MC undershoots the data by up to $\sim 5\%$. Equivalent deviations are observed in the x_{PT} and γ_{PT} distributions. This difference is not concentrated at a specific value of Q^2 and has a negligible effect on the values of the extracted structure function.

Figure 7a shows the distribution of events in the (x,Q^2) plane. The (x,Q^2) bins used for the determination of the structure function are shown in Fig. 7b. The bins have been chosen commensurate with the resolutions. At large Q^2 and also at low y larger bin sizes have been chosen to obtain adequate statistics in each bin and to minimise bin-to-bin migrations as a result of the non-Gaussian tails. Furthermore, large acceptance ($A > 20\%$) and purity ($P > 30\%$) [5] are required for each bin. The lowest values of acceptance occur at the lowest Q^2 values where the box cut becomes effective. The bins with lowest purity occur at the lowest y values. In the majority of bins the acceptance is greater than 80% and the purity is greater than 50%.

Figure 8 shows the distributions in $(\frac{x_{PT}-x_{gen}}{x_{gen}})$ and $(\frac{Q^2_{PT}-Q^2_{gen}}{Q^2_{gen}})$ for a number of bins in the (x,Q^2) plane, where x_{gen} and Q^2_{gen} are the generated values of x and Q^2. The resolutions vary smoothly with x and Q^2. The resolution in x decreases from $\sigma_x \approx 25\%$ for low y ($y = \frac{Q^2}{xs}$) to $\sigma_x \approx 10\%$ for large y. The resolution in Q^2 is $\sigma_{Q^2} \approx 10\,\%$ for large y and improves to $\sigma_{Q^2} \approx 5\,\%$ for intermediate and low y. At the lowest y values tails appear due to the vertex finding efficiency and resolution.

The numbers of events in each of the bins are given in Table 1.

The final sample contains a small number of background events which are not due to deep inelastic neutral current scattering:

- Non-ep background. The level of background not associated with ep collisions is determined from the number of events observed in unpaired or empty bunches. This background is subtracted statistically taking into account the appropriate ratios of bunch currents and numbers of bunches. It amounts to less than 1% in all bins. For events in the bins of $Q^2 > 1000$ GeV^2 all events were scanned visually and no non-ep events were found.

- Photoproduction background. The events from the photoproduction MC code PYTHIA were analysed in the same way as the data and the number of events passing the selection cuts in each bin was determined. This number is subtracted taking into account the ratio

[5] Acceptance is defined as the ratio of the number of events which are reconstructed to the number of generated events in a bin. Purity is defined as the fraction of reconstructed events in a bin which originated from the same bin.

of equivalent luminosity of the data and the MC samples. As a check the δ distributions for each of the bins were fitted to a shape extracted from MC DIS events and a Gaussian shape, which parameterises the photoproduction events (the procedure is described in [1]). The δ distribution for $y > 0.2$ is shown in Fig. 9. Also given are the MC expectations for DIS (solid histogram) and for photoproduction (dashed histogram). The flattening of the MC prediction for photoproduction at $\delta < 38$ GeV is artificial and results from the cut of $W > 190$ GeV applied at the generator level. In the region $\delta < 38$ GeV the photoproduction contribution can be measured directly through events tagged by the LUMI positron tagger (the acceptance for these events tends to zero for $\delta > 40$ GeV). The result of this measurement is shown in Fig. 9. Also shown is the result of the fit to the data (dashed-dotted curve) using the shape from the DIS MC distribution plus a Gaussian contribution (dotted curve) for the photoproduction background. The Gaussian contribution agrees with the MC photoproduction estimate for $\delta > 38$ GeV and with the measured photoproduction background. For $Q^2 > 1000$ GeV^2, the visual scan found at most two events showing topologies consistent with photoproduction events.

The total background contribution to each bin is given in Table 1. The maximum background fraction of about 6% occurs in bins of high y.

7 Proton structure function F_2

In deep inelastic scattering the double differential cross section for inclusive e^+p scattering is given in terms of the structure functions F_i:

$$\frac{d^2\sigma}{dx\ dQ^2} = \frac{2\pi\alpha^2}{xQ^4}\left[Y_+F_2(x,Q^2) - y^2F_{_L}(x,Q^2) - Y_-xF_3(x,Q^2)\right](1+\delta_r(x,Q^2)) \qquad (17)$$

where $Y_\pm = 1 \pm (1-y)^2$ and x and Q^2 are defined at the hadronic vertex . In this equation $F_{_L}$ is the longitudinal structure function, F_3 is the parity violating term arising from the Z° exchange and δ_r is the electroweak radiative correction. Since all of these contributions to the cross section are expected to be small in the kinematic region of the present measurement, this can be rewritten as:

$$\frac{d^2\sigma}{dx\ dQ^2} = \frac{2\pi\alpha^2Y_+}{xQ^4}F_2(x,Q^2)(1-\delta_{_L}-\delta_3)(1+\delta_r). \qquad (18)$$

The F_2 structure function itself contains contributions from virtual photon and Z° exchange:

$$F_2 = F_2^{em} + \frac{Q^2}{(Q^2+M_Z^2)}F_2^{int} + \frac{Q^4}{(Q^2+M_Z^2)^2}F_2^{wk} = F_2^{em}(1+\delta_{_Z}) \qquad (19)$$

where M_Z is the mass of the Z° and F_2^{em}, F_2^{wk} and F_2^{int} are the contributions to F_2 due to photon exchange, Z° exchange and γZ° interference respectively. We finally write:

$$\frac{d^2\sigma}{dx\ dQ^2} = \frac{2\pi\alpha^2Y_+}{xQ^4}F_2^{em}(1+\delta_{_Z})(1-\delta_{_L}-\delta_3)(1+\delta_r). \qquad (20)$$

The corrections, $\delta_{r,Z,3,L}$, are functions of x and Q^2 but are, to a good approximation, independent of F_2, i.e. they are insensitive to the parton density distributions.

In this analysis we determine the structure function F_2. In the Standard Model the difference between F_2 and F_2^{em} is expected to be less than 1% for values of $Q^2 < 1000$ GeV^2. At higher Q^2 the difference becomes progressively larger. In this region therefore we present the values of F_2^{em} as well as F_2. These are extracted from F_2 through the correction δ_Z using the MRSA[21] parton distribution functions.

An iterative procedure is used to extract the structure function F_2. Monte Carlo events are generated according to eq. 17 and so contain transverse and longitudinal photon and Z° contributions as well as radiative effects. In each step of the iteration the value of F_2 in a bin can be obtained from the ratio of observed events in the data to the number of events observed in the MC simulation and the calculated values of $\delta_{r,Z,3,L}$. In the first step the acceptance correction is taken from the MC simulation which uses the parton distributions given by MRSA. The result for F_2 from this first iteration is used for a QCD fit using the DGLAP [30] evolution equations in next-to-leading order (QCD NLO fit) in a manner very similar to that described in [31]. The evolution uses massless quarks of three flavours in the proton and the charm quark coefficient functions from references [32, 33] to ensure a smooth crossing of the charm threshold. The NMC [34] data for $Q^2 > 4$ GeV^2 are used to constrain the QCD NLO fit at high x ($\gtrsim 10^{-2}$). The fit also includes the low Q^2 1994 data from this experiment [3].

The parton distributions from the QCD NLO fit are used to recalculate the cross section, including the new F_L contribution as a function of x and Q^2. The MC events are reweighted using the calculated cross sections and the true hadronic x and Q^2. This reweighted MC is then used to perform the acceptance correction bin by bin to the data, leading to a new estimate of F_2, specified at the mean values of x and Q^2 in each bin. The procedure is repeated until the F_2 values from two consecutive iterations change by less than 0.5%. The final result is reached in three iterations. The functional form of the QCD NLO fit is used to quote the results for F_2 at x and Q^2 values which are chosen to be convenient for comparisons with other F_2 measurements. Using alternative parametrisations for this correction has negligible effect on the measured F_2. It should be noted that the QCD NLO fit is used here only as a parameterisation to obtain a stable acceptance correction and not to perform a detailed QCD analysis.

The statistical errors of the F_2 values are calculated from the number of events measured in the bins, including those from the background subtraction, and the statistical error from the MC simulation. Since we are using bin by bin corrections, the correlations of statistical errors between the F_2 measurements enter only via the finite statistics of the MC sample. The correlations are small given the relatively large MC sample used in this analysis. A correlation between the F_2 values of neighbouring bins is present due to acceptance and smearing effects. The sensitivity of the measured F_2 to these effects has been checked by comparing the F_2 obtained from the first iteration with the final value. The changes were within the statistical errors of the final F_2 values.

The correction δ_L is determined using the QCD prescription for F_L [35] and the parton distributions from the QCD NLO fit. It is significant only in the region of large y where it reaches 12%(see Table 1). The δ_Z and δ_3 corrections are calculated from the MRSA parametrisation of the parton distributions. These corrections are negligible for values of Q^2 below 1000 GeV^2. For values of Q^2 above 1000 GeV^2 they strongly increase with increasing Q^2 and have a slight dependence on y. For the two highest Q^2 bins the corrections are:

- $Q^2 = 3000$ GeV^2,

  $x = 0.20$: $\delta_{_Z} = +4\%$ and $\delta_3 = +5\%$

  $x = 0.08$: $\delta_{_Z} = +5\%$ and $\delta_3 = +8\%$

- $Q^2 = 5000$ GeV^2,

  $x = 0.20$: $\delta_{_Z} = +7.5\%$ and $\delta_3 = +11\%$

  $x = 0.08$: $\delta_{_Z} = +8\%$ and $\delta_3 = +22\%$.

The F_2 values are corrected for higher order QED radiative effects not included in HERACLES. These corrections, including soft photon exponentiation, were evaluated using the program HECTOR in the leading log approximation [36]. They vary smoothly with Q^2 between 0.2% and 0.5%.

7.1 Systematic uncertainties

Several factors contribute to the systematic uncertainties in the measurements of F_2. In the following they are subdivided into six independent categories. For each category we summarise the checks that have been performed to estimate the size of the uncertainty. Figure 10 shows the size of the systematic uncertainties plotted as a function of y for the six categories and also the total systematic error. For reference (see appendix) each test applicable at $Q^2 < 100$ GeV^2 or $y < 0.01$ is numbered; the number is given in brackets {}.

1 Positron finding and efficiency

- The positron identification efficiency is varied within the uncertainty found in the QED Compton study which is ~3% for positron energies $E'_e = 10$ GeV and negligible for energies above 14 GeV {1,2}. The effects on F_2 are negligible except in the lowest x bins where they reach ~3%.

  The parameters of SINISTRA94 are varied to check the effects from overlaps of energy deposits from the hadronic final state with those of the scattered positron {1}. This results in changes of F_2 of ~4%, again in the lowest x bins.

  For $\theta_e < 135°$, where a track is required to match with the CAL positron position, a comparison of the number of rejected events in MC and data can accommodate a possible mismatch in efficiency of at most ±2.5%.

  In addition, an alternative electron finder employed in a previous analysis is used [1]. Consistent results are obtained over the full energy range.

2 Positron scattering angle

- Changing the box cut from 26 cm × 26 cm to 28 cm × 28 cm in both data and MC {3,4} has a small effect on the F_2 at low values of $Q^2 (\leq 15$ GeV) and are negligible elsewhere.

  The systematic uncertainty in the position of the scattered positron is estimated from the difference between the extrapolated track position at the face of the CAL

and the position found from the CAL or the SRTD. In the region of the SRTD these uncertainties are about 1 mm. They are 2 mm outside the SRTD. The largest systematic error is obtained if the relative distance between the two halves of the RCAL is changed by ± 2 mm {5,6}.

For positions determined by the RCAL we additionally changed the distance of the measured impact point with respect to the beam-line by ± 2 mm {7,8}.

For positron angles measured by the tracking detector, the scattering angle θ_e is changed by the estimated systematic uncertainty of the track angle of $\pm 0.2°$.

These changes were made in the data while leaving the MC simulation unchanged. This had an effect of about 1% on the measured F_2.

- The absolute vertex reconstruction efficiency in the MC simulation is decreased by 1% overall {9} or increased by 3% for $\gamma_H < 40°$ {10}. These changes are motivated by the study of the efficiency as a function of the hadronic angle (see Fig. 1e). Also, the cut on the Z_{vertex} position is tightened by demanding –28 cm $< Z_{vertex} <$ 40cm to estimate a possible uncertainty from the luminosity of the events in the satellite bunch {11}. Effects on the measured F_2 are typically 1-2%.

  As an additional check, we required that the vertex determined from the CAL timing was –40 cm $< Z_{vertex}^{timing} <$ 30 cm for the events that had no tracking vertex. The effects on the measured F_2 are similar to those described above and are not included in the final systematic uncertainties.

3 Positron energy scale

- The systematic uncertainties in F_2 due to the uncertainties in the absolute calorimeter energy calibration for scattered positrons is estimated by changing the energy scale in the RCAL in the MC simulation by 2% at 10 GeV linearly decreasing to 1% at 27.5 GeV. For BCAL the energy scale is modified by $\pm 2\%$. The magnitude of these shifts represents our present understanding of the positron energy measurement (see Sect. 4) {12,13}. Systematic variations in F_2 of 1-2% are observed.

4 Hadronic energy measurement

- The energy scale in the MC simulation is changed by $\pm 3\%$ while leaving the positron energy scale unchanged {14,15}. The value of 3% is based on detailed comparisons of the distributions of the quantity $\frac{p_{Th}}{p_{Te}}$ from data and MC (see Fig. 5d-f) and on the deviation of the mean of $\frac{y_{PT}}{y_e}$ from unity for high y (see Fig. 4). The effects on F_2 are typically 4% in the bins at very high and very low y, while the effects are about 1% at moderate y. In addition the energy scales of the different calorimeter parts are changed independently by 3% in turn {16-19}, which resulted in similar effects on F_2.
- The noise cut on isolated EMC(HAC) cells of 100(150) MeV was changed in the MC simulation by ± 10 MeV which reflects the uncertainty in the MC simulation of low energy deposits in the CAL and the modeling of the uranium radioactivity {20,21}. Variations in F_2 of up to 25% are observed in the bins at very low y. Elsewhere the variations in F_2 are within 2%.

5 Hadronic energy flow

- The correction function, $\mathcal{C}(\frac{p_{Th}}{p_{Te}}, p_{Th}, \gamma_H)$, depends on the hadronic energy flow. The correction function was also determined using a MC simulation which uses the LEPTO MEPS model for the description of the hadronic final state, instead of CDMBGF. This model also provides a reasonable description of the hadronic energy flow in DIS events [17]. The new correction function was applied to the data. Acceptance corrections were then made with the sample of CDMBGF MC events with the original correction function applied {22}. The changes in F_2 are typically 2% in all bins.
- The hadronic energy flow for diffractive events is different to that for non-diffractive events. To investigate the sensitivity of the PT method to the size of the diffractive component we reweighted the diffractive scattering cross section in the MC simulation such that it agrees with the measurements of [37] while leaving the correction function $\mathcal{C}$ unchanged {23}. As a separate check, to allow for possible additional diffractive-like events we increased the diffractive cross section by an additional 100%{24}. Effects at the 2% level in F_2 are observed in each check.
- The fraction of events removed by the $\frac{p_{Th}}{p_{Te}}$ cut is sensitive to the amount of p_{Th} lost in the forward beampipe and so also to the details of the fragmentation. We removed the $\frac{p_{Th}}{p_{Te}}$ cut, while extending the correction curves to include the region of very low $\frac{p_{Th}}{p_{Te}}${25}. This resulted in changes of 3% percent at low y.
- We determined the correction functions without allowing for a dependence on p_{Th} {26}, resulting in changes of less than 2 % in F_2 . Reducing, by a factor of two, the size of γ_H intervals in which the correction function is determined resulted in changes of typically 1-2%{27}.

6 Background subtraction

- As described above, the photoproduction background as given by the PYTHIA MC simulation agrees with the determination from the fitting procedure described in section 6 (see Fig. 9), which in turn agrees with the photoproduction contribution extracted from events tagged by the LUMI positron detector. Uncertainties in the LUMI positron detection efficiency, the assumed shape in the fitting procedure and the positron misidentification in the PYTHIA MC simulation lead to an overall uncertainty in the photoproduction background of $\pm$50%{28,29}. This results in an uncertainty in F_2 which is at most 3% for high y and negligible elsewhere.

The total systematic uncertainty for all bins is determined by adding in quadrature separately the positive and negative deviations from the above mentioned categories.

At high Q^2 ($>$ 100 GeV^2), a significant contribution to the apparent systematic deviations is due to the limited number of events in the data. From the lower Q^2 region we know that the systematic uncertainties depend mainly on y. Therefore, all bins with $Q^2 >$ 100 GeV^2 and $y > 0.01$ are combined, for the systematic error determination, in fixed y intervals. The uncertainty in the track matching efficiency contributes only at $Q^2 >$ 350 GeV^2 and is taken into account separately.

Figure 10 shows the positive and negative systematic errors for each bin with $Q^2 <$ 100 GeV^2 as a function of y. For the majority of the bins the total systematic uncertainty is below 5%. As

y increases above $y = 0.5$ the uncertainty grows to around 10%. For $y < 0.01$ the uncertainty increases mainly because of the CAL noise.

The combined results for the bins with $Q^2 > 100$ GeV^2 are also shown.

The systematic errors do not include the uncertainty in the measurement of the integrated luminosity ($\pm 1.5\%$), the overall trigger efficiency ($\pm 1.0\%$) or the uncertainty due to higher order electroweak radiative corrections ($\pm 0.5\%$). These effects lead to a combined uncertainty of 2% on the overall normalisation of F_2.

In addition to the above studies a complete analysis was done using the electron (EL) method of kinematic reconstruction. In the region of high y, where this method is reliable, the results were compatible with this analysis.

8 Results

The values of F_2 are given in Tables 1 and 2 together with their systematic and statistical uncertainties. In the appendix we give the F_2 values with $Q^2 < 100$ GeV^2 or $y < 0.01$ obtained from each systematic check used in the calculation of the systematic uncertainties. Also shown in Tables 1 and 2 are the number of events and the estimated number of background events in each bin as well as the correction due to the longitudinal structure function, $\delta_{_L}$. The F_2 values are displayed versus x for fixed values of Q^2 in Fig. 11 together with the low Q^2 data from our experiment [3] and the high x results from NMC [34]. The rise of F_2 for $x \to 0$ is measured with much improved precision. Also shown is the result of the QCD NLO fit used for the acceptance determination. The data from this analysis at large x reach the x range covered by the fixed target experiments. In the overlap region the agreement is good. The results agree well with the recently published results of the H1 collaboration [4] in the kinematic region where the data sets overlap.

Figure 12 shows the F_2 values as a function of Q^2 for fixed x. Scaling violations are observed, which decrease as x increases. The Q^2-range of the ZEUS data has increased substantially with respect to our previous data. The data now span more than a decade in Q^2 for x values as low as $x = 4 \cdot 10^{-4}$ and almost three decades at $x \approx 0.1$.

In Fig. 13 the data are shown together with the NLO predictions of GRV94 [38] and the NLO parameterisations MRSA′ [21] and CTEQ3 [39]. The data of the fixed target experiments [34, 40, 41, 42] are also shown. At large Q^2 all parameterisations represent the data well. For $Q^2 \lesssim 45$ GeV^2 CTEQ3 undershoots the measured F_2 values in the region $10^{-4} \lesssim x \lesssim 10^{-2}$. MRSA′ overshoots the data below $x = 10^{-3}$ at low Q^2 ($Q^2 \lesssim 8.5$ GeV^2), whereas GRV94 overshoots the data at $Q^2 \lesssim 18$ GeV^2 and $x < 10^{-3}$. Our QCD NLO fit reproduces the data over the full kinematic range indicating that NLO DGLAP evolution can give a consistent description of the data. The details of this fit will be included in a forthcoming paper.

9 Conclusions

We have presented new measurements of the proton structure function F_2 from an analysis of inelastic positron proton neutral current scattering using data obtained with the ZEUS detector

at HERA during 1994. A new method for determining the event kinematics has allowed us to measure F_2 over a substantially larger phase space than before by this experiment and with systematic uncertainties reduced to below 5% in most of the (x, Q^2) space. The data cover Q^2 values between 3.2 and 15000 GeV^2 and x values between $5 \cdot 10^{-5}$ and 0.8.

At large x values and Q^2 values up to 70 GeV^2, where the new data reach the x-range covered by fixed-target experiments, good agreement with these experiments is observed. The data show the rise of F_2 towards small x with much improved precision. Strong scaling violations are observed for $x < 0.02$. The measured x-Q^2 behaviour of F_2 can be described by QCD using NLO DGLAP evolution in the full kinematic range.

10 Acknowledgements

The strong support and encouragement of the DESY Directorate has been invaluable. The experiment was made possible by the inventiveness and the diligent efforts of the HERA machine group. The design, construction and installation of the ZEUS detector have been made possible by the ingenuity and dedicated efforts of many people from inside DESY and from the home institutes who are not listed as authors. Their contributions are acknowledged with great appreciation. Useful conversations with J. Blümlein, S. Riemersma, H. Spiesberger and J. Smith are also gratefully acknowledged.

References

[1] ZEUS Collab., M. Derrick et al., Phys. Lett. B316 (1993) 412;
ZEUS Collab., M. Derrick et al., Z. Phys. C65 (1995) 379.

[2] H1 Collab., I. Abt et al., Nucl. Phys. B407 (1993) 515;
H1 Collab., T. Ahmed et al., Nucl. Phys. B439 (1995) 471.

[3] ZEUS Collab., M. Derrick et al., Z. Phys. C69 (1996) 607.

[4] H1 Collab., S. Aid et al., DESY 96-039 (1996).

[5] ZEUS Collab., M. Derrick et al., Phys. Lett. B293 (1992) 465;
ZEUS Collab., M. Derrick et al., Z. Phys. C63 (1994) 391.

[6] ZEUS Collab., The ZEUS Detector, Status Report 1993, DESY 1993.

[7] M. Derrick et al., Nucl. Inst. Meth. A309 (1991) 77;
A. Andresen et al., Nucl. Inst. Meth. A309 (1991) 101;
A. Bernstein et al., Nucl. Inst. Meth. A336 (1993) 23.

[8] C. Alvisi et al., Nucl. Inst. Meth. A305 (1991) 30.

[9] N. Harnew et al., Nucl. Inst. Meth. A279 (1989) 290;
B. Foster et al., Nucl. Phys. B (Proc. Suppl.) 32 (1993) 181;
B. Foster et al., Nucl. Inst. Meth. A338 (1994) 254.

[10] J. Andruszków et al., DESY 92-066 (1992).

[11] W.H. Smith et al., Nucl. Inst. Meth. A 355 (1995) 278.

[12] GEANT 3.13: R. Brun et al., CERN DD/EE/84-1 (1987).

[13] HERACLES 4.4 (and private communication): K. Kwiatkowski, H. Spiesberger and H.-J. Möhring, Proceedings of the Workshop on Physics at HERA, DESY (1992) 1294.

[14] Y. Azimov, Y. Dokshitzer, V. Khoze, S. Troyan, Phys. Lett. B165 (1985) 147;
G. Gustafson, Phys. Lett. B175 (1986) 453;
G. Gustafson, U. Pettersson Nucl. Phys. B306 (1988) 746;
B. Andersson, G. Gustafson, L. Lönnblad, U. Pettersson Z. Phys. C43 (1989) 625.

[15] ARIADNE 4.0: L. Lönnblad, Comp. Phys. Comm. 71 (1992) 15;
L. Lönnblad, Z. Phys. C65 (1995) 285.

[16] JETSET 7.4: T. Sjöstrand and M. Bergtsson, Comp. Phys. Comm. 43 (1987) 367.

[17] ZEUS Collab., M. Derrick et al., Z. Phys. C59 (1993) 231;
ZEUS Collab., M. Derrick et al., Phys. Lett. B338 (1994) 483.

[18] ZEUS Collab., M. Derrick et al., Phys. Lett. B315 (1993) 481.

[19] H1 Collab., T. Ahmed et al., Nucl. Phys. B429 (1994) 477.

[20] ZEUS Collab., M. Derrick et al., Z. Phys. C68 (1995) 569.

[21] A.D. Martin, W.J. Stirling and R.G. Roberts, Phys. Rev. D50 (1994) 6734.

[22] A.D. Martin, W.J. Stirling and R.G. Roberts, Phys. Rev. D51 (1995) 4756.

[23] LEPTO 6.1: G. Ingelman, Proceedings of the Workshop on Physics at HERA, DESY (1991) 1366.

[24] PYTHIA 5.7: H.-U. Bengtsson and T. Sjöstrand, Comp. Phys. Comm. 46 (1987) 43;
T. Sjöstrand, CERN TH-7112-93, (1994).

[25] H. Abramowicz, E.M. Levin, A. Levy and U. Maor, Phys. Lett. B269 (1991) 465.

[26] H. Abramowicz, A. Caldwell and R. Sinkus, Nucl. Inst. Meth. A365 (1995) 508.

[27] F. Jacquet and A. Blondel, Proceedings of the study of an ep facility for Europe, DESY 79/48 (1979) 391.

[28] S. Bentvelsen, J. Engelen and P. Kooijman, Proceedings of the Workshop on Physics at HERA, DESY (1992), 23.

[29] U. Bassler and G. Bernardi, Nucl. Instr. and Meth. A361 (1995) 197.

[30] V.N. Gribov and L.N. Lipatov, Sov. J. Nucl. Phys. 15 (1972) 438, 675;
L.N. Lipatov, Sov. J. Nucl. Phys. 20 (1975) 95;
Yu. L. Dokshitzer, Sov. Phys. JETP 46 (1977) 641;
G. Altarelli and G. Parisi, Nucl. Phys. B126 (1977) 298.

[31] ZEUS Collab., M. Derrick et al., Phys. Lett. B345 (1995) 576.

[32] E. Laenen, S. Riemersma, J. Smith, and W.L. van Neerven, Nucl. Phys. B392 (1993) 229.

[33] M. Glück, E. Reya, and M. Stratmann, Nucl. Phys. B422 (1994) 37.

[34] NMC Collab., M. Arneodo et al., Phys. Lett. B364 (1995) 107.

[35] G. Altarelli and G. Martinelli, Phys. Lett. B76 (1978) 89.

[36] HECTOR 1.00 (and private communication): A. Arbuzov et al., Comp. Phys. Comm. 94 (1996) 128.

[37] ZEUS Collab., M. Derrick et al., DESY 96-018 (1996).

[38] M. Glück, E. Reya and A. Vogt, Z. Phys. C53 (1992) 127;
M. Glück and E. Reya, Dortmund DO-TH 93/27 (1993);
M. Glück, E. Reya and A. Vogt, Phys. Lett. B306 (1993) 391;
M. Glück, E. Reya and A. Vogt, Z. Phys. C67 (1995) 433.

[39] R. Brock et al., Rev. Mod. Phys. 67 (1995) 157.

[40] E665 Collab., M.R. Adams et al., FERMILAB-PUB-95-396-E.

[41] BCDMS Collab.,A.C. Benvenuti et al., Phys. Lett. B223 (1989) 490.

[42] L.W. Whitlow et al., Phys.Lett. B282 (1992) 475.

Table 1: *The measured F_2 values. The values of x and Q^2 at which F_2 are determined are shown outside the brackets, while the bin boundaries are shown inside the brackets. The number of events in each bin as well as the estimated number of background events are given. The corrections for F_L, δ_L (see eq. 18), are also given.*

$x(range)$	N_{ev}	N_{bg}	$F_2 \pm stat^{+sys}_{-sys}$	$\delta_L\%$
$Q^2 = 3.5\ (3.2-4.0)\ \mathrm{GeV}^2$				
$6.3(5.0-8.0)10^{-5}$	2196	101	$0.875 \pm 0.052^{+0.083}_{-0.101}$	7.8
$1.0(0.8-1.3)10^{-4}$	3721	128	$0.939 \pm 0.040^{+0.063}_{-0.072}$	2.4
$Q^2 = 4.5\ (4.0-5.0)\ \mathrm{GeV}^2$				
$1.0(0.8-1.3)10^{-4}$	5131	211	$1.030 \pm 0.028^{+0.061}_{-0.053}$	4.5
$1.6(1.3-2.0)10^{-4}$	4671	103	$1.038 \pm 0.028^{+0.037}_{-0.034}$	1.5
$2.5(2.0-3.2)10^{-4}$	2967	39	$0.932 \pm 0.029^{+0.031}_{-0.033}$	0.5
$Q^2 = 6.5\ (5.0-7.0)\ \mathrm{GeV}^2$				
$1.0(0.8-1.3)10^{-4}$	3192	179	$1.221 \pm 0.036^{+0.098}_{-0.076}$	11.8
$1.6(1.3-2.0)10^{-4}$	8529	245	$1.138 \pm 0.021^{+0.051}_{-0.034}$	3.6
$2.5(2.0-3.2)10^{-4}$	9101	150	$1.038 \pm 0.018^{+0.021}_{-0.026}$	1.2
$4.0(3.2-5.0)10^{-4}$	6911	50	$0.951 \pm 0.019^{+0.031}_{-0.028}$	0.4
$6.3(5.0-8.0)10^{-4}$	5909	60	$0.841 \pm 0.018^{+0.026}_{-0.017}$	0.2
$1.0(0.8-1.3)10^{-3}$	5278	10	$0.776 \pm 0.017^{+0.036}_{-0.028}$	0.1
$1.6(1.3-2.0)10^{-3}$	4655	20	$0.753 \pm 0.019^{+0.024}_{-0.030}$	0.0
$Q^2 = 6.5\ (5.0-9.0)\ \mathrm{GeV}^2$				
$2.5(2.0-3.2)10^{-3}$	9522	90	$0.645 \pm 0.012^{+0.032}_{-0.024}$	0.0
$4.0(3.2-8.0)10^{-3}$	15723	40	$0.629 \pm 0.009^{+0.018}_{-0.028}$	0.0
$1.6(0.8-3.2)10^{-2}$	16255	20	$0.495 \pm 0.008^{+0.037}_{-0.023}$	0.0
$0.4(0.3-1.3)10^{-1}$	1736	0	$0.403 \pm 0.019^{+0.149}_{-0.073}$	0.0
$Q^2 = 8.5\ (7.0-9.0)\ \mathrm{GeV}^2$				
$1.6(1.3-2.0)10^{-4}$	3666	109	$1.337 \pm 0.037^{+0.060}_{-0.081}$	7.1
$2.5(2.0-3.2)10^{-4}$	6502	132	$1.151 \pm 0.024^{+0.037}_{-0.023}$	2.3
$4.0(3.2-5.0)10^{-4}$	6000	77	$0.993 \pm 0.021^{+0.028}_{-0.019}$	0.8
$6.3(5.0-8.0)10^{-4}$	5983	40	$0.920 \pm 0.019^{+0.014}_{-0.025}$	0.3
$1.0(0.8-1.3)10^{-3}$	5827	50	$0.831 \pm 0.018^{+0.031}_{-0.025}$	0.1
$1.6(1.3-2.0)10^{-3}$	4657	30	$0.704 \pm 0.017^{+0.023}_{-0.015}$	0.0
$Q^2 = 10.0\ (9.0-11.0)\ \mathrm{GeV}^2$				
$1.6(1.3-2.0)10^{-4}$	870	35	$1.359 \pm 0.075^{+0.114}_{-0.078}$	10.9
$2.5(2.0-3.2)10^{-4}$	3904	106	$1.231 \pm 0.032^{+0.043}_{-0.043}$	3.4
$4.0(3.2-5.0)10^{-4}$	4415	57	$1.136 \pm 0.026^{+0.030}_{-0.022}$	1.1
$6.3(5.0-8.0)10^{-4}$	4479	28	$0.968 \pm 0.022^{+0.030}_{-0.021}$	0.4
$1.0(0.8-1.3)10^{-3}$	4370	48	$0.857 \pm 0.021^{+0.024}_{-0.023}$	0.1
$1.6(1.3-2.0)10^{-3}$	3737	10	$0.792 \pm 0.021^{+0.021}_{-0.022}$	0.1
$2.5(2.0-3.2)10^{-3}$	3971	50	$0.715 \pm 0.018^{+0.034}_{-0.028}$	0.0
$Q^2 = 10.0\ (9.0-13.0)\ \mathrm{GeV}^2$				
$6.3(3.2-8.0)10^{-3}$	12284	40	$0.593 \pm 0.008^{+0.022}_{-0.021}$	0.0
$1.6(0.8-3.2)10^{-2}$	15549	30	$0.517 \pm 0.007^{+0.013}_{-0.009}$	0.0

Table 1 (continued): *The measured F_2 values.*

$x(range)$	N_{ev}	N_{bg}	$F_2 \pm stat^{+sys}_{-sys}$	$\delta_L\%$
$0.8(0.3-1.3)10^{-1}$	3685	0	$0.395 \pm 0.010^{+0.098}_{-0.059}$	0.0
$Q^2 = 12.0\ (11.0-13.0)\ \mathrm{GeV}^2$				
$2.5(2.0-3.2)10^{-4}$	2311	94	$1.300 \pm 0.042^{+0.059}_{-0.057}$	5.4
$4.0(3.2-5.0)10^{-4}$	3052	50	$1.128 \pm 0.031^{+0.036}_{-0.024}$	1.7
$6.3(5.0-8.0)10^{-4}$	3339	20	$1.102 \pm 0.027^{+0.020}_{-0.037}$	0.6
$1.0(0.8-1.3)10^{-3}$	3242	40	$0.903 \pm 0.023^{+0.031}_{-0.029}$	0.2
$1.6(1.3-2.0)10^{-3}$	2668	70	$0.789 \pm 0.023^{+0.028}_{-0.021}$	0.1
$2.5(2.0-3.2)10^{-3}$	2849	10	$0.746 \pm 0.021^{+0.030}_{-0.024}$	0.0
$Q^2 = 15.0\ (13.0-16.0)\ \mathrm{GeV}^2$				
$2.5(2.0-3.2)10^{-4}$	1463	84	$1.559 \pm 0.065^{+0.093}_{-0.105}$	9.5
$4.0(3.2-5.0)10^{-4}$	3247	62	$1.338 \pm 0.035^{+0.051}_{-0.029}$	2.9
$6.3(5.0-8.0)10^{-4}$	3421	65	$1.092 \pm 0.027^{+0.029}_{-0.030}$	1.0
$1.0(0.8-1.3)10^{-3}$	3487	20	$0.992 \pm 0.025^{+0.035}_{-0.034}$	0.3
$1.6(1.3-2.0)10^{-3}$	2978	20	$0.908 \pm 0.024^{+0.021}_{-0.025}$	0.1
$2.5(2.0-3.2)10^{-3}$	3022	0	$0.793 \pm 0.021^{+0.037}_{-0.012}$	0.0
$6.3(3.2-8.0)10^{-3}$	5535	10	$0.662 \pm 0.014^{+0.020}_{-0.025}$	0.0
$Q^2 = 15.0\ (13.0-20.0)\ \mathrm{GeV}^2$				
$1.6(0.8-3.2)10^{-2}$	14175	50	$0.553 \pm 0.007^{+0.014}_{-0.015}$	0.0
$0.8(0.3-1.3)10^{-1}$	5160	0	$0.370 \pm 0.008^{+0.061}_{-0.040}$	0.0
$Q^2 = 18.0\ (16.0-20.0)\ \mathrm{GeV}^2$				
$4.0(3.2-5.0)10^{-4}$	2672	85	$1.438 \pm 0.041^{+0.059}_{-0.037}$	4.5
$6.3(5.0-8.0)10^{-4}$	3006	87	$1.166 \pm 0.031^{+0.038}_{-0.037}$	1.5
$1.0(0.8-1.3)10^{-3}$	3118	39	$1.015 \pm 0.028^{+0.037}_{-0.025}$	0.5
$1.6(1.3-2.0)10^{-3}$	2682	29	$0.932 \pm 0.026^{+0.017}_{-0.028}$	0.2
$2.5(2.0-3.2)10^{-3}$	2737	10	$0.879 \pm 0.024^{+0.027}_{-0.017}$	0.1
$6.3(3.2-8.0)10^{-3}$	4755	0	$0.629 \pm 0.013^{+0.019}_{-0.021}$	0.0
$Q^2 = 22.0\ (20.0-25.0)\ \mathrm{GeV}^2$				
$4.0(3.2-5.0)10^{-4}$	1363	50	$1.507 \pm 0.058^{+0.101}_{-0.095}$	7.5
$6.3(5.0-8.0)10^{-4}$	2568	60	$1.324 \pm 0.037^{+0.033}_{-0.051}$	2.3
$1.0(0.8-1.3)10^{-3}$	2498	8	$1.081 \pm 0.028^{+0.030}_{-0.031}$	0.8
$1.6(1.3-2.0)10^{-3}$	2136	20	$0.930 \pm 0.026^{+0.039}_{-0.025}$	0.3
$2.5(2.0-3.2)10^{-3}$	2240	0	$0.906 \pm 0.025^{+0.020}_{-0.026}$	0.1
$4.0(3.2-5.0)10^{-3}$	1892	0	$0.749 \pm 0.022^{+0.039}_{-0.033}$	0.0
$6.3(5.0-8.0)10^{-3}$	2003	0	$0.701 \pm 0.021^{+0.032}_{-0.020}$	0.0
$Q^2 = 22.0\ (20.0-32.0)\ \mathrm{GeV}^2$				
$1.0(0.8-1.3)10^{-2}$	3613	0	$0.601 \pm 0.013^{+0.018}_{-0.030}$	0.0
$2.5(1.3-5.0)10^{-2}$	9701	0	$0.490 \pm 0.007^{+0.012}_{-0.011}$	0.0
$0.8(0.5-1.3)10^{-1}$	2325	0	$0.338 \pm 0.009^{+0.067}_{-0.050}$	0.0
$Q^2 = 27.0\ (25.0-32.0)\ \mathrm{GeV}^2$				
$6.3(5.0-8.0)10^{-4}$	2314	60	$1.460 \pm 0.041^{+0.047}_{-0.027}$	3.8
$1.0(0.8-1.3)10^{-3}$	2356	35	$1.194 \pm 0.032^{+0.030}_{-0.021}$	1.2

Table 1 (continued): *The measured F_2 values.*

$x(range)$	N_{ev}	N_{bg}	$F_2 \pm stat^{+sys}_{-sys}$	$\delta_L\%$
$1.6(1.3-2.0)10^{-3}$	2060	0	$1.140 \pm 0.033^{+0.030}_{-0.042}$	0.4
$2.5(2.0-3.2)10^{-3}$	1854	11	$0.928 \pm 0.028^{+0.024}_{-0.021}$	0.2
$4.0(3.2-5.0)10^{-3}$	1695	8	$0.765 \pm 0.024^{+0.037}_{-0.018}$	0.1
$6.3(5.0-8.0)10^{-3}$	1709	2	$0.674 \pm 0.021^{+0.021}_{-0.019}$	0.0
$Q^2 = 35.0\ (32.0-40.0)\ \mathrm{GeV}^2$				
$6.3(5.0-8.0)10^{-4}$	966	35	$1.565 \pm 0.073^{+0.066}_{-0.046}$	7.3
$1.0(0.8-1.3)10^{-3}$	1756	25	$1.370 \pm 0.044^{+0.014}_{-0.043}$	2.2
$1.6(1.3-2.0)10^{-3}$	1543	8	$1.149 \pm 0.038^{+0.023}_{-0.028}$	0.7
$2.5(2.0-3.2)10^{-3}$	1631	0	$1.018 \pm 0.032^{+0.040}_{-0.032}$	0.3
$4.0(3.2-5.0)10^{-3}$	1423	0	$0.887 \pm 0.030^{+0.034}_{-0.014}$	0.1
$6.3(5.0-8.0)10^{-3}$	1306	0	$0.749 \pm 0.027^{+0.040}_{-0.013}$	0.0
$1.0(0.8-1.3)10^{-2}$	1307	10	$0.681 \pm 0.025^{+0.013}_{-0.036}$	0.0
$Q^2 = 35.0\ (32.0-50.0)\ \mathrm{GeV}^2$				
$1.6(1.3-2.0)10^{-2}$	2026	0	$0.604 \pm 0.017^{+0.017}_{-0.022}$	0.0
$2.5(2.0-5.0)10^{-2}$	3845	0	$0.570 \pm 0.012^{+0.025}_{-0.007}$	0.0
$0.8(0.5-1.3)10^{-1}$	2323	0	$0.461 \pm 0.013^{+0.054}_{-0.049}$	0.0
$Q^2 = 45.0\ (40.0-50.0)\ \mathrm{GeV}^2$				
$1.0(0.8-1.3)10^{-3}$	1431	25	$1.441 \pm 0.053^{+0.074}_{-0.035}$	3.9
$1.6(1.3-2.0)10^{-3}$	1293	33	$1.178 \pm 0.045^{+0.036}_{-0.045}$	1.3
$2.5(2.0-3.2)10^{-3}$	1390	11	$1.071 \pm 0.037^{+0.016}_{-0.025}$	0.4
$4.0(3.2-5.0)10^{-3}$	1172	10	$0.894 \pm 0.034^{+0.031}_{-0.022}$	0.2
$6.3(5.0-8.0)10^{-3}$	1129	0	$0.804 \pm 0.031^{+0.057}_{-0.033}$	0.1
$1.0(0.8-1.3)10^{-2}$	1108	0	$0.745 \pm 0.029^{+0.031}_{-0.043}$	0.0
$Q^2 = 60.0\ (50.0-65.0)\ \mathrm{GeV}^2$				
$1.0(0.8-1.3)10^{-3}$	790	8	$1.553 \pm 0.073^{+0.067}_{-0.066}$	8.0
$1.6(1.3-2.0)10^{-3}$	1250	8	$1.339 \pm 0.050^{+0.039}_{-0.024}$	2.5
$2.5(2.0-3.2)10^{-3}$	1294	8	$1.100 \pm 0.040^{+0.033}_{-0.030}$	0.8
$4.0(3.2-5.0)10^{-3}$	1166	0	$1.012 \pm 0.039^{+0.022}_{-0.041}$	0.3
$6.3(5.0-8.0)10^{-3}$	1118	0	$0.890 \pm 0.035^{+0.044}_{-0.020}$	0.1
$1.0(0.8-1.3)10^{-2}$	952	0	$0.672 \pm 0.028^{+0.025}_{-0.014}$	0.0
$1.6(1.3-2.0)10^{-2}$	760	0	$0.614 \pm 0.029^{+0.053}_{-0.024}$	0.0
$2.5(2.0-5.0)10^{-2}$	1719	0	$0.627 \pm 0.020^{+0.020}_{-0.010}$	0.0
$0.8(0.5-1.3)10^{-1}$	1391	0	$0.521 \pm 0.019^{+0.046}_{-0.040}$	0.0
$Q^2 = 70.0\ (65.0-85.0)\ \mathrm{GeV}^2$				
$1.6(1.3-2.0)10^{-3}$	862	25	$1.318 \pm 0.062^{+0.066}_{-0.041}$	3.6
$2.5(2.0-3.2)10^{-3}$	1107	20	$1.228 \pm 0.049^{+0.021}_{-0.075}$	1.2
$4.0(3.2-5.0)10^{-3}$	885	0	$0.917 \pm 0.039^{+0.043}_{-0.013}$	0.4
$6.3(5.0-8.0)10^{-3}$	852	10	$0.887 \pm 0.040^{+0.033}_{-0.031}$	0.1
$1.0(0.8-1.3)10^{-2}$	816	0	$0.774 \pm 0.035^{+0.037}_{-0.036}$	0.0
$1.6(1.3-2.0)10^{-2}$	616	0	$0.697 \pm 0.037^{+0.036}_{-0.024}$	0.0
$2.5(2.0-5.0)10^{-2}$	1390	0	$0.607 \pm 0.021^{+0.019}_{-0.025}$	0.0

Table 1 (continued): *The measured F_2 values.*

$x(range)$	N_{ev}	N_{bg}	$F_2 \pm stat^{+sys}_{-sys}$	$\delta_L\%$
$0.8(0.5-1.3)10^{-1}$	1244	0	$0.484 \pm 0.018^{+0.029}_{-0.026}$	0.0
$Q^2 = 90.0\ (85.0-110.0)\ \mathrm{GeV}^2$				
$1.6(1.3-2.0)10^{-3}$	299	0	$1.363 \pm 0.101^{+0.114}_{-0.050}$	6.6
$2.5(2.0-3.2)10^{-3}$	746	8	$1.275 \pm 0.063^{+0.038}_{-0.045}$	2.1
$4.0(3.2-5.0)10^{-3}$	702	8	$1.068 \pm 0.054^{+0.046}_{-0.031}$	0.7
$6.3(5.0-8.0)10^{-3}$	689	0	$0.974 \pm 0.049^{+0.035}_{-0.020}$	0.2
$1.0(0.8-1.3)10^{-2}$	667	0	$0.845 \pm 0.043^{+0.033}_{-0.037}$	0.1
$1.6(1.3-2.0)10^{-2}$	456	0	$0.619 \pm 0.037^{+0.033}_{-0.058}$	0.0
$2.5(2.0-3.2)10^{-2}$	468	0	$0.556 \pm 0.033^{+0.039}_{-0.019}$	0.0
$4.0(3.2-5.0)10^{-2}$	473	0	$0.526 \pm 0.031^{+0.035}_{-0.032}$	0.0
$0.8(0.5-1.3)10^{-1}$	987	0	$0.453 \pm 0.019^{+0.037}_{-0.019}$	0.0
$2.0(1.3-3.2)10^{-1}$	122	0	$0.255 \pm 0.029^{+0.080}_{-0.037}$	0.0
$Q^2 = 120.0\ (110.0-140.0)\ \mathrm{GeV}^2$				
$2.5(2.0-3.2)10^{-3}$	477	8	$1.467 \pm 0.093^{+0.038}_{-0.030}$	4.1
$4.0(3.2-5.0)10^{-3}$	519	17	$1.176 \pm 0.073^{+0.030}_{-0.024}$	1.3
$6.3(5.0-8.0)10^{-3}$	520	0	$1.112 \pm 0.066^{+0.031}_{-0.032}$	0.4
$1.0(0.8-1.3)10^{-2}$	466	0	$0.836 \pm 0.051^{+0.024}_{-0.016}$	0.1
$1.6(1.3-2.0)10^{-2}$	321	0	$0.610 \pm 0.043^{+0.031}_{-0.023}$	0.0
$2.5(2.0-3.2)10^{-2}$	366	0	$0.653 \pm 0.045^{+0.016}_{-0.022}$	0.0
$4.0(3.2-5.0)10^{-2}$	345	0	$0.519 \pm 0.036^{+0.012}_{-0.017}$	0.0
$0.8(0.5-1.3)10^{-1}$	716	0	$0.451 \pm 0.022^{+0.019}_{-0.019}$	0.0
$2.0(1.3-3.2)10^{-1}$	125	0	$0.207 \pm 0.022^{+0.073}_{-0.031}$	0.0
$Q^2 = 150.0\ (140.0-185.0)\ \mathrm{GeV}^2$				
$2.5(2.0-3.2)10^{-3}$	159	0	$1.275 \pm 0.130^{+0.051}_{-0.037}$	7.1
$4.0(3.2-5.0)10^{-3}$	376	8	$1.013 \pm 0.070^{+0.026}_{-0.020}$	2.1
$6.3(5.0-8.0)10^{-3}$	418	0	$0.991 \pm 0.063^{+0.028}_{-0.028}$	0.7
$1.0(0.8-1.3)10^{-2}$	382	0	$0.835 \pm 0.056^{+0.024}_{-0.016}$	0.2
$1.6(1.3-2.0)10^{-2}$	316	0	$0.685 \pm 0.050^{+0.020}_{-0.013}$	0.1
$2.5(2.0-3.2)10^{-2}$	314	0	$0.719 \pm 0.054^{+0.036}_{-0.027}$	0.0
$4.0(3.2-5.0)10^{-2}$	297	0	$0.522 \pm 0.039^{+0.012}_{-0.018}$	0.0
$0.8(0.5-1.3)10^{-1}$	573	0	$0.420 \pm 0.022^{+0.017}_{-0.005}$	0.0
$2.0(1.3-3.2)10^{-1}$	204	0	$0.288 \pm 0.026^{+0.033}_{-0.045}$	0.0
$Q^2 = 200.0\ (185.0-240.0)\ \mathrm{GeV}^2$				
$4.0(3.2-5.0)10^{-3}$	186	0	$1.035 \pm 0.096^{+0.026}_{-0.021}$	4.2
$6.3(5.0-8.0)10^{-3}$	267	0	$1.041 \pm 0.084^{+0.027}_{-0.021}$	1.3
$1.0(0.8-1.3)10^{-2}$	258	0	$0.832 \pm 0.067^{+0.023}_{-0.024}$	0.4
$1.6(1.3-2.0)10^{-2}$	230	0	$0.720 \pm 0.062^{+0.021}_{-0.014}$	0.1
$2.5(2.0-3.2)10^{-2}$	189	0	$0.631 \pm 0.060^{+0.032}_{-0.024}$	0.0
$4.0(3.2-5.0)10^{-2}$	194	0	$0.541 \pm 0.050^{+0.013}_{-0.018}$	0.0
$0.8(0.5-1.3)10^{-1}$	372	0	$0.410 \pm 0.027^{+0.016}_{-0.005}$	0.0
$2.0(1.3-3.2)10^{-1}$	178	0	$0.271 \pm 0.025^{+0.012}_{-0.011}$	0.0

Table 1 (continued): *The measured F_2 values.*

$x(range)$	N_{ev}	N_{bg}	$F_2 \pm stat^{+sys}_{-sys}$	$\delta_L\%$
$Q^2 = 250.0\ (240.0 - 310.0)\ \mathrm{GeV}^2$				
$4.0(3.2 - 5.0)10^{-3}$	67	0	$1.353 \pm 0.219^{+0.054}_{-0.040}$	7.2
$6.3(5.0 - 8.0)10^{-3}$	184	0	$1.176 \pm 0.116^{+0.030}_{-0.024}$	2.1
$1.0(0.8 - 1.3)10^{-2}$	200	0	$0.916 \pm 0.085^{+0.026}_{-0.026}$	0.6
$1.6(1.3 - 2.0)10^{-2}$	147	0	$0.699 \pm 0.074^{+0.020}_{-0.013}$	0.2
$2.5(2.0 - 3.2)10^{-2}$	127	0	$0.544 \pm 0.061^{+0.016}_{-0.010}$	0.1
$4.0(3.2 - 5.0)10^{-2}$	148	0	$0.583 \pm 0.063^{+0.029}_{-0.022}$	0.0
$0.8(0.5 - 1.3)10^{-1}$	275	0	$0.435 \pm 0.034^{+0.010}_{-0.015}$	0.0
$2.0(1.3 - 3.2)10^{-1}$	148	0	$0.267 \pm 0.027^{+0.011}_{-0.011}$	0.0
$Q^2 = 350.0\ (310.0 - 410.0)\ \mathrm{GeV}^2$				
$6.3(5.0 - 8.0)10^{-3}$	129	0	$1.107 \pm 0.127^{+0.044}_{-0.032}$	4.8
$1.0(0.8 - 1.3)10^{-2}$	144	0	$0.814 \pm 0.086^{+0.021}_{-0.016}$	1.3
$1.6(1.3 - 2.0)10^{-2}$	120	0	$0.661 \pm 0.076^{+0.019}_{-0.019}$	0.4
$2.5(2.0 - 3.2)10^{-2}$	95	0	$0.446 \pm 0.055^{+0.013}_{-0.009}$	0.1
$4.0(3.2 - 5.0)10^{-2}$	103	0	$0.672 \pm 0.089^{+0.034}_{-0.025}$	0.0
$0.8(0.5 - 1.3)10^{-1}$	199	0	$0.414 \pm 0.037^{+0.010}_{-0.014}$	0.0
$2.0(1.3 - 3.2)10^{-1}$	130	0	$0.262 \pm 0.029^{+0.011}_{-0.003}$	0.0
$Q^2 = 450.0\ (410.0 - 530.0)\ \mathrm{GeV}^2$				
$6.3(5.0 - 8.0)10^{-3}$	51	0	$1.722 \pm 0.348^{+0.082}_{-0.066}$	8.7
$1.0(0.8 - 1.3)10^{-2}$	89	0	$0.929 \pm 0.128^{+0.033}_{-0.030}$	2.4
$1.6(1.3 - 2.0)10^{-2}$	84	0	$0.864 \pm 0.125^{+0.032}_{-0.033}$	0.7
$2.5(2.0 - 3.2)10^{-2}$	89	0	$0.688 \pm 0.095^{+0.026}_{-0.026}$	0.2
$4.0(3.2 - 5.0)10^{-2}$	52	0	$0.435 \pm 0.075^{+0.017}_{-0.014}$	0.1
$0.8(0.5 - 1.3)10^{-1}$	148	0	$0.455 \pm 0.048^{+0.026}_{-0.021}$	0.0
$2.0(1.3 - 3.2)10^{-1}$	115	0	$0.348 \pm 0.043^{+0.016}_{-0.010}$	0.0
$Q^2 = 650.0\ (530.0 - 710.0)\ \mathrm{GeV}^2$				
$1.0(0.8 - 1.3)10^{-2}$	76	0	$1.067 \pm 0.163^{+0.051}_{-0.041}$	5.7
$1.6(1.3 - 2.0)10^{-2}$	71	0	$0.897 \pm 0.142^{+0.032}_{-0.029}$	1.6
$2.5(2.0 - 3.2)10^{-2}$	78	0	$0.728 \pm 0.109^{+0.027}_{-0.028}$	0.5
$4.0(3.2 - 5.0)10^{-2}$	43	10	$0.471 \pm 0.102^{+0.018}_{-0.018}$	0.1
$0.8(0.5 - 1.3)10^{-1}$	104	0	$0.445 \pm 0.056^{+0.025}_{-0.020}$	0.0
$2.0(1.3 - 3.2)10^{-1}$	96	0	$0.344 \pm 0.046^{+0.012}_{-0.014}$	0.0
$Q^2 = 800.0\ (710.0 - 900.0)\ \mathrm{GeV}^2$				
$1.0(0.8 - 1.3)10^{-2}$	22	0	$0.890 \pm 0.241^{+0.042}_{-0.034}$	9.3
$1.6(1.3 - 2.0)10^{-2}$	40	0	$0.819 \pm 0.169^{+0.029}_{-0.026}$	2.6
$2.5(2.0 - 3.2)10^{-2}$	48	0	$0.657 \pm 0.122^{+0.023}_{-0.021}$	0.8
$4.0(3.2 - 5.0)10^{-2}$	32	0	$0.512 \pm 0.115^{+0.019}_{-0.019}$	0.2
$0.8(0.5 - 1.3)10^{-1}$	54	0	$0.293 \pm 0.048^{+0.011}_{-0.009}$	0.0
$2.0(1.3 - 3.2)10^{-1}$	45	0	$0.227 \pm 0.041^{+0.008}_{-0.010}$	0.0

Table 2: *The measured F_2 and F_2^{em} values for $Q^2 > 1000$ GeV^2 (see text). The values of x and Q^2 at which F_2 and F_2^{em} are determined are shown outside the brackets, while the bin boundaries are shown inside the brackets. The number of events in each bin as well as the estimated number of background events are given. The corrections for F_L, δ_L (see eq. 18), are also given.*

$x(range)$	N_{ev}	N_{bg}	F_2	$F_2^{em} \pm stat^{+sys}_{-sys}$	$\delta_L\%$
$Q^2 = 1200.0$ $(900.0 - 1300.0)$ GeV^2					
$1.6(1.3 - 2.0)10^{-2}$	34	0	0.645	$0.634 \pm 0.135^{+0.030}_{-0.024}$	6.8
$2.5(2.0 - 3.2)10^{-2}$	41	0	0.652	$0.641 \pm 0.128^{+0.023}_{-0.021}$	1.9
$4.0(3.2 - 5.0)10^{-2}$	32	0	0.586	$0.577 \pm 0.132^{+0.021}_{-0.019}$	0.5
$0.8(0.5 - 1.3)10^{-1}$	54	0	0.321	$0.316 \pm 0.052^{+0.012}_{-0.010}$	0.1
$2.0(1.3 - 3.2)10^{-1}$	48	0	0.308	$0.304 \pm 0.057^{+0.017}_{-0.014}$	0.0
$5.1(3.2 - 8.0)10^{-1}$	11	0	0.056	$0.055 \pm 0.020^{+0.003}_{-0.002}$	0.0
$Q^2 = 1500.0$ $(1300.0 - 1800.0)$ GeV^2					
$2.5(2.0 - 5.0)10^{-2}$	52	0	0.614	$0.601 \pm 0.105^{+0.028}_{-0.023}$	3.2
$0.8(0.5 - 1.3)10^{-1}$	46	0	0.605	$0.593 \pm 0.119^{+0.022}_{-0.022}$	0.1
$2.0(1.3 - 3.2)10^{-1}$	29	0	0.216	$0.212 \pm 0.048^{+0.012}_{-0.010}$	0.0
$Q^2 = 2000.0$ $(1800.0 - 2500.0)$ GeV^2					
$4.0(2.0 - 5.0)10^{-2}$	28	0	0.704	$0.682 \pm 0.169^{+0.024}_{-0.022}$	1.7
$0.8(0.5 - 1.3)10^{-1}$	19	0	0.362	$0.351 \pm 0.099^{+0.013}_{-0.013}$	0.2
$2.0(1.3 - 3.2)10^{-1}$	25	0	0.412	$0.401 \pm 0.110^{+0.015}_{-0.013}$	0.0
$Q^2 = 3000.0$ $(2500.0 - 3500.0)$ GeV^2					
$0.8(0.2 - 1.3)10^{-1}$	15	0	0.238	$0.227 \pm 0.067^{+0.008}_{-0.007}$	0.5
$2.0(1.3 - 8.0)10^{-1}$	26	0	0.479	$0.458 \pm 0.127^{+0.017}_{-0.014}$	0.0
$Q^2 = 5000.0$ $(3500.0 - 15000.0)$ GeV^2					
$0.8(0.2 - 1.3)10^{-1}$	12	0	0.613	$0.558 \pm 0.209^{+0.026}_{-0.022}$	1.7
$2.0(1.3 - 8.0)10^{-1}$	17	0	0.211	$0.194 \pm 0.056^{+0.007}_{-0.007}$	0.1

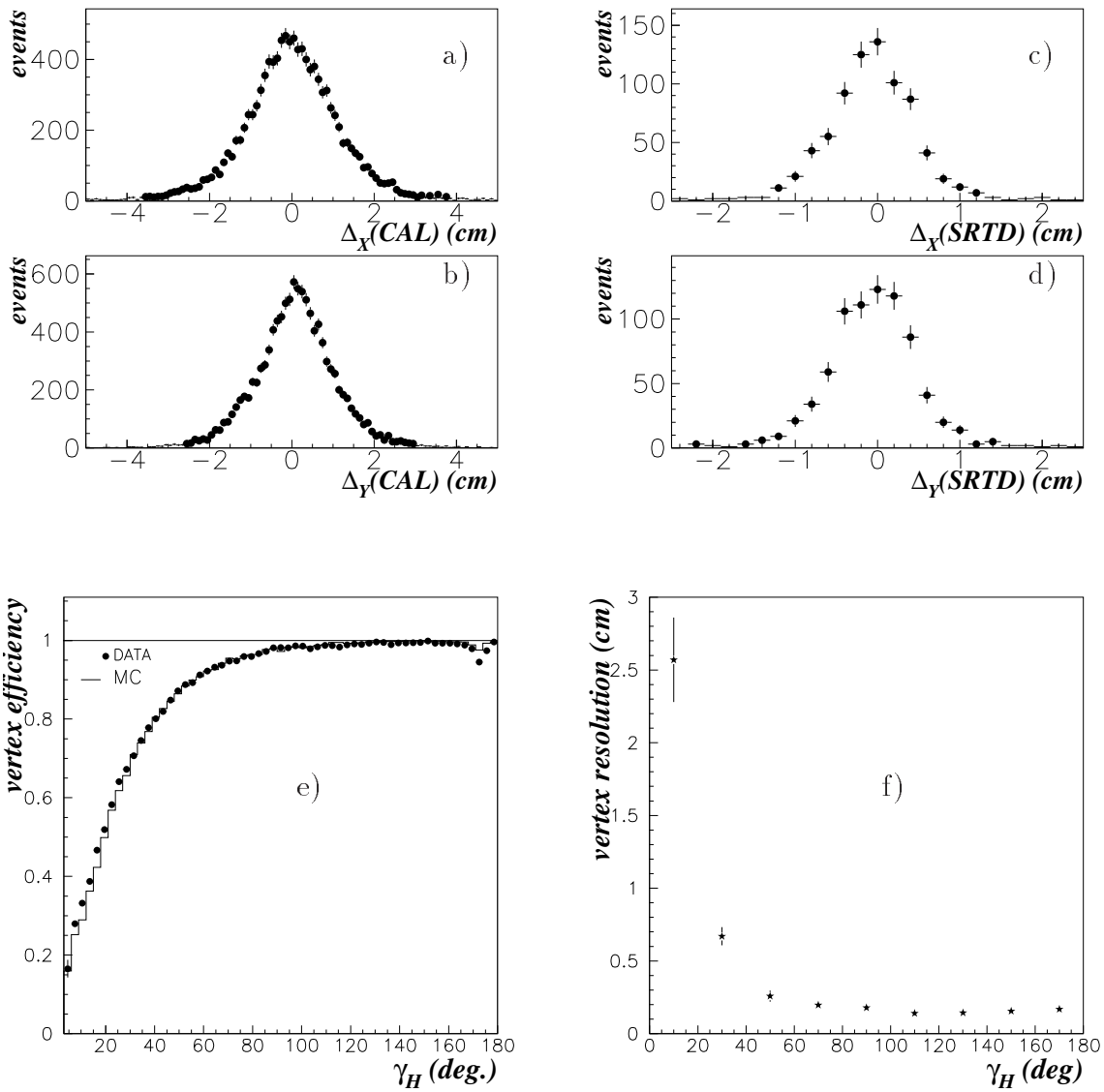

Figure 1: *Distance (in cm) between track and RCAL position a) in X, b) and Y. Distance (in cm) between track and SRTD position c) in X, d) and Y. e) Vertex reconstruction efficiency as a function of γ_H (points: data; histogram: MC). f) Vertex resolution along the beam (in cm) as a function of γ_H.*

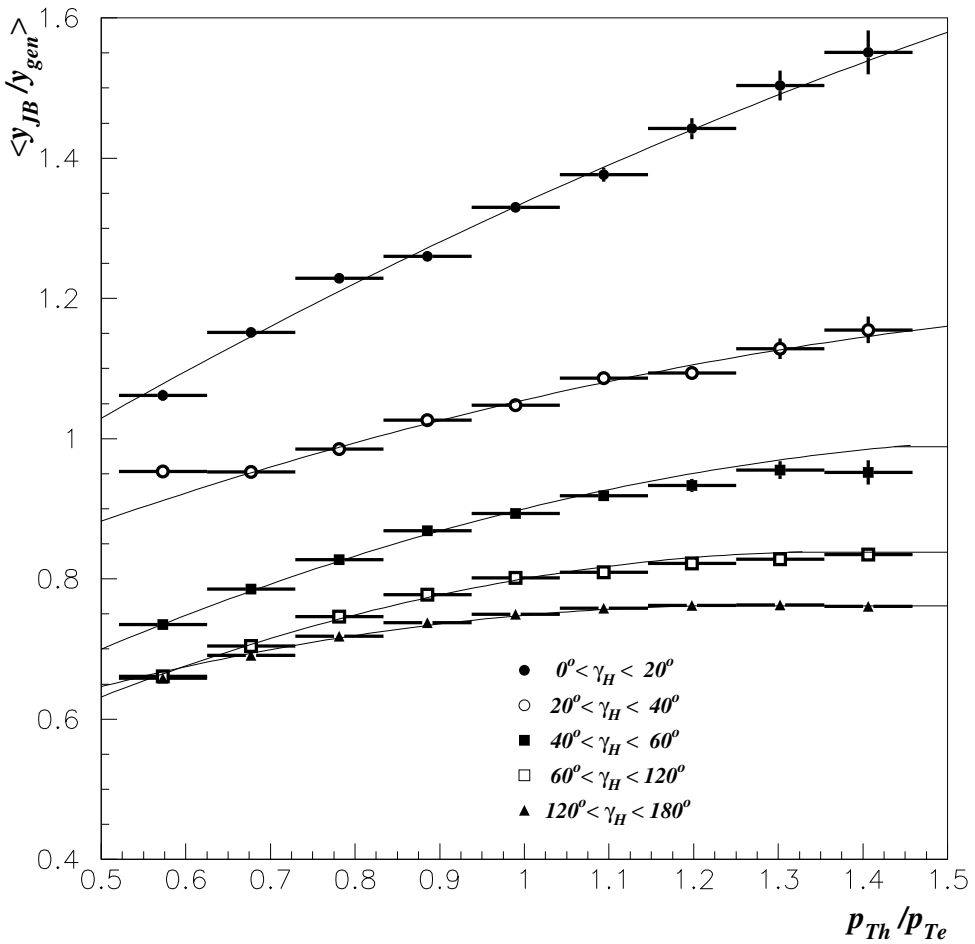

Figure 2: *The ratio* $\frac{y_{JB}}{y_{gen}}$ *averaged over* p_{Th} *as a function of* $\frac{p_{Th}}{p_{Te}}$ *for several ranges of* γ_H*. The curves show the correction function* $\mathcal{C}(\frac{p_{Th}}{p_{Te}}, p_{Th}, \gamma_H)$*, averaged over* p_{Th} *as a function of* $\frac{p_{Th}}{p_{Te}}$ *for several ranges in* γ_H*.*

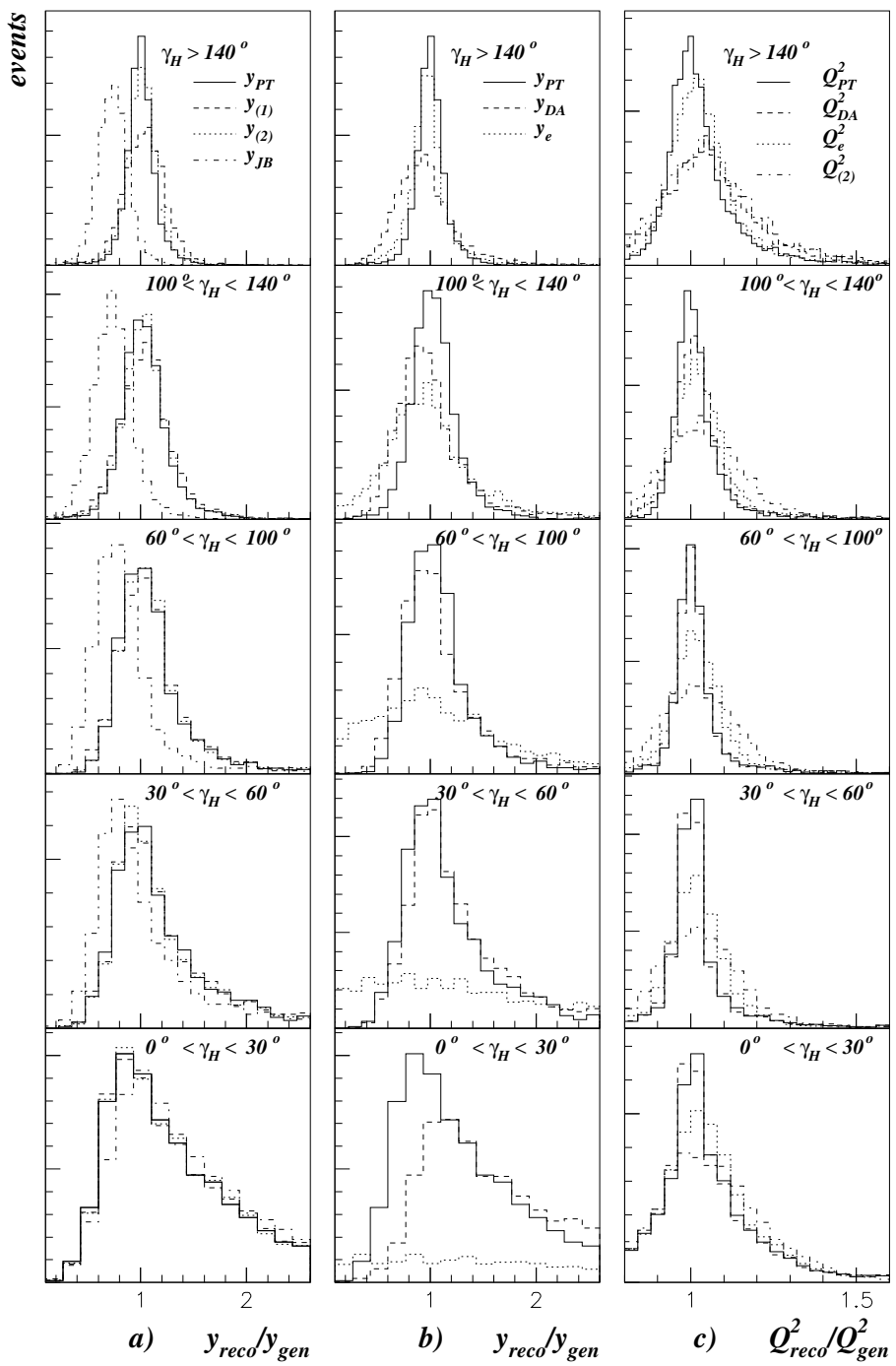

Figure 3: *a) The distributions of* $\frac{y_{JB}}{y_{gen}}$ *(dashed-dotted),* $\frac{y_{(1)}}{y_{gen}}$ *(dashed),* $\frac{y_{(2)}}{y_{gen}}$ *(dotted) and* $\frac{y_{PT}}{y_{gen}}$ *(solid) for several ranges in* γ_H *as determined from the MC simulation. b) The distributions of* $\frac{y_e}{y_{gen}}$ *(dotted),* $\frac{y_{DA}}{y_{gen}}$ *(dashed) and* $\frac{y_{PT}}{y_{gen}}$ *(solid) for several ranges in* γ_H *as obtained from the MC simulation. c) The corresponding distributions of* $\frac{Q^2_{PT}}{Q^2_{gen}}$ *(solid),* $\frac{Q^2_{DA}}{Q^2_{gen}}$ *(dashed),* $\frac{Q^2_e}{Q^2_{gen}}$ *(dotted) and* $\frac{Q^2_{(2)}}{Q^2_{gen}}$ *(dashed-dotted).*

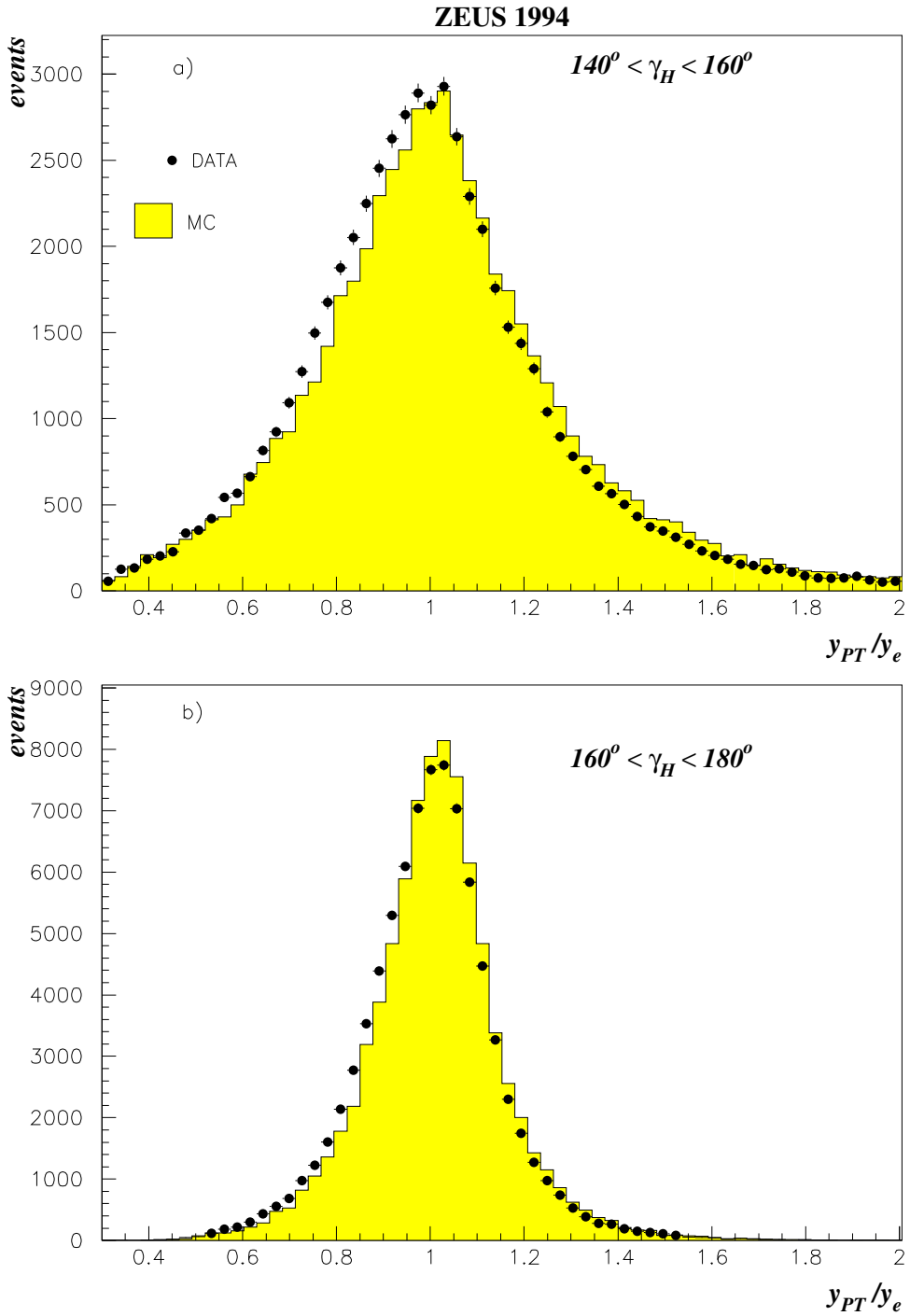

Figure 4: *The distributions of* $\frac{y_{PT}}{y_{gen}}$ *for a)* $140° < \gamma_H < 160°$ *and b)* $160° < \gamma_H < 180°$. *The points show the data and the shaded histograms show the results from the MC simulation.*

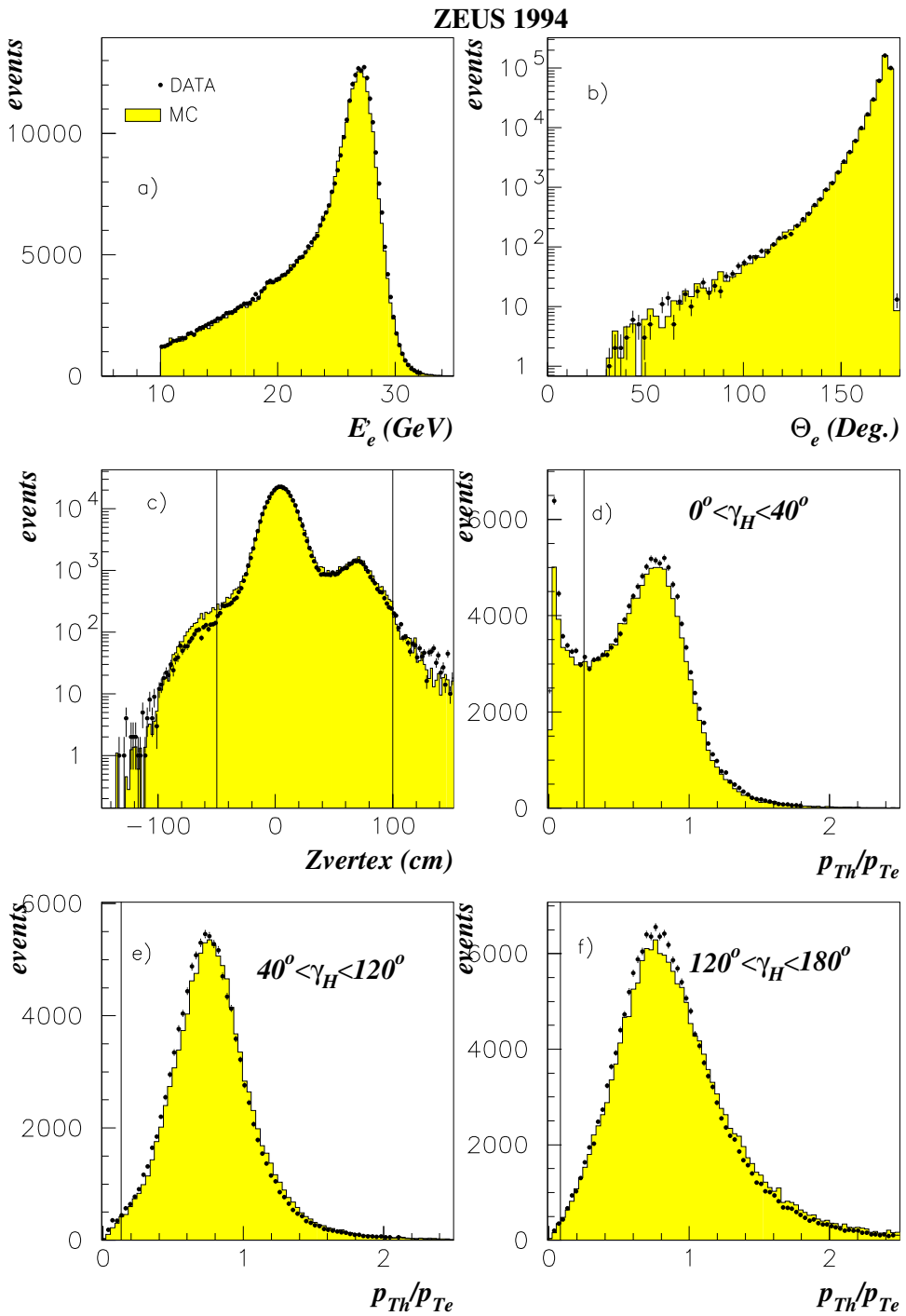

Figure 5: *Distributions of a) positron energy, b) positron angle, c) Z_{vertex}, d)–f) $\frac{p_{Th}}{p_{Te}}$ for different ranges of γ_H. The vertical lines in c)–f) indicate the positions of the cuts used in the analysis. For d)-f) the cut values are shown for the central value of γ_H in each bin (see text). The MC distributions are normalised to the integrated luminosity of the data.*

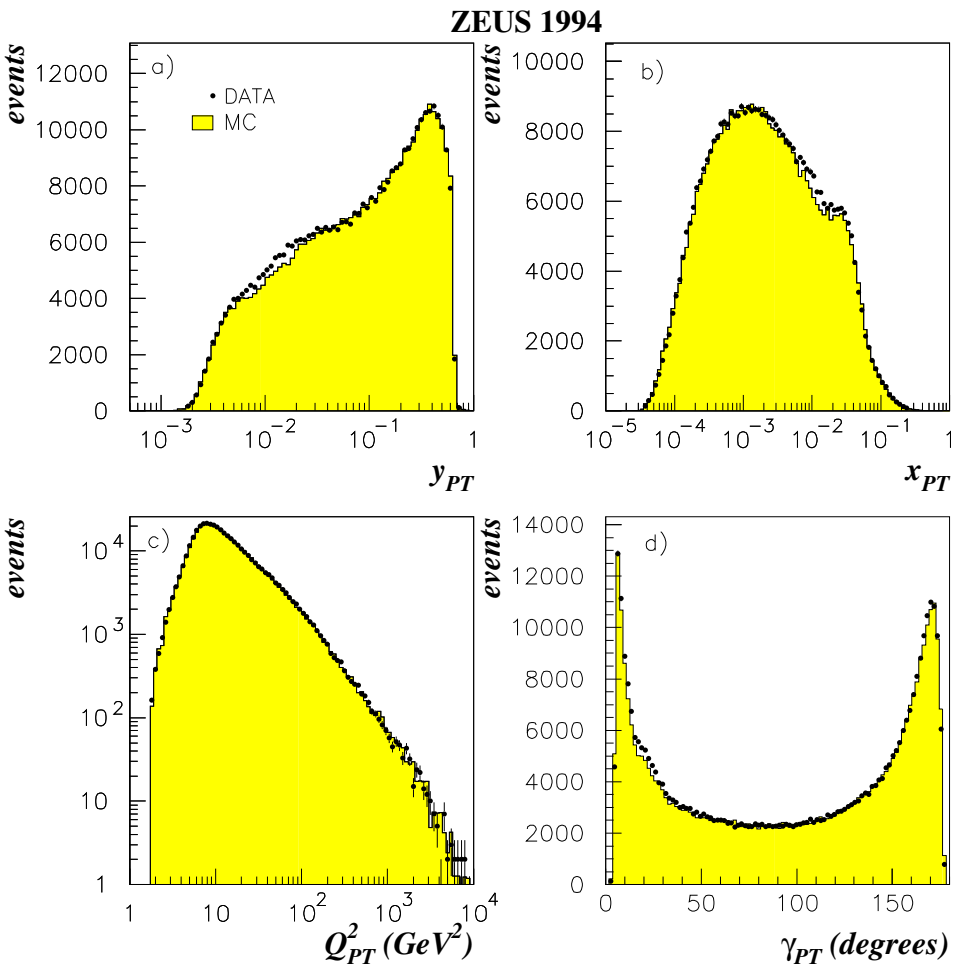

Figure 6: *The distributions of a) y_{PT}, b) x_{PT}, c) Q^2_{PT} and d) γ_{PT} for data (points) compared with the distributions obtained from the MC simulation (shaded histograms). The MC distributions are normalised to the integrated luminosity of the data.*

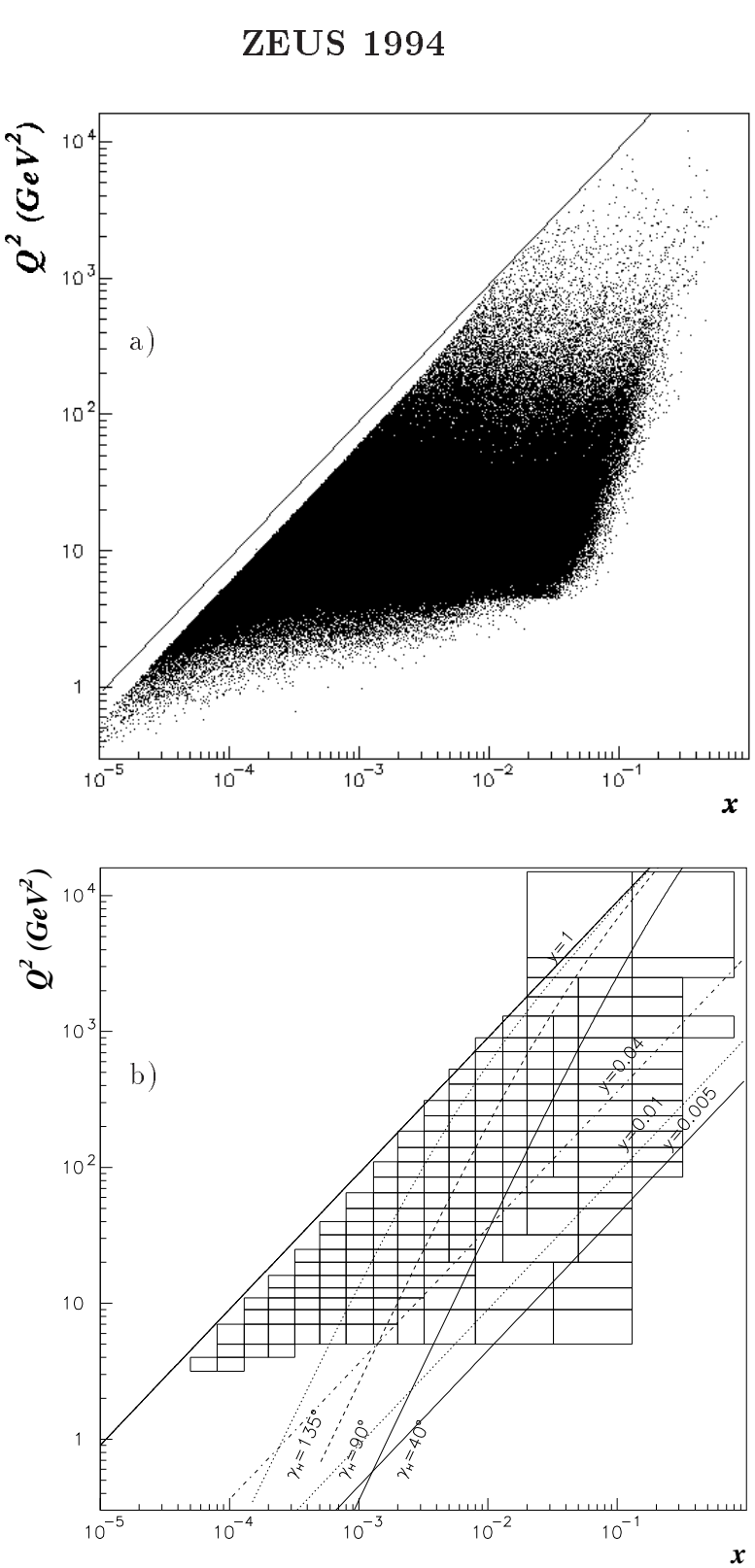

Figure 7: *a) The distribution of the events in the (x,Q^2) plane. b) The (x,Q^2)-bins used in the structure function determination. Also indicated are lines of constant y and of constant γ_H. The γ_H values for this figure are calculated directly from x and Q^2.*

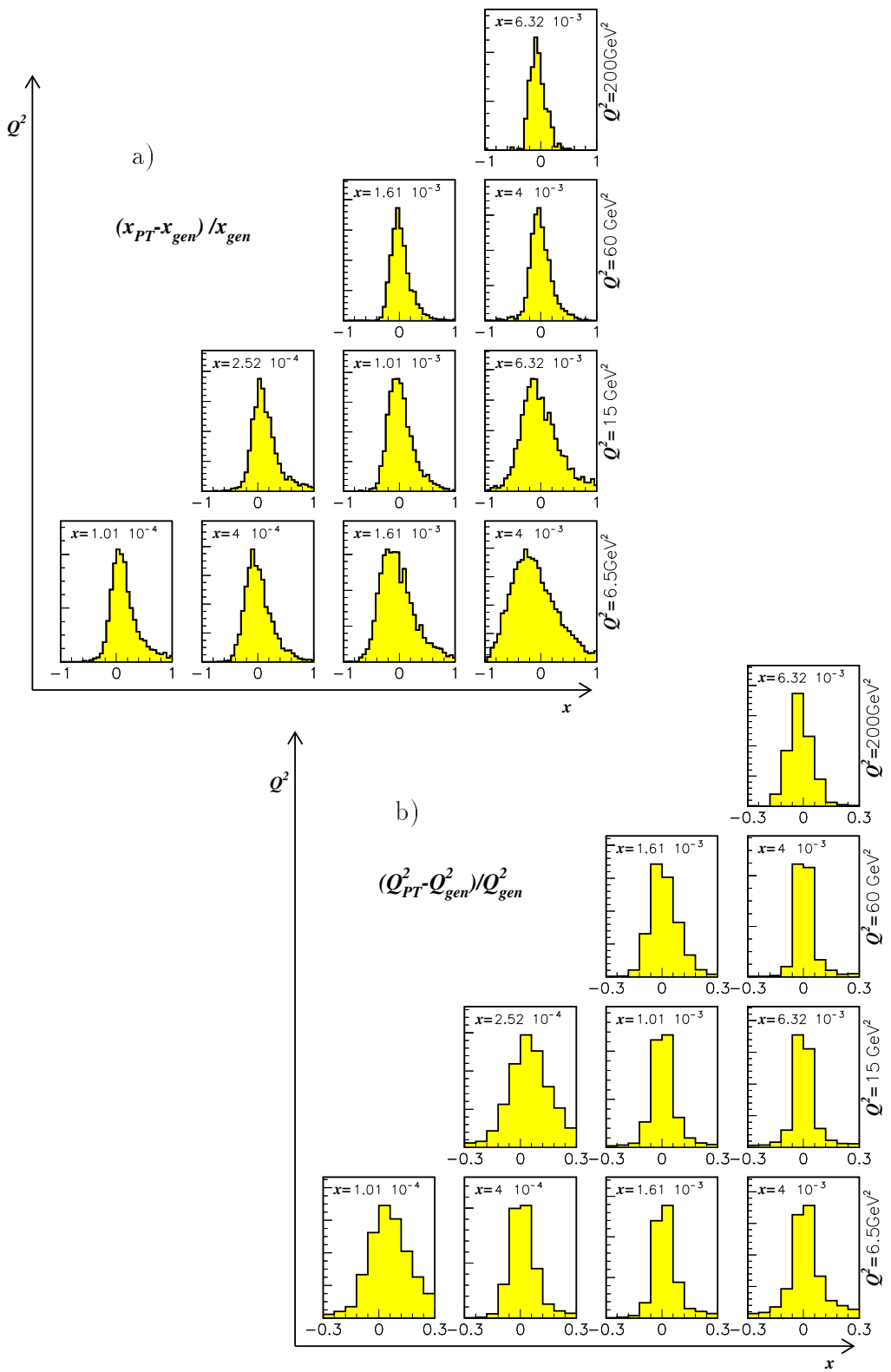

Figure 8: *a) The distributions of* $\frac{x_{PT}-x_{gen}}{x_{gen}}$ *for different* (x,Q^2) *bins, obtained by MC simulation. b) The distributions of* $\frac{Q^2_{PT}-Q^2_{gen}}{Q^2_{gen}}$ *for the same* (x,Q^2) *bins.*

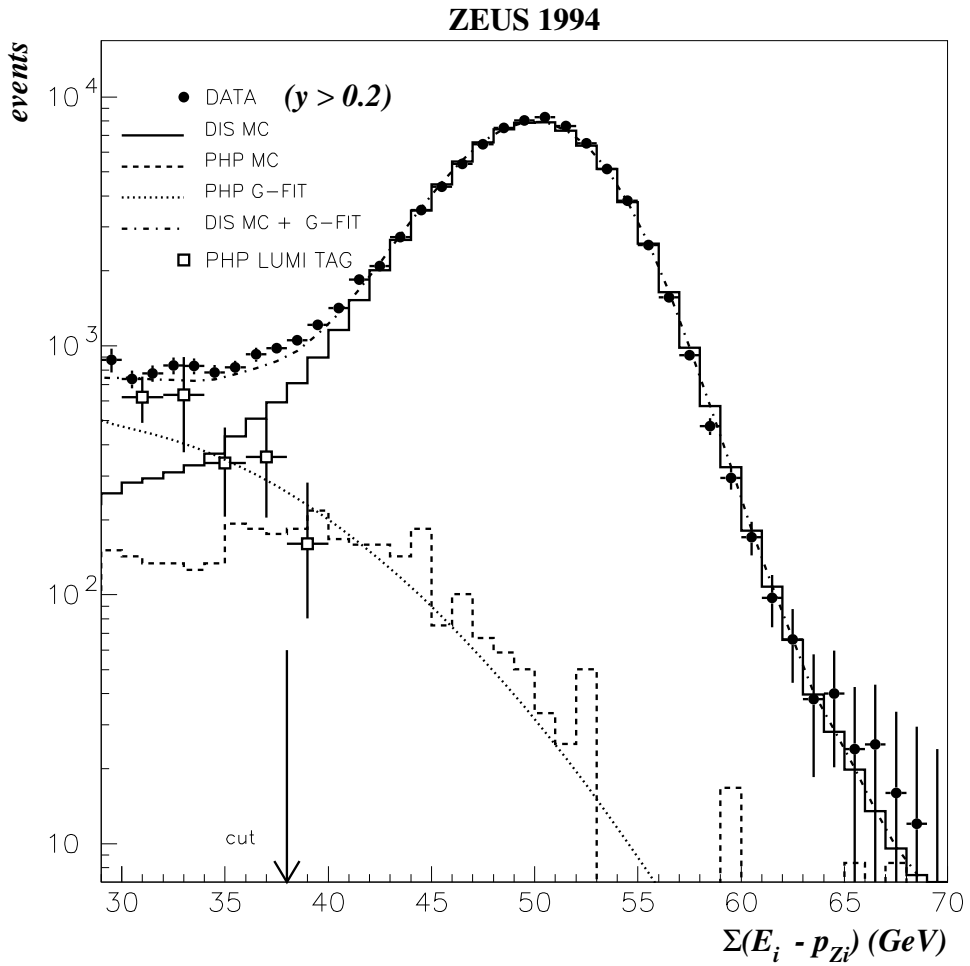

Figure 9: *The distribution of $\Sigma_i(E_i - p_{Zi})$ for data (solid dots), DIS MC simulation (solid histogram), photoproduction (PHP) MC simulation (dashed histogram) and LUMI tagged photoproduction data (open squares). The PHP distribution is valid for $\Sigma_i(E_i - p_{Zi}) > 38$ GeV. The result of the fit to the data, described in the text, is shown as the dashed-dotted curve and the photoproduction contribution to this fit is indicated by the dotted curve.*

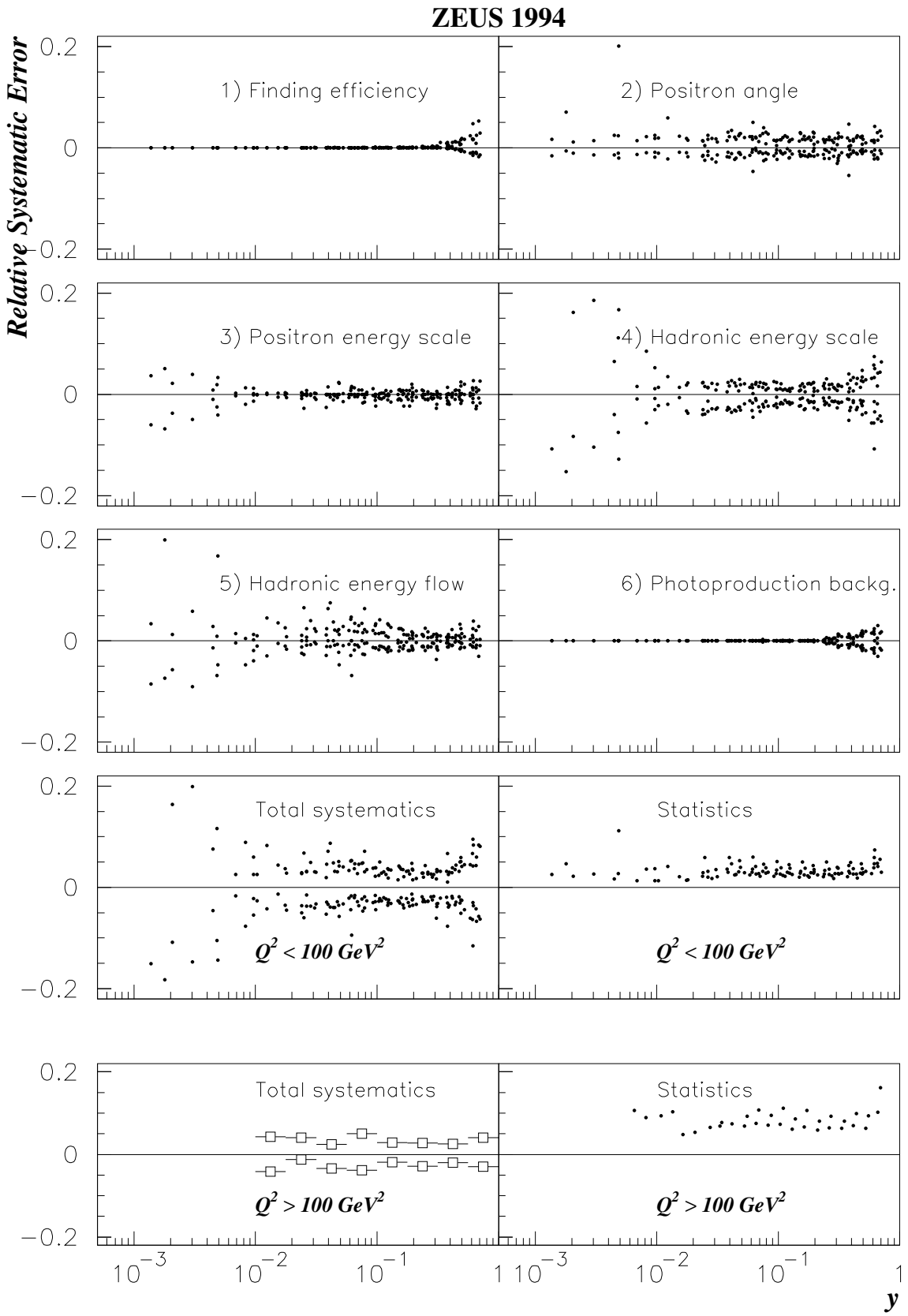

Figure 10: *Relative systematic errors as a function of y for different categories of systematic uncertainties for bins with* $Q^2 < 100$ GeV^2. *The total systematic and statistical errors are also given. The bottom two plots show total systematic and statistical errors for bins with with* $Q^2 > 100$ GeV^2. *In categories 4) and 5), and the total systematic error plot for* $Q^2 < 100$ *GeV*^{2}, *the four lowest y points are off-scale and are not shown.*

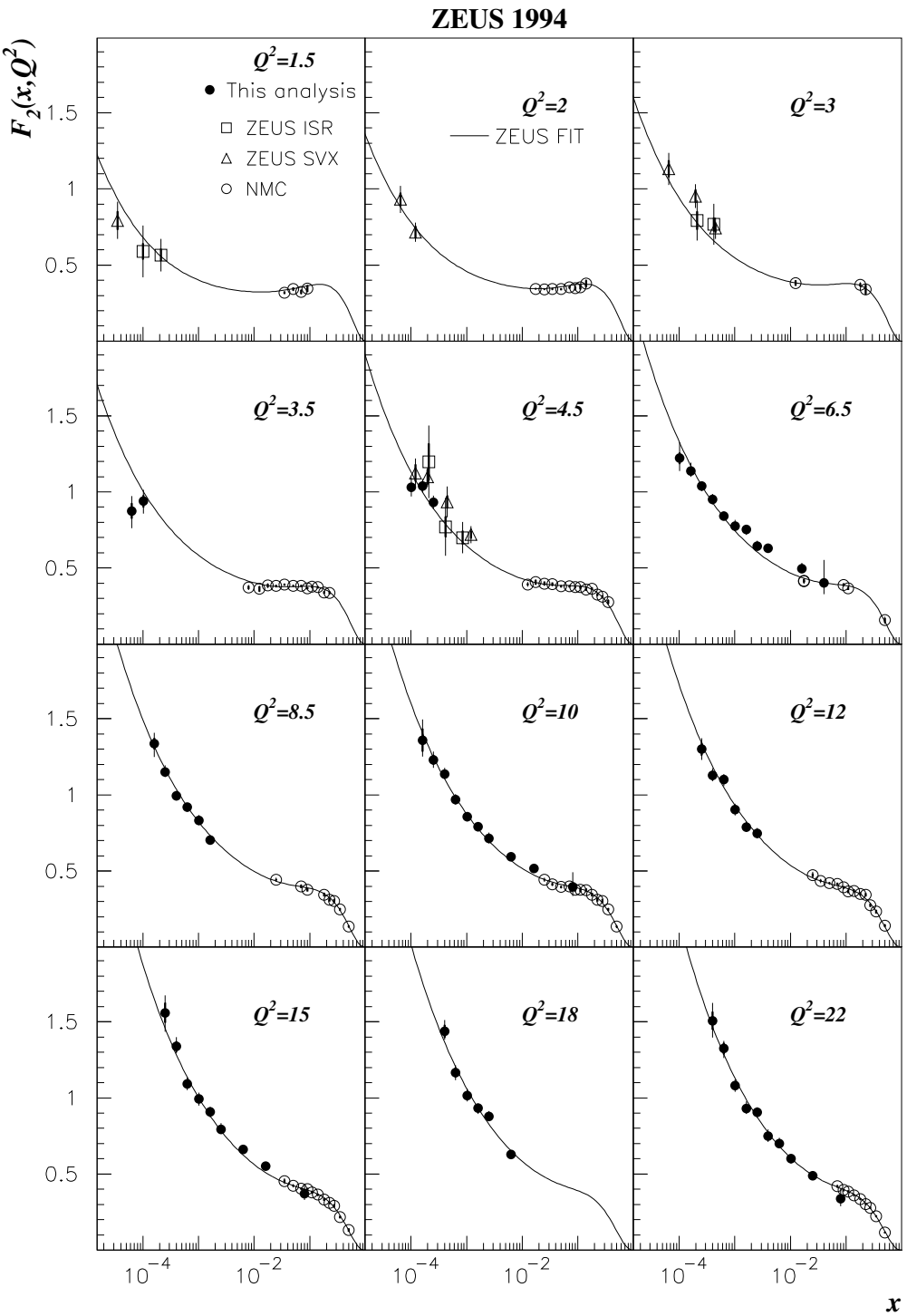

Figure 11a: *Structure function F_2 as a function of x for fixed values of Q^2 (1.5 GeV^2 < Q^2 < 22 GeV^2). The solid dots correspond to the data from this analysis. The "ISR" (open squares) and "SVX" (open triangles) data show the ZEUS results obtained previously. The inner thick error bars represent the statistical error, the full error bars correspond to the statistical and systematic errors added in quadrature. The results from NMC are also shown (open circles). The solid lines indicate the QCD NLO fit to the data used for the acceptance correction. The Q^2 values are indicated in units of* GeV^2.

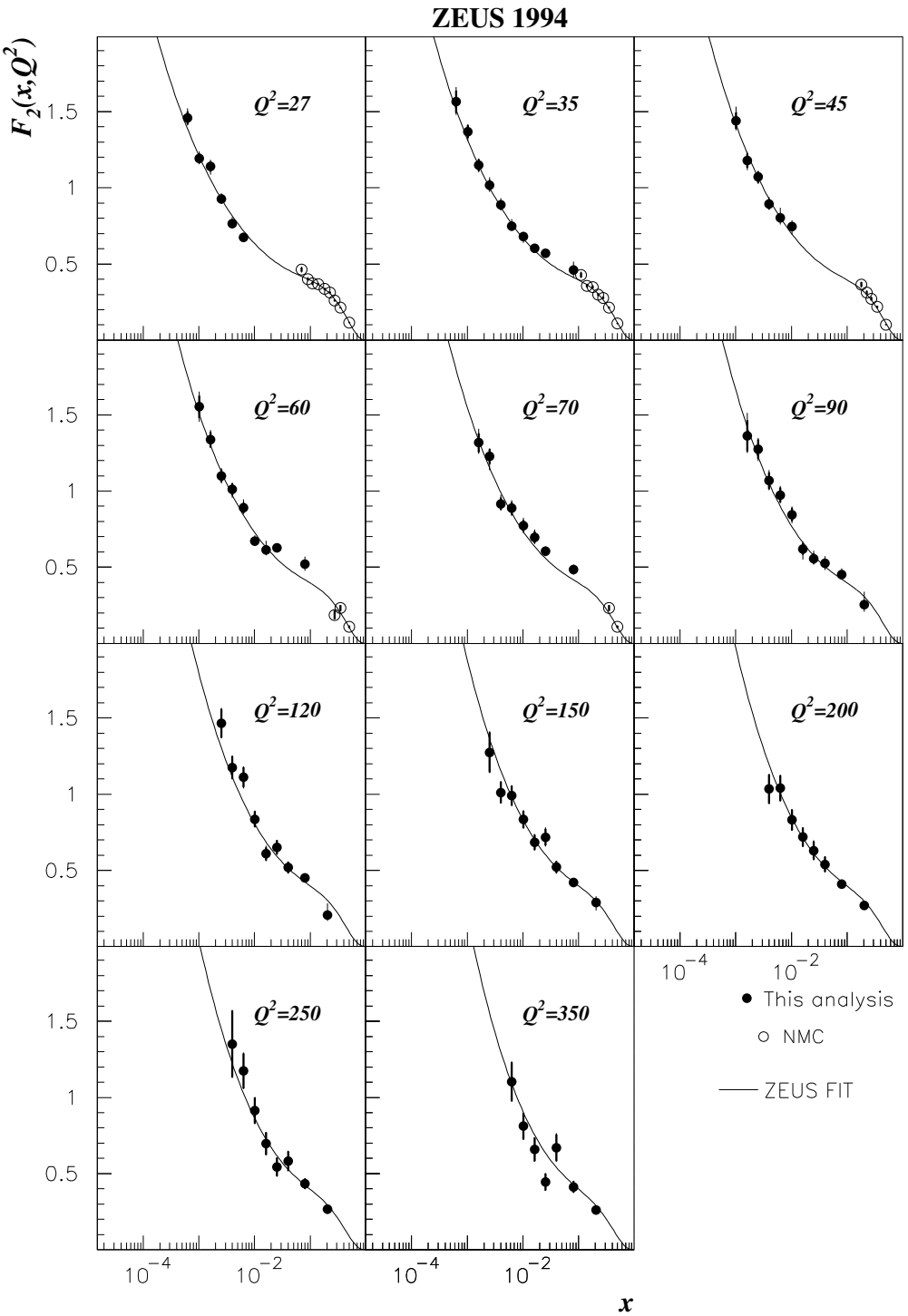

Figure 11b: *Structure function F_2 as a function of x for fixed values of Q^2* (27 GeV^2 $< Q^2 <$ 350 GeV^2). The Q^2 values are indicated in units of GeV^2.

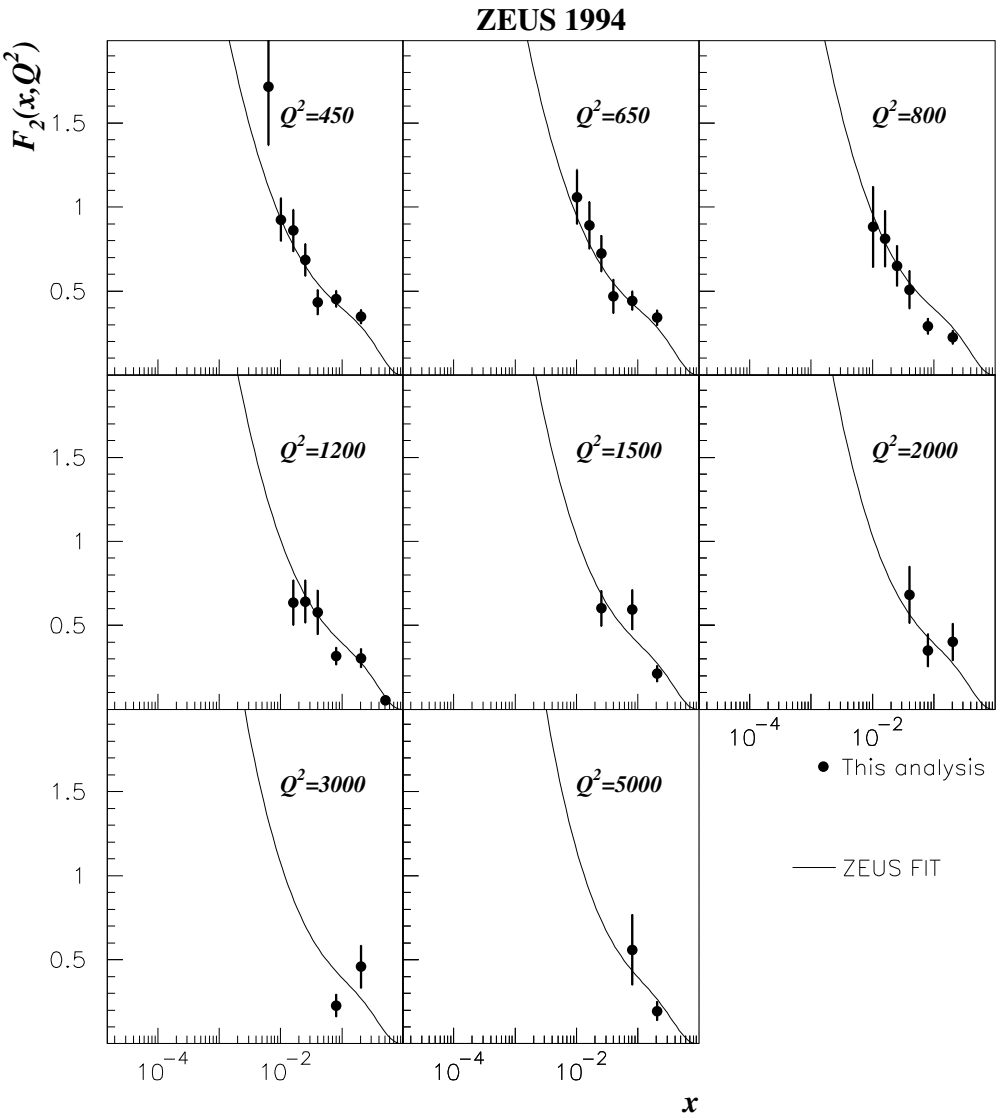

Figure 11c: *Structure function F_2 (F_2^{em} for $Q^2 > 1000$ GeV^2) as a function of x for fixed values of Q^2 (450 GeV^2 $< Q^2 <$ 5000 GeV^2).* The Q^2 values are indicated in units of GeV^2.

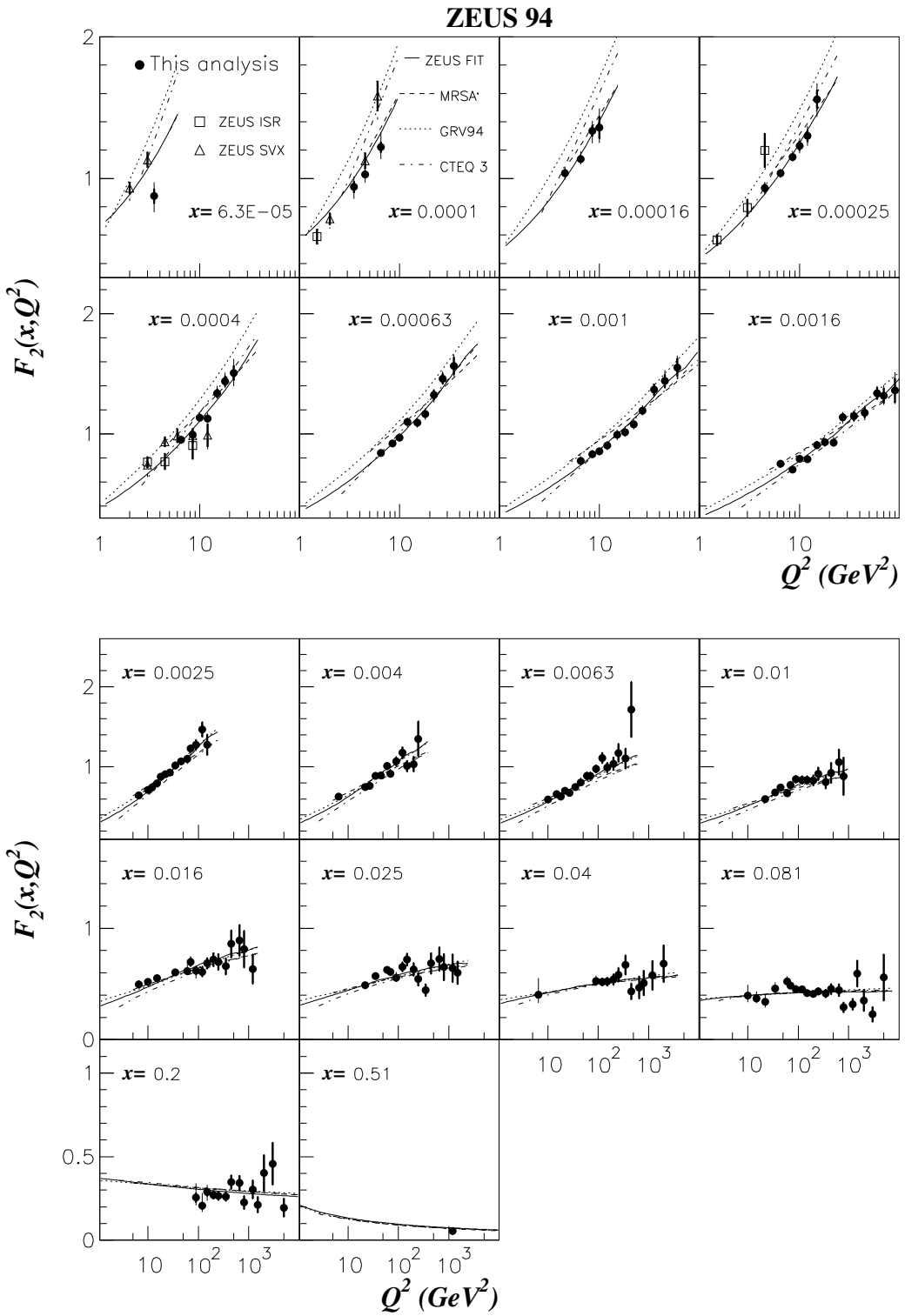

Figure 12: *Structure function F_2^{em} as a function of Q^2 for fixed values of x. The data from this analysis correspond to the solid dots. The "ISR" (open squares) and "SVX" (open triangles) data show the ZEUS results obtained previously. The solid line indicates the QCD NLO fit to the data used for acceptance correction. Also indicated are the MRSA′, GRV94 and CTEQ3 parameterisations.*

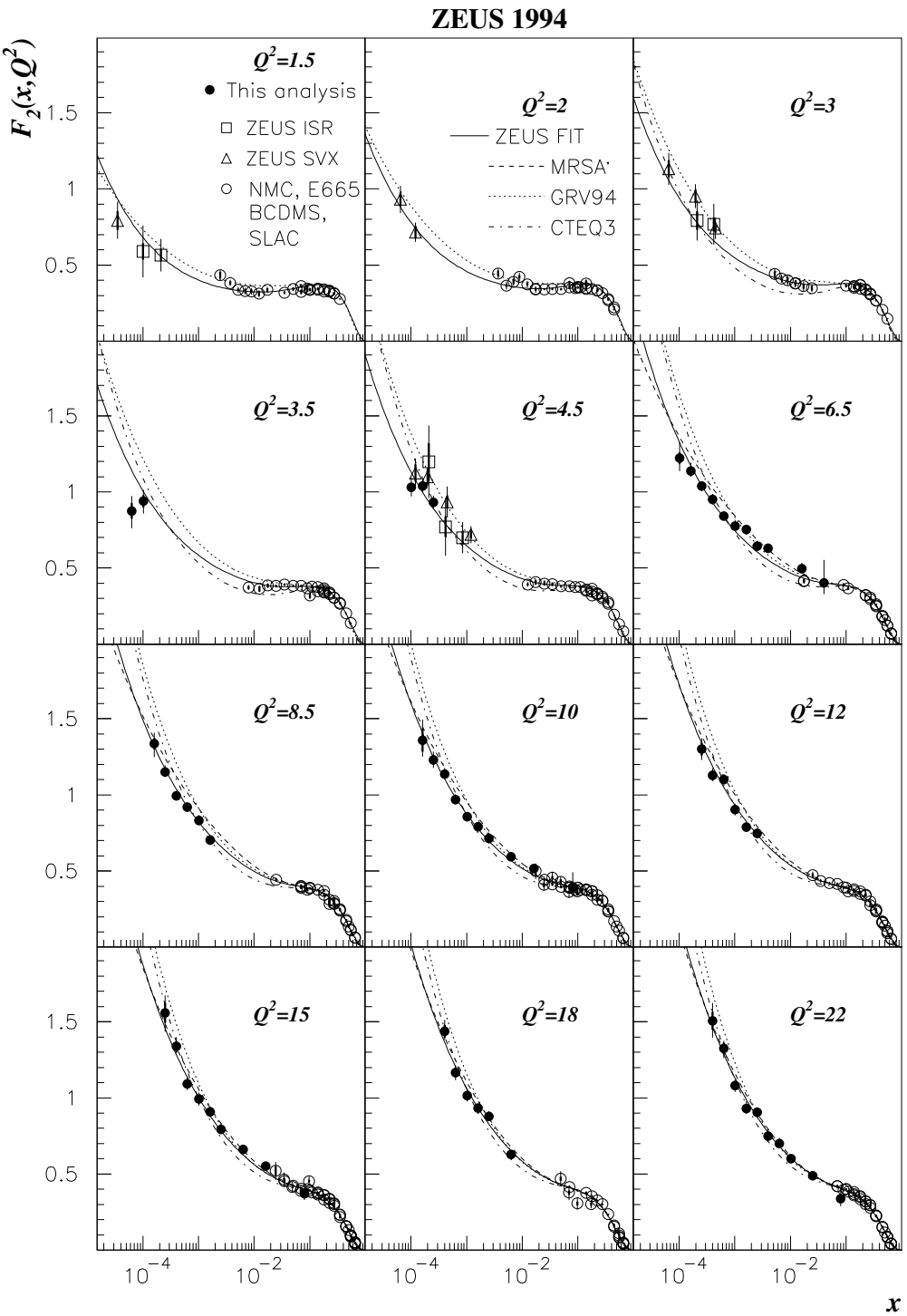

Figure 13a: *Structure function F_2 as a function of x for fixed values of Q^2. The solid dots correspond to the data from this analysis. The "ISR" (open squares) and "SVX" (open triangles) data show the ZEUS results obtained previously. The inner thick error bars represent the statistical error, the full error bars correspond to the statistical and systematic errors added in quadrature. The results from NMC, E665, BCDMS and SLAC are also shown (open circles). The solid line indicates the QCD NLO fit to the data used for acceptance correction. Also indicated are the MRSA′, GRV94 and CTEQ3 parameterisations. The Q^2 values are given in* GeV^2.

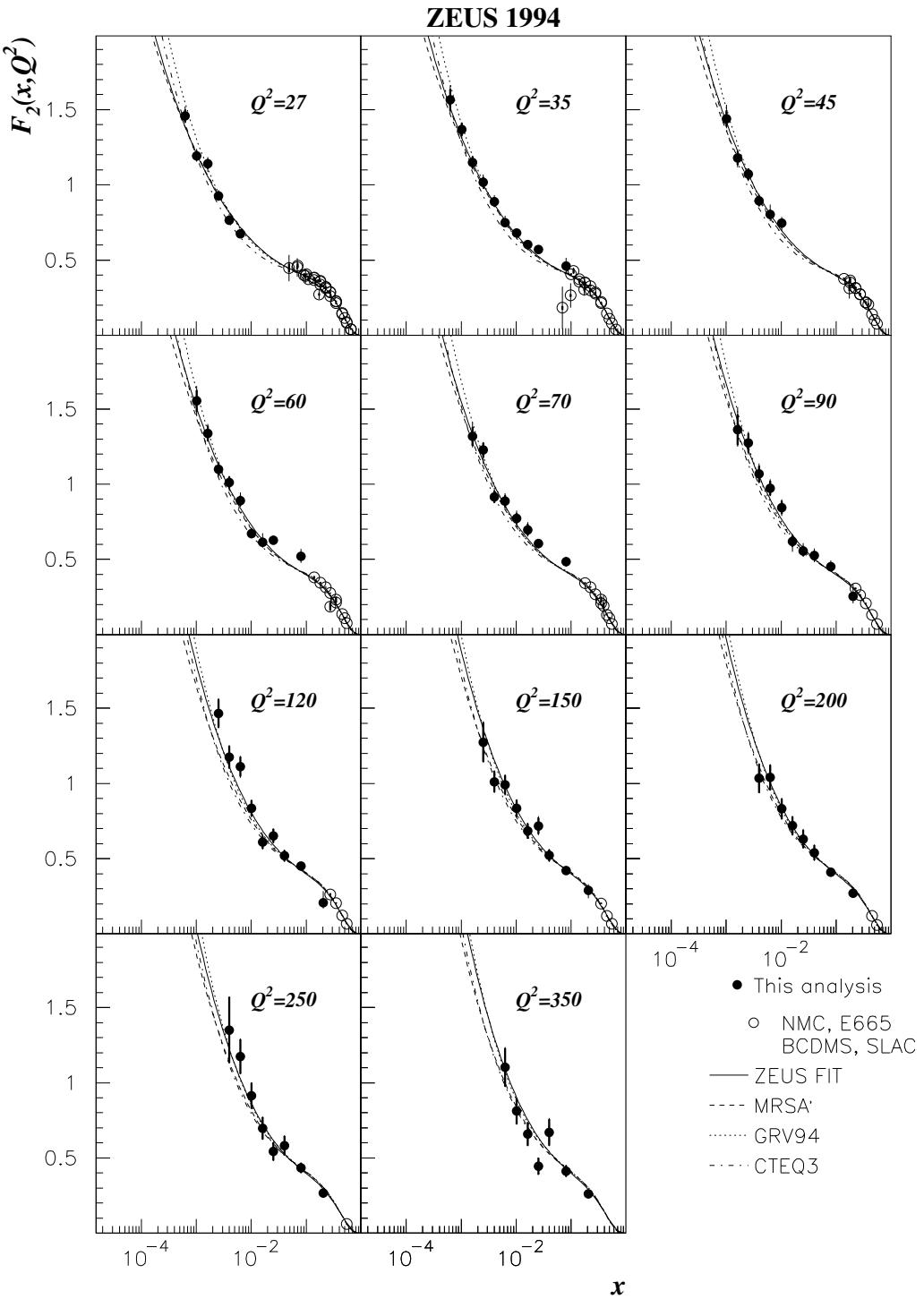

Figure 13b: *Structure function F_2 as a function of x for fixed values of Q^2. The solid line indicates the QCD NLO fit to the data used for acceptance correction. Also indicated are the MRSA′, GRV94 and CTEQ3 parameterisations. The Q^2 values are given in* GeV^2.

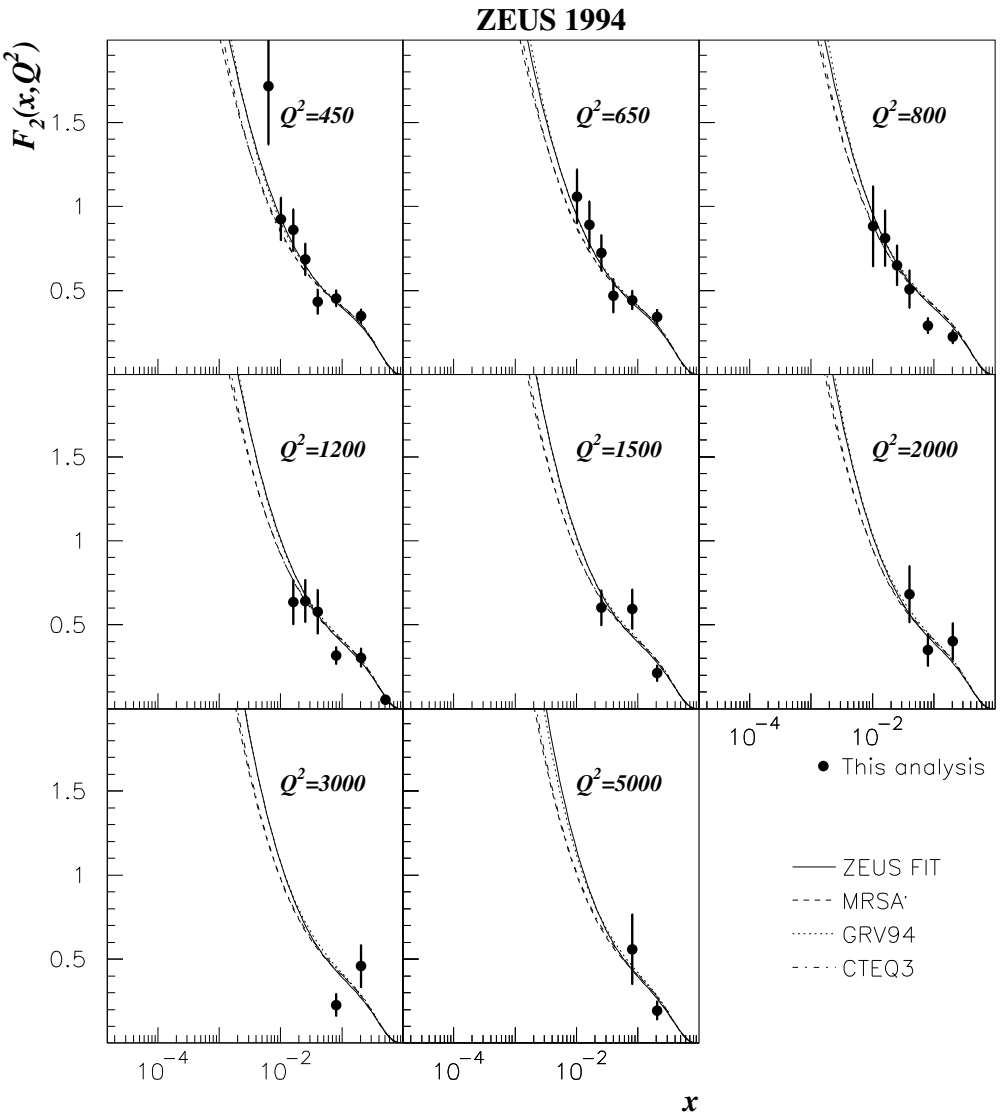

Figure 13c: *Structure function F_2 (F_2^{em} for $Q^2 > 1000$ GeV^2) as a function of x for fixed values of Q^2. The solid curves indicates the QCD NLO fit to the data used for acceptance correction. Also indicated are the MRSA', GRV94 and CTEQ3 parameterisations. The Q^2 values are given in* GeV^2.

A Systematic uncertainties and their correlations

In Sect. 7.1, the determination of the systematic uncertainties of the F_2 values was discussed. The resulting systematic errors are given in Tables 1 and 2. Bin to bin correlations exist for the systematic errors. Given the small statistical and systematic uncertainties of the present measurement these correlations should be taken into account when performing fits.

A.1 F_2 values resulting from systematic checks

Tables A1a and A1b give the F_2 values obtained for each of the 29 different checks of systematic uncertainties described in Sect. 7.1.[6] As noted above, the systematic uncertainties for the F_2 measurements at $Q^2 > 100$ GeV^2 and $y = \frac{Q^2}{xs} > 0.01$ are small compared to the statistical errors. Therefore, these F_2 values are given only for the data with $Q^2 < 100$ GeV^2 or $y < 0.01$.

In the calculation of the total systematic uncertainty given in Tables 1 and 2, the deviations from the central value for each check were added in quadrature, except for the two checks concerning diffractively produced events (n^o 23, 24) whose contributions were calculated from the maximum offset, positive or negative, produced by the checks of n^o 23 and 24.

Fits to the F_2 data, which take the systematic error correlations into account, may be performed in the following way. First the F_2 values with their statistical errors as given in Tables 1 and 2 are fitted. This yields the standard values of the fit parameters (a_i) and their statistical errors ($\sigma_i(stat)$). The fit is then repeated for each of the 29 sets of F_2 values listed in Tables A1a and A1b resulting in 29 different sets of fit parameters a_i^f, $f = 1 - 29$. An estimate of the systematic errors of the fit parameters may be obtained by adding in quadrature, for each fit parameter, the differences from the central parameter values, $\sigma_i(syst) = \sqrt{\sum_f (a_i^f - a_i)^2}$.

Note that the overall normalisation error of 2% (see Sect. 7.1) must be taken into account separately.

A.2 Compact parametrisation of uncertainty correlations

Although we recommend the use of Tables A1a and A1b, in determining the effect of correlated uncertainties in a fit to F_2, the large number of systematic checks involved may make this a cumbersome process. Therefore, a somewhat more compact representation of the correlated systematic uncertainties is provided below.

We have investigated the dependence on y and Q^2 of the relative deviations, $\Delta(F_2)/F_2$, of the F_2 values listed in Tables A1a and A1b from the central values of F_2. These deviations can be

[6] This Table and a short description of its recommended usage is available in electronic form from the ZEUS WWW page whose current address is http://zow00.desy.de:8000/. It can also be obtained by contacting the authors.

grouped in six different classes of systematic behaviour, one of which is a function of Q^2 only and the others are functions of y only.

$$
\begin{aligned}
A: \quad & \tfrac{\Delta(F_2)}{F_2}\,[\%] &&= a_A - b_A \cdot \log_{10} Q^2 \\
B: \quad & \tfrac{\Delta(F_2)}{F_2}\,[\%] &&= a_B / |\log_{10} y|^2 \\
C: \quad & \tfrac{\Delta(F_2)}{F_2}\,[\%] &&= a_C / |\log_{10} y|^2 - b_C \cdot |\log_{10} y|^7 \\
D: \quad & \tfrac{\Delta(F_2)}{F_2}\,[\%] &&= a_D / |\log_{10} y|^2 + b_D \cdot |\log_{10} y|^7 - c_D \\
E: \quad & \tfrac{\Delta(F_2)}{F_2}\,[\%] &&= a_E \cdot |\log_{10} y|^2 - b_E \cdot |\log_{10} y|^4 \\
F: \quad & \tfrac{\Delta(F_2)}{F_2}\,[\%] &&= -a_F + b_F \cdot |\log_{10} y|
\end{aligned}
$$

The deviations produced by the systematic checks fall into one of the classes listed above (positive class) or into a class (negative class) where the signs of the coefficients are reversed (these classes are denoted by, e.g. –A). The parameters are determined by fitting the deviations produced by each check separately to the appropriate functional form. For each class the parameters obtained from each fit are then added in quadrature.

The results for the six classes of systematic errors are given in Table A2 and their dependence on Q^2 and y are displayed graphically in Fig. A1.[7] Note that these functions only represent the systematic errors within the kinematic range of the present F_2 measurements.

These functional forms may be used for systematic studies to reproduce the offsets of the values of F_2 for $Q^2 < 100$ GeV^2 or $y < 0.01$ given in this paper. Outside this kinematic region, the systematic errors given in Table 1 can be treated as uncorrelated errors.

The systematic deviations of the F_2 values as described by the 6+6 classes determined can be added to the central values of F_2 to produce 12 sets of F_2 data. These 12 sets may be used, in the same way as described in Sect. A.1 for the 29 sets, to determine the effect of correlated uncertainties on fits to F_2.

These functions have been tested using the QCD NLO fit described in Sect. 7. The systematic uncertainties of the fit parameters are consistent with the more complete treatment described in Sect. A.1. It should be noted, however, that the simplification of the systematic correlations results in some loss of information, and that the use of the full treatment described in Sect. A.1 is recommended if the most reliable estimates of the effect of correlated uncertainties are required.

[7] A FORTRAN program of these functions is available through the ZEUS WWW home page whose current address is http://zow00.desy.de:8000/. It can also be obtained by contacting the authors.

x	Q^2 (GeV^2)	0: F_2 standard	1: Finding efficiency +	2: Finding efficiency -	3: BOX X 28cm	4: BOX Y 28cm	5: Wide gap	6: Narrow gap	7: R+0.2cm	8: R-0.2cm	9: Vertex efficiency -1%	10: Vertex efficiency low γ_H +3%	11: Vertex cut (-28,40)	12: Positron Energy scale +	13: Positron Energy scale -	14: Hadron scale +3%	15: Hadron scale -3%	16: Hadron scale +3%	17: Hadron scale F/B/RCAL +3/0/-3 %	18: Hadron scale F/B/RCAL -3/0/+3 %	19: Hadron scale F/B/RCAL 0/+3/0 %	20: Noise +	21: Noise -	22: MEPS	23: Diffractive [37] (take maximum 23,24)	24: Diffractive x 2	25: Relax $\frac{P_{rb}}{P_{re}}$ cut	26: 1 P_{rb} bin	27: More γ bins	28: PHP background x 1.5	29: PHP background x 0.5
6.3 $\times 10^{-5}$	3.5	0.875	0.917	0.862	0.866	0.875	0.884	0.861	0.875	0.875	0.870	0.875	0.871	0.882	0.861	0.923	0.805	0.917	0.817	0.856	0.883	0.864	0.887	0.870	0.896	0.887	0.876	0.880	0.864	0.854	0.896
1.0 $\times 10^{-4}$	3.5	0.939	0.949	0.937	0.980	0.889	0.954	0.929	0.939	0.939	0.946	0.939	0.939	0.952	0.928	0.973	0.905	0.954	0.910	0.935	0.947	0.923	0.943	0.936	0.946	0.946	0.938	0.935	0.945	0.926	0.952
1.0 $\times 10^{-4}$	4.5	1.030	1.046	1.023	1.032	1.034	1.036	1.019	1.030	1.030	1.027	1.030	1.031	1.055	1.011	1.069	0.998	1.056	1.006	1.019	1.030	1.024	1.038	1.028	1.036	1.034	1.028	1.016	1.031	1.010	1.050
1.6 $\times 10^{-4}$	4.5	1.038	1.042	1.037	1.056	1.015	1.046	1.024	1.038	1.038	1.041	1.038	1.060	1.044	1.037	1.034	1.034	1.028	1.046	1.032	1.047	1.029	1.049	1.036	1.029	1.041	1.036	1.034	1.031	1.028	1.047
2.5 $\times 10^{-4}$	4.5	0.932	0.933	0.932	0.930	0.918	0.952	0.928	0.932	0.932	0.935	0.932	0.951	0.935	0.934	0.929	0.924	0.914	0.937	0.922	0.933	0.924	0.931	0.940	0.939	0.935	0.930	0.943	0.918	0.931	0.934
1.0 $\times 10^{-4}$	6.5	1.221	1.257	1.204	1.220	1.227	1.235	1.208	1.221	1.222	1.221	1.221	1.246	1.254	1.201	1.282	1.173	1.266	1.179	1.213	1.237	1.214	1.226	1.215	1.212	1.229	1.223	1.222	1.216	1.199	1.243
1.6 $\times 10^{-4}$	6.5	1.138	1.151	1.135	1.135	1.133	1.158	1.125	1.138	1.138	1.139	1.138	1.157	1.148	1.137	1.164	1.114	1.158	1.125	1.130	1.145	1.133	1.147	1.138	1.135	1.136	1.138	1.149	1.142	1.128	1.147
2.5 $\times 10^{-4}$	6.5	1.038	1.042	1.038	1.031	1.042	1.046	1.022	1.038	1.038	1.035	1.038	1.044	1.030	1.032	1.045	1.032	1.032	1.043	1.030	1.046	1.028	1.045	1.046	1.033	1.035	1.039	1.037	1.037	1.032	1.044
4.0 $\times 10^{-4}$	6.5	0.951	0.951	0.951	0.954	0.963	0.962	0.939	0.951	0.951	0.953	0.951	0.962	0.941	0.951	0.961	0.948	0.946	0.960	0.941	0.964	0.941	0.959	0.953	0.957	0.958	0.951	0.959	0.933	0.951	0.951
6.3 $\times 10^{-4}$	6.5	0.841	0.841	0.841	0.837	0.847	0.857	0.834	0.841	0.841	0.841	0.841	0.851	0.835	0.843	0.842	0.839	0.832	0.848	0.838	0.845	0.837	0.843	0.844	0.852	0.848	0.842	0.830	0.848	0.841	0.841
1.0 $\times 10^{-3}$	6.5	0.776	0.776	0.776	0.779	0.786	0.786	0.770	0.776	0.776	0.779	0.776	0.787	0.783	0.776	0.777	0.777	0.766	0.782	0.779	0.772	0.752	0.793	0.797	0.783	0.782	0.782	0.766	0.780	0.776	0.776
1.6 $\times 10^{-3}$	6.5	0.753	0.753	0.753	0.745	0.755	0.760	0.740	0.753	0.753	0.755	0.753	0.762	0.750	0.752	0.747	0.752	0.752	0.757	0.755	0.746	0.729	0.764	0.767	0.755	0.760	0.756	0.750	0.747	0.753	0.753
2.5 $\times 10^{-3}$	6.5	0.645	0.645	0.645	0.634	0.652	0.652	0.636	0.645	0.645	0.645	0.645	0.651	0.644	0.645	0.643	0.650	0.643	0.651	0.650	0.642	0.627	0.655	0.655	0.653	0.660	0.650	0.640	0.662	0.645	0.645
4.0 $\times 10^{-3}$	6.5	0.629	0.629	0.629	0.626	0.631	0.637	0.619	0.629	0.629	0.629	0.628	0.633	0.625	0.630	0.630	0.629	0.627	0.631	0.631	0.628	0.605	0.643	0.619	0.629	0.624	0.634	0.629	0.627	0.629	0.629
1.6 $\times 10^{-2}$	6.5	0.495	0.495	0.495	0.505	0.498	0.501	0.488	0.495	0.495	0.494	0.495	0.494	0.490	0.499	0.489	0.496	0.491	0.495	0.498	0.489	0.526	0.477	0.489	0.494	0.490	0.506	0.495	0.503	0.495	0.495
4.0 $\times 10^{-2}$	6.5	0.403	0.403	0.403	0.431	0.407	0.409	0.401	0.403	0.403	0.403	0.405	0.404	0.376	0.424	0.393	0.416	0.414	0.394	0.405	0.400	0.522	0.344	0.375	0.405	0.392	0.484	0.407	0.402	0.403	0.403
1.6 $\times 10^{-4}$	8.5	1.337	1.368	1.323	1.336	1.336	1.347	1.327	1.337	1.334	1.339	1.337	1.352	1.340	1.333	1.370	1.280	1.363	1.293	1.325	1.343	1.314	1.337	1.327	1.343	1.342	1.337	1.329	1.338	1.316	1.357
2.5 $\times 10^{-4}$	8.5	1.151	1.161	1.150	1.151	1.152	1.168	1.135	1.150	1.151	1.151	1.151	1.166	1.145	1.148	1.171	1.148	1.159	1.157	1.145	1.155	1.143	1.159	1.152	1.147	1.146	1.149	1.150	1.160	1.143	1.159
4.0 $\times 10^{-4}$	8.5	0.993	0.996	0.993	0.995	0.989	1.009	0.981	0.993	0.993	0.990	0.993	0.995	0.991	1.001	0.996	0.991	0.987	0.997	0.991	1.006	0.990	1.001	1.002	1.000	0.994	0.995	0.996	0.981	0.991	0.994
6.3 $\times 10^{-4}$	8.5	0.920	0.921	0.920	0.914	0.927	0.930	0.916	0.920	0.920	0.922	0.920	0.922	0.915	0.912	0.919	0.918	0.907	0.924	0.910	0.924	0.907	0.922	0.920	0.921	0.921	0.919	0.919	0.916	0.920	0.920
1.0 $\times 10^{-3}$	8.5	0.831	0.832	0.831	0.837	0.830	0.842	0.818	0.831	0.831	0.832	0.831	0.833	0.829	0.840	0.835	0.828	0.823	0.842	0.830	0.839	0.812	0.847	0.844	0.841	0.842	0.833	0.834	0.833	0.831	0.831
1.6 $\times 10^{-3}$	8.5	0.704	0.705	0.704	0.708	0.703	0.713	0.694	0.704	0.704	0.705	0.704	0.716	0.700	0.703	0.708	0.702	0.700	0.707	0.708	0.701	0.698	0.713	0.714	0.708	0.713	0.707	0.699	0.711	0.704	0.704
1.6 $\times 10^{-4}$	10.0	1.359	1.432	1.336	1.359	1.359	1.379	1.366	1.353	1.398	1.364	1.359	1.371	1.371	1.349	1.412	1.307	1.381	1.337	1.353	1.375	1.355	1.362	1.343	1.375	1.349	1.356	1.395	1.323	1.339	1.380
2.5 $\times 10^{-4}$	10.0	1.231	1.246	1.227	1.230	1.231	1.238	1.218	1.231	1.228	1.229	1.231	1.254	1.240	1.219	1.247	1.203	1.247	1.209	1.226	1.239	1.221	1.238	1.238	1.230	1.226	1.232	1.230	1.233	1.218	1.243
4.0 $\times 10^{-4}$	10.0	1.136	1.138	1.136	1.136	1.142	1.135	1.135	1.135	1.137	1.137	1.136	1.153	1.137	1.129	1.155	1.132	1.140	1.139	1.126	1.146	1.127	1.142	1.139	1.145	1.139	1.136	1.137	1.123	1.133	1.140
6.3 $\times 10^{-4}$	10.0	0.968	0.969	0.968	0.967	0.967	0.981	0.951	0.968	0.969	0.967	0.968	0.980	0.964	0.976	0.972	0.971	0.964	0.981	0.960	0.978	0.962	0.980	0.974	0.979	0.976	0.966	0.969	0.968	0.967	0.969
1.0 $\times 10^{-3}$	10.0	0.857	0.857	0.857	0.861	0.867	0.870	0.847	0.857	0.857	0.854	0.857	0.861	0.849	0.859	0.853	0.852	0.845	0.864	0.852	0.855	0.849	0.856	0.866	0.866	0.862	0.860	0.848	0.852	0.856	0.857
1.6 $\times 10^{-3}$	10.0	0.792	0.793	0.792	0.797	0.795	0.799	0.785	0.792	0.792	0.790	0.792	0.796	0.789	0.792	0.797	0.790	0.790	0.800	0.792	0.791	0.773	0.801	0.801	0.798	0.803	0.794	0.793	0.785	0.792	0.792
2.5 $\times 10^{-3}$	10.0	0.715	0.715	0.715	0.716	0.721	0.728	0.698	0.715	0.715	0.714	0.714	0.714	0.708	0.710	0.717	0.715	0.711	0.722	0.718	0.715	0.693	0.728	0.738	0.722	0.724	0.719	0.716	0.721	0.715	0.715
6.3 $\times 10^{-3}$	10.0	0.593	0.593	0.593	0.596	0.597	0.601	0.587	0.592	0.593	0.592	0.593	0.597	0.592	0.594	0.591	0.593	0.589	0.594	0.597	0.589	0.574	0.602	0.586	0.596	0.597	0.595	0.593	0.607	0.593	0.593
1.6 $\times 10^{-2}$	10.0	0.517	0.518	0.517	0.518	0.520	0.524	0.511	0.517	0.517	0.517	0.517	0.518	0.516	0.519	0.519	0.520	0.515	0.523	0.520	0.514	0.522	0.515	0.517	0.518	0.515	0.517	0.525	0.517	0.517	0.517
8.1 $\times 10^{-2}$	10.0	0.395	0.395	0.395	0.397	0.395	0.401	0.389	0.395	0.395	0.395	0.396	0.396	0.371	0.409	0.387	0.398	0.395	0.389	0.397	0.394	0.490	0.354	0.363	0.394	0.384	0.410	0.392	0.392	0.395	0.395
2.5 $\times 10^{-4}$	12.0	1.300	1.322	1.290	1.300	1.301	1.305	1.294	1.295	1.307	1.299	1.300	1.310	1.320	1.317	1.334	1.261	1.316	1.277	1.292	1.307	1.297	1.303	1.305	1.306	1.309	1.298	1.305	1.283	1.276	1.325
4.0 $\times 10^{-4}$	12.0	1.128	1.140	1.128	1.127	1.130	1.150	1.117	1.130	1.130	1.129	1.128	1.138	1.127	1.121	1.143	1.114	1.128	1.132	1.125	1.137	1.119	1.134	1.134	1.134	1.139	1.127	1.130	1.129	1.119	1.138
6.3 $\times 10^{-4}$	12.0	1.102	1.104	1.102	1.100	1.102	1.113	1.088	1.101	1.102	1.099	1.102	1.107	1.096	1.110	1.101	1.089	1.086	1.108	1.080	1.107	1.091	1.104	1.104	1.113	1.103	1.102	1.100	1.099	1.102	1.102
1.0 $\times 10^{-3}$	12.0	0.903	0.903	0.903	0.904	0.904	0.912	0.892	0.902	0.903	0.905	0.903	0.915	0.889	0.908	0.900	0.908	0.893	0.909	0.906	0.903	0.892	0.910	0.923	0.913	0.905	0.885	0.905	0.910	0.903	0.903
1.6 $\times 10^{-3}$	12.0	0.789	0.789	0.789	0.793	0.793	0.808	0.780	0.788	0.789	0.788	0.789	0.800	0.791	0.792	0.794	0.791	0.783	0.794	0.788	0.795	0.772	0.792	0.796	0.798	0.795	0.792	0.786	0.798	0.789	0.789
2.5 $\times 10^{-3}$	12.0	0.746	0.746	0.746	0.747	0.753	0.755	0.731	0.746	0.746	0.745	0.746	0.756	0.735	0.747	0.745	0.743	0.743	0.755	0.750	0.744	0.732	0.758	0.756	0.757	0.764	0.745	0.746	0.739	0.746	0.746
2.5 $\times 10^{-4}$	15.0	1.559	1.597	1.541	1.559	1.559	1.556	1.550	1.526	1.574	1.562	1.559	1.578	1.567	1.523	1.612	1.507	1.594	1.510	1.547	1.567	1.535	1.575	1.556	1.564	1.544	1.554	1.564	1.559	1.512	1.606
4.0 $\times 10^{-4}$	15.0	1.338	1.352	1.337	1.337	1.338	1.349	1.329	1.331	1.345	1.339	1.338	1.351	1.341	1.336	1.366	1.320	1.360	1.333	1.333	1.356	1.329	1.358	1.333	1.347	1.334	1.341	1.340	1.329	1.329	1.347
6.3 $\times 10^{-4}$	15.0	1.092	1.093	1.092	1.092	1.092	1.099	1.083	1.092	1.091	1.090	1.092	1.108	1.081	1.093	1.094	1.084	1.084	1.096	1.079	1.101	1.078	1.098	1.104	1.108	1.100	1.092	1.081	1.095	1.087	1.098
1.0 $\times 10^{-3}$	15.0	0.992	0.993	0.992	0.993	0.992	1.002	0.986	0.990	0.992	0.992	0.992	1.013	0.996	0.999	0.995	0.976	0.981	0.998	0.976	1.002	0.978	1.001	1.012	1.001	0.998	0.994	0.995	0.976	0.992	0.992
1.6 $\times 10^{-3}$	15.0	0.908	0.908	0.908	0.906	0.911	0.914	0.903	0.908	0.909	0.905	0.908	0.920	0.907	0.902	0.911	0.910	0.902	0.914	0.907	0.907	0.892	0.914	0.918	0.913	0.910	0.913	0.909	0.892	0.908	0.908
2.5 $\times 10^{-3}$	15.0	0.793	0.793	0.793	0.794	0.795	0.802	0.790	0.792	0.794	0.791	0.793	0.806	0.790	0.791	0.791	0.803	0.790	0.798	0.807	0.790	0.786	0.801	0.811	0.802	0.801	0.796	0.787	0.812	0.793	0.793
6.3 $\times 10^{-3}$	15.0	0.662	0.662	0.662	0.663	0.662	0.671	0.652	0.661	0.662	0.663	0.662	0.675	0.660	0.667	0.662	0.661	0.659	0.664	0.665	0.658	0.640	0.670	0.657	0.664	0.666	0.662	0.664	0.658	0.662	0.662
1.6 $\times 10^{-2}$	15.0	0.553	0.553	0.553	0.553	0.553	0.558	0.548	0.552	0.553	0.552	0.552	0.562	0.552	0.553	0.552	0.552	0.548	0.557	0.555	0.549	0.543	0.559	0.551	0.559	0.550	0.548	0.552	0.551	0.553	0.553
8.1 $\times 10^{-2}$	15.0	0.370	0.370	0.370	0.371	0.370	0.375	0.366	0.370	0.370	0.370	0.371	0.370	0.357	0.379	0.365	0.378	0.376	0.367	0.373	0.368	0.429	0.341	0.349	0.368	0.368	0.376	0.373	0.372	0.370	0.370
4.0 $\times 10^{-4}$	18.0	1.438	1.465	1.432	1.438	1.438	1.447	1.436	1.429	1.445	1.433	1.438	1.460	1.440	1.421	1.469	1.425	1.451	1.428	1.430	1.449	1.435	1.449	1.448	1.440	1.438	1.430	1.437	1.456	1.417	1.459
6.3 $\times 10^{-4}$	18.0	1.166	1.170	1.166	1.167	1.167	1.161	1.152	1.159	1.174	1.165	1.166	1.191	1.168	1.160	1.181	1.154	1.170	1.170	1.153	1.179	1.159	1.171	1.178	1.170	1.168	1.169	1.167	1.145	1.153	1.180
1.0 $\times 10^{-3}$	18.0	1.015	1.016	1.015	1.015	1.015	1.036	1.009	1.017	1.014	1.014	1.015	1.012	1.002	1.028	1.017	1.025	1.005	1.034	1.009	1.022	1.004	1.018	1.020	1.022	1.017	1.001	1.022	1.014	1.013	1.016
1.6 $\times 10^{-3}$	18.0	0.932	0.932	0.932	0.932	0.932	0.941	0.914	0.933	0.932	0.936	0.932	0.941	0.929	0.933	0.935	0.929	0.920	0.936	0.928	0.940	0.925	0.937	0.933	0.938	0.936	0.926	0.920	0.936	0.931	0.934
2.5 $\times 10^{-3}$	18.0	0.879	0.880	0.879	0.880	0.879	0.884	0.872	0.875	0.880	0.876	0.879	0.883	0.873	0.878	0.881	0.889	0.872	0.882	0.888	0.874	0.870	0.888	0.895	0.886	0.889	0.881	0.881	0.874	0.879	0.879
6.3 $\times 10^{-3}$	18.0	0.629	0.629	0.629	0.630	0.630	0.633	0.621	0.631	0.629	0.628	0.629	0.635	0.623	0.630	0.629	0.626	0.627	0.634	0.631	0.627	0.613	0.641	0.626	0.633	0.634	0.630	0.628	0.640	0.629	0.629

Table A1a: *The extracted F_2 values for each systematic check at values of $Q^2 < 100$ GeV^2 or $y = \frac{Q^2}{xs} < 0.01$.*

x	Q^2 (GeV^2)	Systematic check																														
		0	*1*	*2*	*3*	*4*	*5*	*6*	*7*	*8*	*9*	*10*	*11*	*12*	*13*	*14*	*15*	*16*	*17*	*18*	*19*	*20*	*21*	*22*	*23*	*24*	*25*	*26*	*27*	*28*	*29*
4.0×10^{-4}	22.0	1.507	1.534	1.493	1.507	1.507	1.519	1.500	1.506	1.488	1.513	1.507	1.526	1.526	1.515	1.572	1.436	1.562	1.462	1.497	1.522	1.496	1.516	1.505	1.493	1.505	1.514	1.525	1.498	1.479	1.536
6.3×10^{-4}	22.0	1.324	1.332	1.324	1.324	1.324	1.335	1.320	1.325	1.330	1.327	1.324	1.338	1.304	1.326	1.331	1.292	1.324	1.307	1.307	1.333	1.315	1.336	1.334	1.330	1.323	1.323	1.309	1.337	1.311	1.338
1.0×10^{-3}	22.0	1.081	1.083	1.081	1.081	1.081	1.083	1.064	1.065	1.085	1.079	1.081	1.094	1.080	1.073	1.093	1.080	1.076	1.095	1.072	1.094	1.069	1.086	1.089	1.088	1.089	1.079	1.085	1.069	1.079	1.083
1.6×10^{-3}	22.0	0.930	0.930	0.930	0.930	0.930	0.939	0.923	0.920	0.938	0.930	0.930	0.954	0.921	0.938	0.930	0.928	0.922	0.938	0.927	0.937	0.930	0.940	0.944	0.936	0.928	0.911	0.931	0.945	0.930	0.930
2.5×10^{-3}	22.0	0.906	0.906	0.906	0.906	0.906	0.912	0.897	0.904	0.912	0.907	0.906	0.916	0.898	0.899	0.897	0.906	0.900	0.913	0.903	0.900	0.896	0.913	0.914	0.913	0.913	0.906	0.893	0.915	0.906	0.906
4.0×10^{-3}	22.0	0.749	0.750	0.749	0.750	0.749	0.756	0.743	0.747	0.754	0.750	0.749	0.763	0.752	0.754	0.760	0.741	0.739	0.757	0.747	0.751	0.729	0.755	0.777	0.752	0.755	0.754	0.763	0.728	0.749	0.749
6.3×10^{-3}	22.0	0.701	0.701	0.701	0.701	0.701	0.705	0.696	0.697	0.703	0.701	0.701	0.722	0.700	0.701	0.691	0.709	0.701	0.700	0.707	0.692	0.690	0.714	0.696	0.703	0.707	0.703	0.695	0.717	0.701	0.701
1.0×10^{-2}	22.0	0.601	0.601	0.601	0.601	0.601	0.609	0.591	0.598	0.601	0.601	0.601	0.605	0.596	0.603	0.604	0.600	0.597	0.606	0.606	0.600	0.577	0.612	0.589	0.603	0.600	0.592	0.601	0.607	0.601	0.601
2.5×10^{-2}	22.0	0.490	0.490	0.490	0.490	0.490	0.494	0.486	0.488	0.494	0.490	0.488	0.497	0.489	0.491	0.491	0.491	0.487	0.494	0.492	0.488	0.487	0.492	0.489	0.491	0.487	0.481	0.496	0.487	0.490	0.490
8.1×10^{-2}	22.0	0.338	0.338	0.338	0.338	0.338	0.340	0.334	0.336	0.341	0.338	0.342	0.337	0.321	0.352	0.328	0.346	0.343	0.331	0.340	0.334	0.400	0.305	0.308	0.337	0.336	0.350	0.334	0.355	0.338	0.338
6.3×10^{-4}	27.0	1.460	1.475	1.454	1.460	1.460	1.468	1.460	1.484	1.452	1.455	1.460	1.476	1.453	1.470	1.477	1.450	1.467	1.455	1.456	1.463	1.447	1.461	1.473	1.466	1.462	1.456	1.461	1.461	1.443	1.476
1.0×10^{-3}	27.0	1.194	1.196	1.194	1.194	1.194	1.200	1.189	1.206	1.204	1.194	1.194	1.208	1.185	1.193	1.199	1.184	1.195	1.193	1.183	1.201	1.186	1.203	1.208	1.196	1.199	1.194	1.188	1.194	1.187	1.200
1.6×10^{-3}	27.0	1.140	1.141	1.140	1.140	1.140	1.147	1.125	1.131	1.133	1.139	1.140	1.155	1.113	1.148	1.145	1.154	1.124	1.155	1.143	1.145	1.142	1.140	1.142	1.145	1.144	1.141	1.117	1.138	1.140	1.140
2.5×10^{-3}	27.0	0.928	0.929	0.928	0.928	0.928	0.934	0.928	0.926	0.935	0.929	0.928	0.945	0.926	0.935	0.921	0.925	0.921	0.935	0.925	0.926	0.917	0.931	0.935	0.931	0.934	0.919	0.929	0.915	0.928	0.928
4.0×10^{-3}	27.0	0.765	0.765	0.765	0.765	0.765	0.772	0.761	0.758	0.776	0.764	0.765	0.783	0.765	0.772	0.767	0.767	0.765	0.770	0.773	0.766	0.750	0.769	0.787	0.774	0.778	0.770	0.768	0.771	0.763	0.767
6.3×10^{-3}	27.0	0.674	0.674	0.674	0.674	0.674	0.676	0.672	0.668	0.680	0.675	0.674	0.689	0.672	0.670	0.667	0.673	0.669	0.673	0.674	0.665	0.663	0.679	0.673	0.680	0.687	0.673	0.674	0.670	0.674	0.674
6.3×10^{-4}	35.0	1.565	1.589	1.551	1.565	1.565	1.583	1.556	1.566	1.545	1.564	1.565	1.577	1.553	1.561	1.607	1.545	1.590	1.557	1.556	1.574	1.564	1.579	1.572	1.551	1.556	1.574	1.561	1.553	1.544	1.586
1.0×10^{-3}	35.0	1.370	1.374	1.369	1.370	1.370	1.371	1.355	1.366	1.351	1.368	1.370	1.373	1.346	1.359	1.371	1.367	1.361	1.367	1.365	1.376	1.361	1.368	1.370	1.374	1.371	1.370	1.370	1.353	1.360	1.380
1.6×10^{-3}	35.0	1.149	1.150	1.149	1.149	1.149	1.150	1.153	1.156	1.145	1.149	1.149	1.158	1.152	1.156	1.137	1.157	1.136	1.157	1.136	1.150	1.141	1.156	1.154	1.157	1.154	1.145	1.152	1.135	1.146	1.152
2.5×10^{-3}	35.0	1.018	1.020	1.018	1.018	1.018	1.027	1.005	1.028	1.008	1.018	1.018	1.043	1.009	1.027	1.016	1.006	1.009	1.021	1.006	1.025	1.007	1.023	1.019	1.023	1.017	1.018	1.005	1.043	1.018	1.018
4.0×10^{-3}	35.0	0.887	0.889	0.887	0.887	0.887	0.891	0.885	0.885	0.886	0.888	0.887	0.886	0.883	0.885	0.896	0.896	0.887	0.898	0.895	0.892	0.883	0.895	0.912	0.896	0.892	0.890	0.884	0.876	0.887	0.887
6.3×10^{-3}	35.0	0.749	0.749	0.749	0.749	0.749	0.757	0.750	0.751	0.758	0.746	0.749	0.747	0.754	0.755	0.748	0.750	0.748	0.747	0.756	0.743	0.737	0.755	0.755	0.757	0.765	0.757	0.770	0.768	0.749	0.749
1.0×10^{-2}	35.0	0.681	0.682	0.681	0.681	0.681	0.682	0.674	0.672	0.688	0.681	0.681	0.689	0.664	0.679	0.670	0.684	0.680	0.682	0.682	0.673	0.666	0.683	0.662	0.684	0.685	0.680	0.675	0.689	0.681	0.681
1.6×10^{-2}	35.0	0.604	0.604	0.604	0.604	0.604	0.609	0.599	0.597	0.604	0.602	0.604	0.610	0.606	0.602	0.609	0.598	0.593	0.612	0.607	0.602	0.591	0.614	0.600	0.604	0.602	0.605	0.598	0.603	0.604	0.604
2.5×10^{-2}	35.0	0.570	0.570	0.570	0.570	0.570	0.574	0.566	0.571	0.567	0.569	0.570	0.582	0.567	0.571	0.568	0.575	0.569	0.571	0.573	0.567	0.569	0.575	0.574	0.571	0.567	0.569	0.571	0.589	0.570	0.570
8.1×10^{-2}	35.0	0.461	0.461	0.461	0.461	0.461	0.464	0.458	0.459	0.457	0.459	0.471	0.461	0.449	0.470	0.448	0.468	0.465	0.454	0.464	0.457	0.511	0.429	0.431	0.460	0.459	0.465	0.465	0.449	0.461	0.461
1.0×10^{-3}	45.0	1.441	1.451	1.436	1.441	1.441	1.452	1.436	1.462	1.441	1.441	1.441	1.462	1.458	1.456	1.478	1.413	1.466	1.427	1.438	1.458	1.433	1.445	1.456	1.451	1.454	1.443	1.434	1.468	1.428	1.453
1.6×10^{-3}	45.0	1.178	1.180	1.178	1.178	1.178	1.179	1.169	1.178	1.157	1.176	1.178	1.200	1.163	1.160	1.187	1.172	1.168	1.186	1.165	1.189	1.172	1.195	1.187	1.179	1.175	1.175	1.165	1.168	1.163	1.194
2.5×10^{-3}	45.0	1.071	1.072	1.071	1.071	1.071	1.071	1.071	1.074	1.075	1.070	1.071	1.077	1.074	1.072	1.072	1.069	1.068	1.081	1.059	1.079	1.066	1.066	1.073	1.076	1.074	1.070	1.052	1.073	1.071	1.071
4.0×10^{-3}	45.0	0.894	0.895	0.894	0.894	0.894	0.902	0.892	0.897	0.891	0.891	0.894	0.905	0.894	0.893	0.889	0.895	0.887	0.896	0.899	0.891	0.880	0.896	0.909	0.897	0.894	0.895	0.917	0.883	0.894	0.894
6.3×10^{-3}	45.0	0.804	0.804	0.804	0.804	0.804	0.804	0.797	0.809	0.787	0.800	0.804	0.827	0.799	0.792	0.802	0.804	0.794	0.807	0.809	0.803	0.800	0.808	0.829	0.810	0.804	0.801	0.782	0.847	0.804	0.804
1.0×10^{-2}	45.0	0.745	0.745	0.745	0.745	0.745	0.755	0.746	0.749	0.736	0.747	0.745	0.763	0.746	0.761	0.738	0.751	0.753	0.746	0.751	0.739	0.724	0.754	0.732	0.748	0.749	0.743	0.754	0.713	0.745	0.745
1.0×10^{-3}	60.0	1.553	1.567	1.540	1.553	1.553	1.563	1.557	1.599	1.526	1.545	1.553	1.555	1.510	1.573	1.555	1.529	1.547	1.554	1.544	1.566	1.542	1.576	1.552	1.540	1.543	1.553	1.585	1.535	1.545	1.562
1.6×10^{-3}	60.0	1.339	1.342	1.338	1.339	1.339	1.345	1.349	1.345	1.331	1.339	1.339	1.357	1.334	1.332	1.331	1.344	1.332	1.342	1.331	1.344	1.337	1.328	1.365	1.349	1.353	1.340	1.334	1.327	1.334	1.343
2.5×10^{-3}	60.0	1.100	1.101	1.100	1.100	1.100	1.107	1.083	1.117	1.085	1.099	1.100	1.114	1.090	1.106	1.105	1.102	1.095	1.113	1.095	1.113	1.099	1.110	1.090	1.101	1.104	1.101	1.106	1.089	1.096	1.104
4.0×10^{-3}	60.0	1.012	1.013	1.012	1.012	1.012	1.005	1.006	1.011	1.001	1.009	1.012	1.029	1.014	0.989	1.002	1.003	0.999	1.016	1.002	1.003	0.997	1.016	1.023	1.017	1.011	1.011	1.003	1.018	1.012	1.012
6.3×10^{-3}	60.0	0.890	0.891	0.890	0.890	0.890	0.894	0.886	0.900	0.883	0.893	0.890	0.900	0.883	0.892	0.889	0.900	0.890	0.890	0.906	0.884	0.878	0.893	0.917	0.900	0.890	0.891	0.914	0.881	0.890	0.890
1.0×10^{-2}	60.0	0.672	0.672	0.672	0.672	0.672	0.675	0.676	0.684	0.675	0.672	0.672	0.678	0.673	0.681	0.673	0.672	0.670	0.679	0.671	0.668	0.673	0.683	0.660	0.673	0.679	0.671	0.676	0.683	0.672	0.672
1.6×10^{-2}	60.0	0.614	0.614	0.614	0.614	0.614	0.618	0.609	0.633	0.621	0.610	0.615	0.621	0.614	0.611	0.615	0.612	0.611	0.625	0.621	0.612	0.594	0.625	0.608	0.616	0.617	0.611	0.620	0.660	0.614	0.614
2.5×10^{-2}	60.0	0.627	0.627	0.627	0.627	0.627	0.626	0.626	0.628	0.624	0.625	0.628	0.637	0.626	0.628	0.624	0.631	0.626	0.624	0.628	0.625	0.620	0.634	0.633	0.628	0.626	0.633	0.628	0.639	0.627	0.627
8.1×10^{-2}	60.0	0.521	0.521	0.521	0.521	0.521	0.528	0.518	0.528	0.518	0.518	0.523	0.524	0.510	0.527	0.511	0.528	0.524	0.518	0.526	0.514	0.564	0.494	0.498	0.520	0.518	0.516	0.525	0.511	0.521	0.521
1.6×10^{-3}	70.0	1.318	1.327	1.313	1.318	1.318	1.313	1.308	1.321	1.318	1.322	1.318	1.344	1.320	1.305	1.346	1.298	1.335	1.311	1.315	1.326	1.308	1.330	1.318	1.330	1.337	1.314	1.357	1.297	1.298	1.338
2.5×10^{-3}	70.0	1.228	1.229	1.228	1.228	1.228	1.226	1.219	1.233	1.192	1.229	1.228	1.233	1.195	1.221	1.207	1.224	1.210	1.236	1.216	1.231	1.219	1.217	1.235	1.238	1.237	1.225	1.183	1.239	1.228	1.228
4.0×10^{-3}	70.0	0.917	0.917	0.917	0.917	0.917	0.931	0.913	0.940	0.911	0.916	0.917	0.923	0.911	0.935	0.918	0.925	0.915	0.926	0.918	0.922	0.931	0.918	0.923	0.921	0.907	0.915	0.932	0.919	0.917	0.917
6.3×10^{-3}	70.0	0.887	0.888	0.887	0.887	0.887	0.891	0.883	0.894	0.872	0.880	0.887	0.896	0.881	0.880	0.890	0.886	0.883	0.892	0.891	0.891	0.888	0.889	0.917	0.885	0.884	0.888	0.864	0.891	0.887	0.887
1.0×10^{-2}	70.0	0.774	0.774	0.774	0.774	0.774	0.789	0.766	0.792	0.756	0.778	0.774	0.792	0.762	0.768	0.771	0.778	0.766	0.777	0.774	0.765	0.759	0.789	0.753	0.779	0.778	0.775	0.784	0.778	0.774	0.774
1.6×10^{-2}	70.0	0.697	0.697	0.697	0.697	0.697	0.692	0.698	0.693	0.693	0.698	0.697	0.715	0.709	0.707	0.697	0.699	0.708	0.699	0.713	0.692	0.680	0.701	0.711	0.696	0.701	0.697	0.700	0.681	0.697	0.697
2.5×10^{-2}	70.0	0.607	0.607	0.607	0.607	0.607	0.613	0.602	0.614	0.593	0.608	0.598	0.609	0.608	0.603	0.607	0.604	0.602	0.611	0.606	0.607	0.590	0.609	0.606	0.608	0.604	0.609	0.609	0.621	0.607	0.607
8.1×10^{-2}	70.0	0.484	0.484	0.484	0.484	0.484	0.481	0.485	0.489	0.480	0.480	0.478	0.494	0.477	0.490	0.477	0.491	0.486	0.480	0.488	0.481	0.508	0.471	0.466	0.483	0.485	0.483	0.476	0.486	0.484	0.484
1.6×10^{-3}	90.0	1.363	1.386	1.349	1.363	1.363	1.390	1.372	1.404	1.381	1.357	1.363	1.385	1.395	1.381	1.426	1.319	1.382	1.358	1.346	1.377	1.372	1.374	1.377	1.359	1.374	1.360	1.381	1.411	1.363	1.363
2.5×10^{-3}	90.0	1.275	1.277	1.274	1.275	1.275	1.278	1.275	1.278	1.259	1.271	1.275	1.274	1.251	1.270	1.300	1.257	1.290	1.277	1.254	1.288	1.258	1.289	1.275	1.282	1.265	1.277	1.281	1.274	1.268	1.282
4.0×10^{-3}	90.0	1.068	1.069	1.068	1.068	1.068	1.068	1.073	1.075	1.068	1.063	1.068	1.083	1.064	1.059	1.070	1.092	1.050	1.084	1.068	1.081	1.071	1.076	1.079	1.073	1.077	1.070	1.092	1.048	1.062	1.075
6.3×10^{-3}	90.0	0.974	0.974	0.974	0.974	0.974	0.974	0.970	0.981	0.960	0.978	0.974	0.989	0.963	0.980	0.972	0.985	0.971	0.978	0.987	0.977	0.968	0.984	0.976	0.978	0.975	0.974	0.997	0.971	0.974	0.974
1.0×10^{-2}	90.0	0.845	0.845	0.845	0.845	0.845	0.836	0.843	0.838	0.830	0.851	0.845	0.857	0.826	0.840	0.834	0.848	0.847	0.847	0.844	0.828	0.839	0.852	0.869	0.849	0.861	0.844	0.837	0.836	0.845	0.845
1.6×10^{-2}	90.0	0.619	0.619	0.619	0.619	0.619	0.634	0.610	0.647	0.592	0.618	0.619	0.623	0.622	0.629	0.616	0.615	0.609	0.619	0.620	0.612	0.596	0.612	0.607	0.622	0.610	0.619	0.616	0.580	0.619	0.619
2.5×10^{-2}	90.0	0.556	0.557	0.556	0.556	0.556	0.555	0.560	0.568	0.557	0.554	0.550	0.548	0.565	0.557	0.554	0.551	0.551	0.563	0.555	0.551	0.544	0.563	0.560	0.559	0.562	0.561	0.559	0.590	0.556	0.556
4.0×10^{-2}	90.0	0.526	0.526	0.526	0.526	0.526	0.528	0.523	0.526	0.518	0.527	0.516	0.526	0.521	0.513	0.528	0.516	0.520	0.529	0.527	0.534	0.526	0.510	0.513	0.523	0.525	0.521	0.523	0.560	0.526	0.526
8.1×10^{-2}	90.0	0.453	0.453	0.453	0.453	0.453	0.456	0.451	0.458	0.443	0.452	0.463	0.476	0.454	0.453	0.451	0.460	0.455	0.454	0.456	0.449	0.466	0.445	0.443	0.452	0.450	0.449	0.443	0.473	0.453	0.453
2.0×10^{-1}	90.0	0.255	0.255	0.255	0.255	0.255	0.251	0.257	0.259	0.253	0.253	0.268	0.305	0.245	0.264	0.233	0.263	0.263	0.235	0.257	0.251	0.296	0.242	0.255	0.254	0.259	0.278	0.243	0.292	0.255	0.255
2.0×10^{-1}	120.0	0.207	0.207	0.207	0.207	0.207	0.213	0.207	0.210	0.203	0.207	0.232	0.212	0.198	0.217	0.196	0.219	0.218	0.198	0.207	0.205	0.245	0.193	0.187	0.206	0.208	0.226	0.197	0.255	0.207	0.207
2.0×10^{-1}	150.0	0.288	0.288	0.288	0.288	0.288	0.286	0.284	0.287	0.280	0.289	0.301	0.296	0.269	0.297	0.273	0.302	0.296	0.278	0.288	0.287	0.310	0.272	0.259	0.288	0.290	0.294	0.294	0.281	0.288	0.288

Table A1b: *The extracted F_2 values for each systematic check at values of $Q^2 < 100$ GeV^2 or $y = \frac{Q^2}{xs} < 0.01$.*

Class	Checks contributing to class	a_{class}	b_{class}	c_{class}
A	11;5;7	2.34	0.96	0
–A	6;8;9	–1.94	–0.83	0
B	1;29	0.126	0	0
–B	2;28	–0.085	0	0
C	12;14	0.153	$4.4 \cdot 10^{-3}$	0
–C	3;4;13;15;27	–0.145	$-3.4 \cdot 10^{-3}$	0
D	10;16;26;25	0.132	$4.3 \cdot 10^{-3}$	0.69
–D	17;22;24;23	–0.146	$-7.4 \cdot 10^{-3}$	–1.29
E	21	1.62	0.39	0
–E	20	–3.05	–0.77	0
F	19	1.05	0.83	0
–F	18	–1.00	–0.79	0

Table A2: *The parameters of the functions describing the different classes of systematic uncertainties of F_2 (see text).*

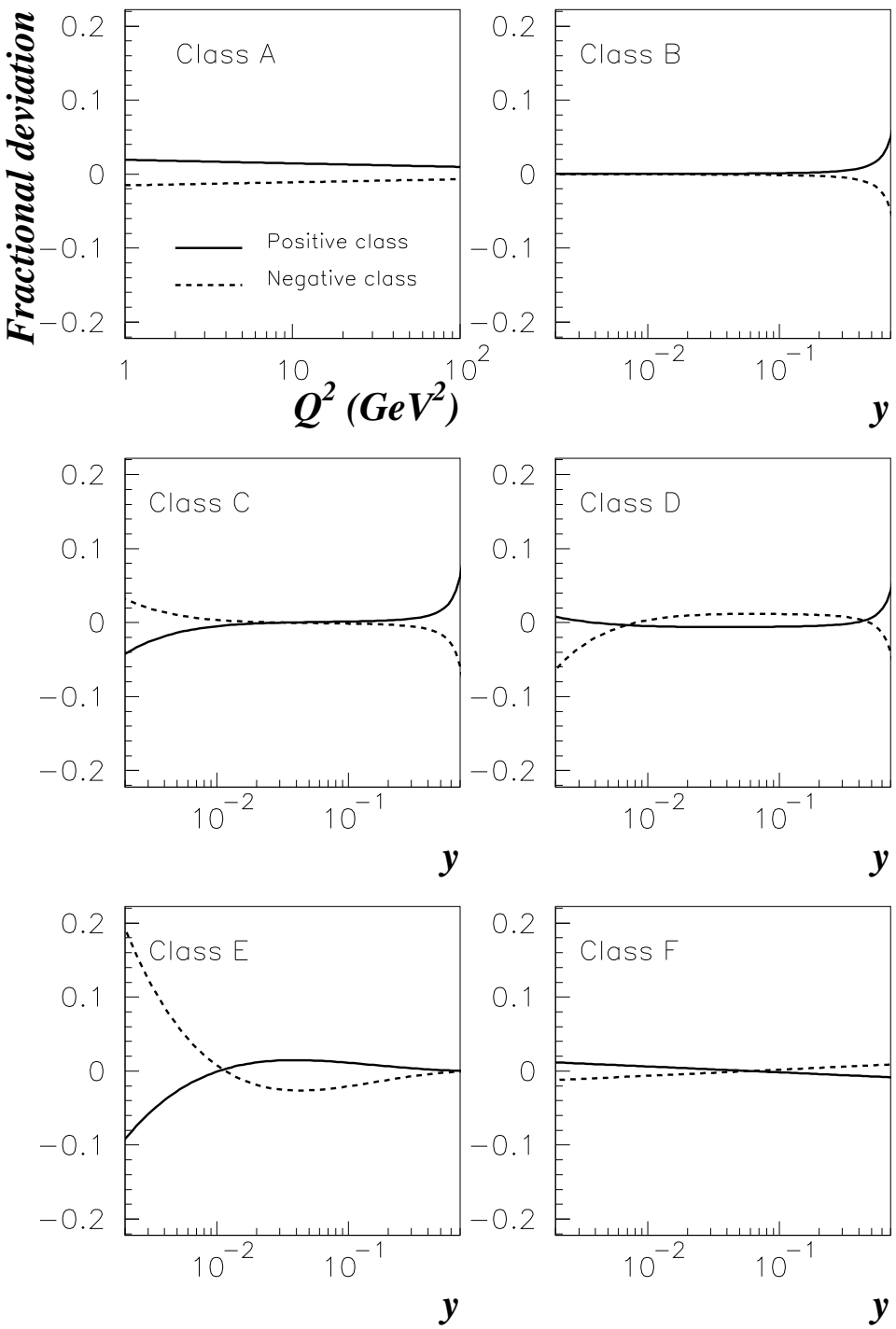

Figure A1: *The Q^2 or y dependence of $\frac{\Delta F_2}{F_2}$ for the six classes of systematic uncertainties (see text).*